THE DESIGN AND CONTROL OF A BATTERY-SUPERCAPACITOR

HYBRID ENERGY STORAGE MODULE

FOR NAVAL APPLICATIONS

by

ISAAC J. COHEN

Presented to the Faculty of the Graduate School of

The University of Texas at Arlington in Partial Fulfillment

of the Requirements

for the Degree of

DOCTOR OF PHILOSOPHY

THE UNIVERSITY OF TEXAS AT ARLINGTON

May 2016

Acknowledgements

First and foremost I would like to thank my family for their support and encouragement through my academic career. My wife, Bailey, my parents, Eli, Kelly, Cara, and Darryl, and my siblings, Jesse and Brittany have all been sources of inspiration and a shelter during stressful times.

I also want to thank my advisor, Dr. David Wetz, for not only his advice and mentorship through this time, but also for his friendship. I would like to thank my mentors throughout my academic career, Dr. Rasool Kenarangui, Dr. John Heinzel, and Dr. Qing Dong, for all of their guidance and counsel. I would like to thank all of my committee members, Dr. Wei-Jen Lee, Dr. William Dillon, and Dr. Ali Davoudi, for the invaluable suggestions and comments that have helped me to shape my dissertation topic.

Finally, I would like to thank my lab mates over the years, Clint, Matt, Chris, Derek, Caroline, Kendal, Calvin, Donald and Brian, for always offering a helping hand, allowing me to bounce ideas off of you, and for telling me when those ideas were less than intelligent.

Without all of your help and encouragement, none of this would have been possible and for that, I thank all of you.

April 25, 2016

Abstract

THE DESIGN AND CONTROL OF A BATTERY-SUPERCAPACITOR HYBRID

ENERGY STORAGE MODULE FOR NAVAL APPLICATIONS

Isaac J. Cohen, PhD

The University of Texas at Arlington, 2016

Supervising Professor: David Wetz, PhD

As the Navy transitions to a more electrical fleet, the electrical architectures must adapt to the changing load profiles. With the introduction of electrical propulsion and new types of electrical energy based weapons, load profiles have become higher power and more transient than ever seen before – especially during directed energy weapon operation. One issue that has become apparent with the introduction of these transient loads is the ability of traditional generation sources, such as fossil fuel generators, to power them. Generators are stiff sources of power which suffer efficiency losses when they deviate from operating at a constant maximum load. The logical answer to this problem is to create a low-pass filter on the power flow by inserting an energy storage device that is capable of both sinking and sourcing energy in order to keep the power demand constant. In a Naval setting, the traditional approach to energy storage devices would be lead acid batteries, but with recent developments in lithium-ion chemistries, it would be preferable to utilize energy dense lithium-ion batteries to save precious space and weight on board the ship. Although lithium-ion batteries offer many benefits, one

issue they face is a degradation of lifetime when the battery is cycled at high rates. One solution that might come to mind is to simply use a power dense device that is relatively unaffected by high rate usage such as a capacitor, but these devices typically do not possess enough energy density to accommodate the system for long periods of time – even sourcing power for periods of time where there may be a deficiency in generation. One proposed method of overcoming these challenges is the integration of both energy dense and power dense devices into a single module, referred to as a hybrid energy storage module. In the case of a battery-supercapacitor hybrid energy storage module, the voltage of each device is proportional to the energy stored. If these devices were simply placed in parallel, as energy is drawn from the module, the voltage will drop on the capacitor quicker than it will from the battery, leading to a situation where the battery will source the majority of the current due to voltage dominance. In order to minimize the current batteries, power electronic converters are placed in front of the battery to actively control the amount of current flowing in and out of it. There are many challenges when designing this type of system – especially when considering how to integrate this into existing shipboard systems using commercial-off-the-shelf components. The research presented here will delve into the design and control of a hybrid energy storage module. The work presented here will present the mathematical model of a hybrid energy storage module, it will show the simulation of this system using the SimPowerSystems toolbox within MATLAB/Simulink, it will build this system up on a tabletop testbed to validate the simulation results, and finally it will evaluate the integration of this components using commercial-off-the-shelf components to mimic a real-life implementation of such a system.

Table of Contents

List of Figures

List of Tables

Chapter 1: Introduction and Hypothesis

Traditionally, armed forces such as the United States Navy have relied upon fossil fuel based energy generation to propel their ships and provide the electrical power needed to operate their conventional and unique electrical loads, while weapon systems have primarily relied on chemical combustion for propulsion and explosives to deliver damage to the target. It is the near term desire of the US Navy to transition into a more electric fleet, utilizing alternative forms of electrical energy generation to power both the propulsion systems as well as a number of advanced electrical weapon systems currently under development such as railguns, solid state lasers, and high power microwave (HPM) generators, all of which rely on pulsed power sources [1, 2, 3]. With this desire comes the need to integrate a large number of vastly different high power electrical loads into a ship or forward operating base's (FOBs) electrical generation grid. Whether on a ship or on land, the power distribution grids being used are essentially MicroGrids. These complex demands require that a number of different electrical generation sources, such as fossil fuel generators, solar panels, fuel cells, flywheels, wind turbines, batteries, and capacitors be installed and intelligently monitored and controlled to ensure power delivery at all times to the critical loads. As one may expect, this is not a trivial task.

The next generation naval destroyer, the Zumwalt class, is one example of the US Navy's shift towards implementing a more electric fleet. This class of ship features 78 MW of total distributed power generation as part of the next generation integrated power systems (NGIPS). The NGIPS automatically adjusts power generation and distribution,

enabling future naval ships to more quickly adapt to changing combat conditions while reliably engaging high power load systems [4, 5, 6, 7, 8].

Nearly all of the distributed generation sources discussed earlier are unregulated sources which require the use of power electronic voltage converters, a point of discussion later, to regulate their voltage before they are connected to a point of common coupling. In islanded systems, such as on a naval vessel – where there is no way to connect to a larger grid, the operation of high power loads can account for a significant percentage of available power generation. As a result, they are capable of forcing even fuel based power generation out of stiff operating conditions. To augment the primary generation sources and maintain a stiff bus voltage, renewable energy sources can be employed. These sources have trade-offs that must be properly managed for success. Wind turbines and solar panels offer low power density and intermittent operation, thereby reducing their usefulness and reliability as a direct form of prime power generation for high continuous or pulsed power loads. Fuel cells offer high energy density but low power density making them a bit more reliable but still not a direct form of power generation in most cases. Flywheels offer a high combined power and energy making them extremely useful for driving pulsed power systems, but their cost and complexity often makes using them difficult [9, 10]. As will be shown later, electrochemical batteries and capacitors, when used together, hold a great deal of promise for use in driving pulsed power systems when combined together as batteries are very energy dense and capacitors are power dense.

Historically, pulsed power research has been performed in large laboratories where size and weight have not been the most pressing of concerns. Instead, the focus has been

on improving size, lifetime, reliability, and efficiency of high power switches, intermediate energy storage systems, pulse forming lines and circuit topologies, and new end use loads [11, 12, 13]. Before new advanced pulsed power systems, such as those discussed earlier, can be implemented on either mobile or small footprint stationary applications, the prime power source which drives them must be optimized for both size and operational efficiency. While it would be ideal to have these loads powered directly off of the same generation source used to propel the ship, the high transient nature of the pulsed loads, coupled with the intermittent use of them, would make the implementation of such a large generator extremely inefficient. This is where alternative power sources, in particular electrochemical batteries and capacitors, become vital for success.

Technological advancements in the field of electrochemistry have enabled the development of batteries and capacitors with higher combined energy and power than ever previously thought possible. Despite these advances, there is still no one cell which possess the optimum power and energy density for all applications. Lithium-ion batteries (LIBs) and electric-double-layer capacitors (EDLCs) with energy densities in the range of 100 - 200 Wh/kg and 10 Wh/kg [14] respectively, are available commercially off the shelf (COTS). COTS LIBs typically offer power densities in the range of 0.1 – 0.5 kW/kg though specialty high power LIBs are available with power densities as high as 28 kW/kg [15, 16, 17]. While these power densities, especially those from the specialty cells, are very desirable, the usable capacity of the device can often be significantly reduced when they are operated at their full power capabilities, thereby reducing the operational efficiency and life span [18, 16, 19]. In addition to

these drawbacks, the expensive costs and commercial unavailability of many devices causes them to be undesirable as the sole power source. Repetitive operation at high power has been shown to significantly reduce a LIB's cycle life, thereby increasing the cost per 'shot' ratio of the system when more frequent battery replacement is required [18]. While EDLCs do not offer high energy densities, they offer power densities as high as 5 kW/kg and their long cycle life, up to 10^6 cycles, is not reduced when they are operated at extreme power levels [20]. Therefore, the ability to utilize both of these energy storage technologies within a single Hybrid Energy Storage Module (HESM) provides the ability to optimize the power supply's weight, volume, power density, energy density, and cycle life.

The goal of the HESM is to maximize the operational and cycle life of the batteries by limiting the currents which they discharge and recharge at. The capacitor is used to supply the bulk of the transient currents and currents in excess of those which are harmful to the battery. The battery is used as the main energy supply to recharge the capacitor as well as supply a steady portion of the current to the load. Similarly, during recharge the battery's current can be limited while the capacitor absorbs a high rate of recharge.

HESMs are not a new concept with the fundamental topologies having already been developed, seen in Figure 1 and Figure 2. In its simplest form, the passive topology, batteries and capacitors are simply connected in parallel with their load. In Figure 1, the load is a two-quadrant DC/DC converter and a DC bus. In this configuration, the internal equivalent series resistance (ESR) of each device drives where the energy supplied to the load comes from. In the case of high transient loads, the capacitors lower ESR

enables them to supply the front end power while the batteries are used to supply the steady energy [21]. [22] previously showed that the front end and steady state power draw supplied by batteries is significantly reduced when capacitors are added.
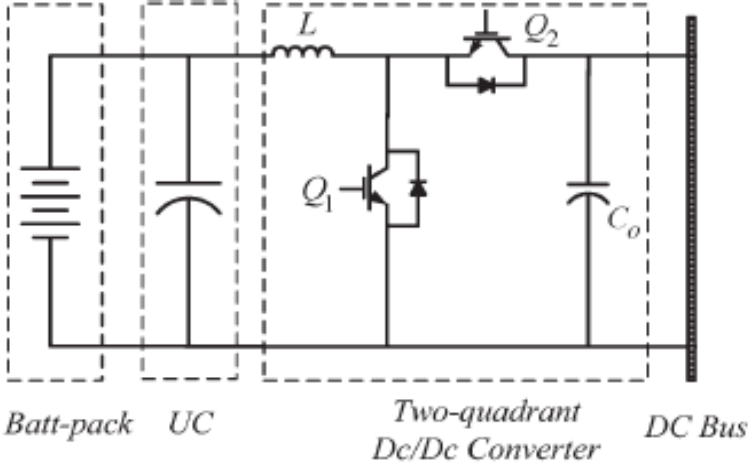
Figure 1: Circuit diagram of an example passive HESM [23]
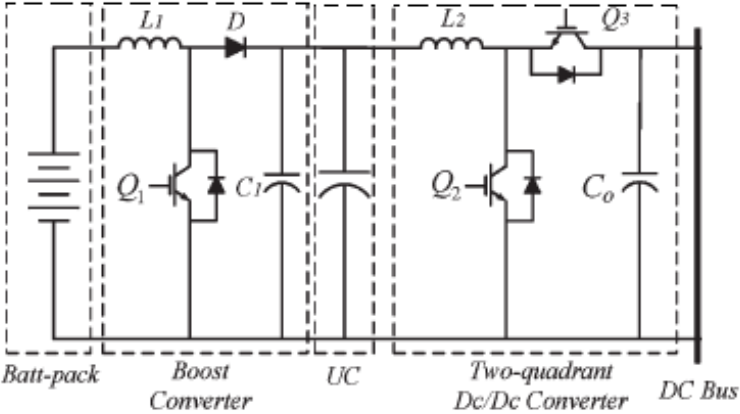
Figure 2: Circuit diagram of an example active HESM [20]

An active HESM topology is more complex, but this comes with increased instantaneous power capabilities and longevity. With this topology, the focus is on maintaining the system bus voltage and controlling the currents drawn out of the distributed power sources. Notice in Figure 2 how the battery is independently regulated

15

using a boost converter. The output of the boost converter feeds the capacitor and then the DC/DC converter, therefore the capacitor picks up whatever portion of the load is not supplied by the battery.

Previous work has shown that Hybrid Energy Storage Modules (HESMs) can contribute to not only improve the performance of an energy storage device (ESD), but also overcome the limitations of the individual components of the architecture, such as the power delivery limitations of a battery or the energy storage limitations of an ultracapacitor [24, 25, 26]. While this topology has been verified, there are still some questions on how to best control them. Many of the published efforts thus far have focused on the development of control algorithms and mathematical models for specialized, research based, reconfigurable power electronic converters. In these cases, validations of the experimental control algorithms have been performed using small proof of concept hardware setups. Voltages and currents are typically in the vicinity of a few volts or amps, respectively, allowing the power electronic converter to be the focus of the work. While the previously published works do a great job at demonstrating the many advantages a HESM offers, significant time, effort, and money is required to build up the capability to develop custom power electronics. This can be prohibitive to the advancement of HESM research outside of the power electronics area. [27] designed a low cost digital energy management system and an optimal control algorithm was developed in [28] to coordinate slow ESDs and fast ESDs. While these control developments have been very useful, they do not address the need for a controller that is capable of interfacing with COTS products. Fuzzy logic control has been used in many applications such as [29], who developed an intuitive fuzzy logic

based learning algorithm which was implemented to reduce intensive computation of a complex dynamics such as a humanoid. Some, such as [30] have utilized fuzzy logic control to drive a HESM, but in their case, they used the controller in order to eliminate the need to constantly calculate resource intensive Riccati equations to assist in choosing gains for an adaptive Linear-Quadratic Regulator controller. Others, such as [31, 32] developed an energy-based split and power sharing control strategy for hybrid energy storage systems, but these strategies are focused on different target variables such as loss reduction, leveling the components state of charge, or optimizing system operating points in a vehicular system.

When constructing a HESM for naval pulsed power load applications, several design parameters must be considered to develop the controller. First, the HESM must be responsible for supplying all load demands that it might encounter. Energy sizing techniques such as shown in [33] should be applied in order to assist in meeting this demand. Second, the HESM should add the benefit of becoming an additional source during parallel operation with an existing shipboard power system, offering a reduction in external power system sizing. Finally, the HESM should operate as a power buffer during this parallel operation, offering improved power quality to the load from sluggish generation sources, such as fossil-fuel generators, such as seen in [34].

There are many combinations of high power density and high energy density ESDs that can be used to create a HESM, but a common topology that will be evaluated in this paper is the combination of ultracapacitors and batteries. Although the Navy has traditionally used lead-acid batteries as the go-to ESD, lithium-ion batteries (LIBs) offer a higher energy and power density with respect to both volume and weight. In this

scenario, a HESM becomes even more necessary as previous research has shown that while LIBs are capable of being cycled at high rates, they degrade much more quickly [34] – necessitating the limiting of power to and from the battery to be as minimal as possible. This limitation can be implemented through the introduction of intelligent controls.

In the work presented here, an active HESM will be designed and developed using COTS components. A challenge that will be presented by this system is how to offer a form of system level control over the integrated components. To achieve this, steps will be taken to mathematically model a HESM, design a controller, model and simulate the controller, use the controller on a custom tabletop testbed implementation of a HESM, and finally implement the controller on a real COTS integrated system. It is hypothesized in this work that a system level control can be achieved to satisfy the requirements of an equivalent energy storage device in a pulsed power naval setting while offering the previously mentioned advantages that a HESM contributes. The result of this work is a testbed, which can be utilized to easily evaluate different energy storage chemistries and power system integration techniques.

Chapter 2: Mathematical Model of a HESM

The first step to developing a controller for the system is to mathematically model it. Other researchers have spent time modeling this system mathematically such as [35], which presented a detailed small-signal mathematical model that represents the dynamics of the converter interfaced energy storage system around a steady-state operating point. Their model considered the variations in the battery current, supercapacitor current, and DC load bus voltage as the state variables, the variations in the power converter's duty cycle as the input, and the variations in the battery voltage, supercapacitor voltage, and load current as external disturbances. Modeling this system mathematically can be difficult for a multitude of reasons. Considerations must be made with regards to the level of detail to include in the model and degree of linearizing applied to the system. In the case of a HESM there is the additional problem of properly representing the energy storage devices. Typically, when power electronics converters are mathematically described in an entry level course, they utilize an ideal voltage source as an input and a common resistor as a load, but with a HESM, energy storage devices serve as both the source and the load and exhibit bi-directional power flow. Alone, the system can be considered passive, but with the addition of power generation, there are still opportunities to cause enormous instabilities. Approaching this system mathematically, the ultracapacitor is simple to model in the idea that it is simply a capacitor with a large capacitance and an equivalent series resistance, so it offers no challenge in modeling, but the model of a battery is different. To make it simple for both model description and for controller design, it was decided that the battery model to use would be Saft's RC model of a lithium-ion battery [36]. In this model, they use a bulk

capacitor to describe the large energy storage of the device and they use a few

resistors to model the ESR and chemical impedances along with a second capacitor to

emulate surface capacitance of the terminals. The HESM schematic that will be used to

mathematically model the system can be seen in Figure 3.
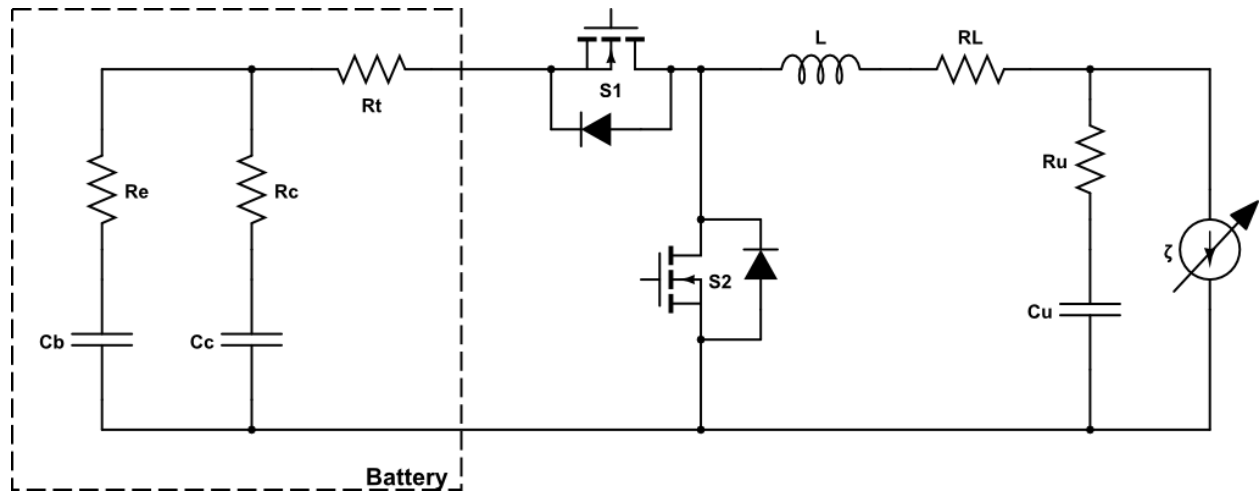
Figure 3: Schematic of HESM for mathematical modeling

Where,

C_b	Bulk Capacitance	S_2	Boost Converter Switch
C_c	Surface Capacitance	L	Power Inductor
R_e	Electrochemical Resistance	R_L	ESR of Inductor
R_c	Double Layer Resistance	C_u	Ultracapacitor
R_t	Terminal Resistance	R_u	ESR of Ultracapacitor
S_1	Buck Converter Switch	ζ	Load and/or Generation Disturbance

Since there are two switches that can have binary states, this system is considered time

varying. The sets of equations that describe the system in each of the binary states are

shown below, splitting up into the different states of the system, based on the directions

of power flow of the system and the state of the switches.

In the equations shown below, the states are defined as:

$$\begin{bmatrix} \dot{x}_1 \\ \dot{x}_2 \\ \dot{x}_3 \\ \dot{x}_4 \end{bmatrix} = \begin{bmatrix} i_L \\ V_u \\ V_b \\ V_c \end{bmatrix} \tag{1}$$

There are essentially two systems to consider when mathematically describing this HESM. The first system is the buck converter system, where power flows from the battery to the ultracapacitor. The second system is the boost converter system, where the power flows from the ultracapacitor to the battery. These systems are used separately and exist separately and therefore will be analyzed separately with different designations for current flow and voltage polarities. The branch currents designated in the buck converter system can be seen in Figure 4 and the designations made for the boost converter system can be seen in Figure 5. Analysis will begin with analyzing the power flow from the battery to the ultracapacitor and will then be followed with analyzing the power flow from the ultracapacitor to the battery. MOSFET switches are considered ideal in this analysis and therefore are assumed to have no voltage drop during conduction. The body diodes of the MOSFETs are also considered to be ideal and therefore will be assumed to have no forward breakdown voltage, no voltage drop during conduction, and infinite reverse breakdown voltage.
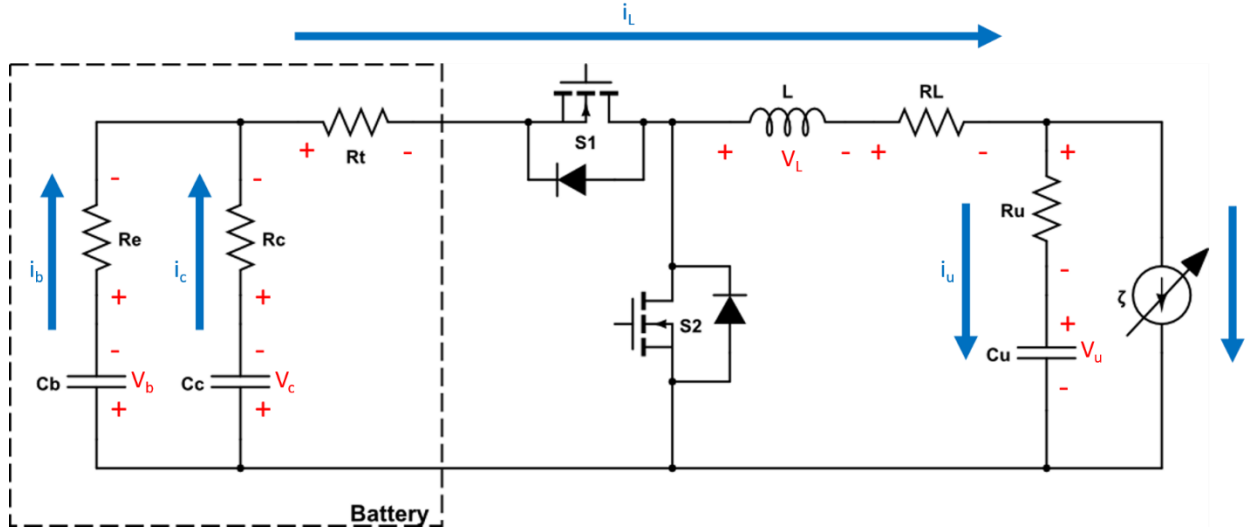
Figure 4: Branch current designations for buck converter system

State 1: The power flows from the battery to the ultracapacitor; S_1 is on and S_2 is off

$$V_c + R_c i_c + R_t i_L + V_L + R_L i_L + R_u i_u + V_u = 0 \tag{2}$$

$$\rightarrow \boxed{\dot{x}_1(L) + \dot{x}_2(R_u C_u) + \dot{x}_4(R_c C_c) = x_1(-R_L - R_t) - x_2 - x_4} \tag{3}$$

$$i_L - i_u - \zeta = 0 \tag{4}$$

$$\rightarrow \boxed{\dot{x}_2(-C_u) = -x_1 + \zeta} \tag{5}$$

$$V_b + R_e i_b - R_c i_c - V_c = 0 \tag{6}$$

$$\rightarrow \boxed{\dot{x}_3(R_e C_b) + \dot{x}_4(-R_c C_c) = -x_3 + x_4} \tag{7}$$

$$i_b + i_c - i_L = 0 \tag{8}$$

$$\rightarrow \boxed{\dot{x}_3(C_b) + \dot{x}_4(C_c) = x_1} \tag{9}$$

These equations are in the form $M\dot{x} = Ax + F\zeta$. Where,

$$M_1 = \begin{bmatrix} L & R_u C_u & 0 & R_c C_c \\ 0 & -C_u & 0 & 0 \\ 0 & 0 & R_e C_b & -R_c C_c \\ 0 & 0 & C_b & C_c \end{bmatrix} \tag{10}$$

$$A_1 = \begin{bmatrix} -R_L - R_t & -1 & 0 & -1 \\ -1 & 0 & 0 & 0 \\ 0 & 0 & -1 & 1 \\ 1 & 0 & 0 & 0 \end{bmatrix} \tag{11}$$

22

$$F_1 = \begin{bmatrix} 0 \\ 1 \\ 0 \\ 0 \end{bmatrix} \tag{12}$$

$$\hat{A}_1 \equiv M_1^{-1}A_1$$

$$= \begin{bmatrix} \dfrac{\left(\dfrac{R_e^2}{R_c + R_e} - R_e - R_L - R_t - R_u\right)}{L} & \dfrac{-1}{L} & \dfrac{-R_c}{L(R_c + R_e)} & \dfrac{-R_e}{L(R_c + R_e)} \\[4mm] \dfrac{1}{C_{UC}} & 0 & 0 & 0 \\[4mm] \dfrac{\left(1 - \dfrac{R_e}{(R_c + R_e)}\right)}{C_b} & 0 & \dfrac{-1}{C_b(R_c + R_e)} & \dfrac{1}{C_b(R_c + R_e)} \\[4mm] \dfrac{R_e}{C_c(R_c + R_e)} & 0 & \dfrac{1}{C_c(R_c + R_e)} & \dfrac{-1}{C_c(R_c + R_e)} \end{bmatrix} \tag{13}$$

$$\hat{F}_1 \equiv M_1^{-1}F_1 = \begin{bmatrix} \dfrac{R_u}{L} \\[3mm] \dfrac{-1}{C_u} \\[3mm] 0 \\ 0 \end{bmatrix} \tag{14}$$

This mathematical model describes the relationship of the states of the system when the switch of the "buck converter" is switched closed. To see the relationships of the system while the switch is open, State 2 is considered.

State 2: The power flows from the battery to the ultracapacitor; S₁ is off and S₂ is off

$$V_L + R_L i_L + R_u i_u + V_u = 0 \tag{15}$$

$$\rightarrow \boxed{\dot{x}_1(L) + \dot{x}_2(R_u C_u) = x_1(-R_L) - x_2} \tag{16}$$

$$i_L - i_u - \zeta = 0 \tag{17}$$

$$\rightarrow \boxed{\dot{x}_2(-C_u) = -x_1 + \zeta} \tag{18}$$

$$V_b + R_e i_b - R_c i_c - V_c = 0 \tag{19}$$

$$\rightarrow \boxed{\dot{x}_3(R_e C_b) + \dot{x}_4(-R_c C_c) = -x_3 + x_4} \tag{20}$$

23

$$i_b + i_c = 0 \tag{21}$$

$$\rightarrow \boxed{\dot{x}_3(C_b) + \dot{x}_4(C_c) = 0} \tag{22}$$

These equations are in the form $M\dot{x} = Ax + F\zeta$. Where,

$$M_2 = \begin{bmatrix} L & R_u C_u & 0 & 0 \\ 0 & -C_u & 0 & 0 \\ 0 & 0 & R_e C_b & -R_c C_c \\ 0 & 0 & C_b & C_c \end{bmatrix} \tag{23}$$

$$A_2 = \begin{bmatrix} -R_L - R_t & -1 & 0 & 0 \\ -1 & 0 & 0 & 0 \\ 0 & 0 & -1 & 1 \\ 0 & 0 & 0 & 0 \end{bmatrix} \tag{24}$$

$$F_2 = \begin{bmatrix} 0 \\ 1 \\ 0 \\ 0 \end{bmatrix} \tag{25}$$

$$\hat{A}_2 \equiv M_2^{-1} A_2 = \begin{bmatrix} \dfrac{(-R_L - R_u)}{L} & \dfrac{-1}{L} & 0 & 0 \\ \dfrac{1}{C_u} & 0 & 0 & 0 \\ 0 & 0 & \dfrac{-1}{C_b(R_c + R_e)} & \dfrac{1}{C_b(R_c + R_e)} \\ 0 & 0 & \dfrac{1}{C_c(R_c + R_e)} & \dfrac{-1}{C_c(R_c + R_e)} \end{bmatrix} \tag{26}$$

$$\hat{F}_2 \equiv M_2^{-1} F_2 = \begin{bmatrix} \dfrac{R_u}{L} \\ -\dfrac{1}{C_u} \\ 0 \\ 0 \end{bmatrix} \tag{27}$$

To calculate the outputs, there are only really two values that are of any concern in this system during this power flow direction. In this case, only the DC bus voltage and the inductor current are of interest.

These values can be found with the equations,

$$y = R_u i_u + V_u \qquad (28)$$

$$\rightarrow R_u C_u \dot{x}_2 + x_2 \qquad (29)$$

From equation 5,

$$\dot{x}_2 = \frac{x_1}{C_u} - \frac{\zeta}{C_u} \qquad (30)$$

$$y = R_u x_1 + x_2 - R_u \zeta \qquad (31)$$

This output is arranged in the format of $y = Cx + G\zeta$ where,

$$C_{1,2} = \begin{bmatrix} R_u & 1 & 0 & 0 \\ 1 & 0 & 0 & 0 \end{bmatrix} \qquad (32)$$

$$G_{1,2} = \begin{bmatrix} 0 \\ -R_u \\ 0 \\ 0 \end{bmatrix} \qquad (33)$$

Since this system is binary in nature and literally changes the plant during each state, it can be represented as an average between these two states where the averaging number is determined by the percentage of time during a cycle spent in each state. Since these switches are driven by pulsed width modulation, the duty cycle of this signal can be considered the percentage of time in a period that each state exists inside. Another note is that there is no controllable input to this system besides the duty cycle of each switch. This is an interesting problem to overcome and is a suggested topic of research for future work.

For now, the combination of these two states for power flowing from the battery towards the ultracapacitor can be described by the equations:

$$\dot{x} = \left(d\hat{A}_1 + (1-d)\hat{A}_2\right)x + F\zeta \tag{34}$$

$$\rightarrow \dot{x} = \left(d\hat{A}_1 x + \hat{A}_2 x - d\hat{A}_2 x\right) + F\zeta \tag{35}$$

$$\rightarrow \dot{x} = \left(\hat{A}_2 x + d(\hat{A}_1 - \hat{A}_2)x\right) + F\zeta \tag{36}$$

$$\hat{A}_1 - \hat{A}_2 = \begin{bmatrix} \dfrac{\left(\dfrac{R_e^2}{R_c + R_e} - R_e - R_t\right)}{L} & 0 & -\dfrac{R_c}{L(R_c + R_e)} & -\dfrac{R_e}{L(R_c + R_e)} \\ 0 & 0 & 0 & 0 \\ \dfrac{\left(1 - \dfrac{R_e}{(R_c + R_e)}\right)}{C_b} & 0 & 0 & 0 \\ \dfrac{R_e}{C_c(R_c + R_e)} & 0 & 0 & 0 \end{bmatrix} \tag{37}$$

The next two states describe the system when power flows from the ultracapacitor to the battery, in other words the boost converter system. Keeping this in mind, the branch current designations change, as seen in Figure 5.
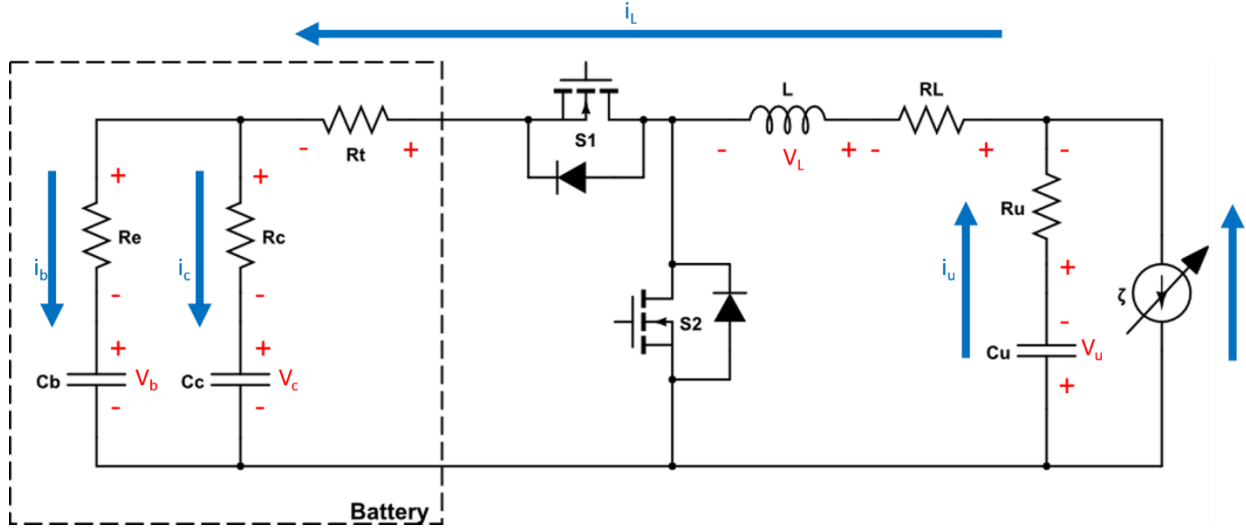
Figure 5: Branch current designations for boost converter system

State 3: The power flows from the ultracapacitor to the battery; S_1 is off and S_2 is on

$$V_u + R_u i_u + R_L i_L + V_L = 0 \tag{38}$$

$$\rightarrow \boxed{\dot{x}_1(L) + \dot{x}_2(R_u C_u) = x_1(-R_L) - x_2} \tag{39}$$

$$-i_L + i_u + \zeta = 0 \tag{40}$$

$$\rightarrow \boxed{\dot{x}_2(C_u) = x_1 - \zeta} \tag{41}$$

$$-V_c - R_c i_c + R_e i_b + V_b = 0 \tag{42}$$

$$\rightarrow \boxed{\dot{x}_3(R_e C_b) + \dot{x}_4(-R_c C_c) = -x_3 + x_4} \tag{43}$$

$$-i_b - i_c = 0 \tag{44}$$

$$\rightarrow \boxed{\dot{x}_3(-C_b) + \dot{x}_4(-C_c) = 0} \tag{45}$$

These equations are in the form $M\dot{x} = Ax + F\zeta$. Where,

$$M_3 = \begin{bmatrix} L & R_u C_u & 0 & R_c C_c \\ 0 & C_u & 0 & 0 \\ 0 & 0 & R_e C_b & -R_c C_c \\ 0 & 0 & -C_b & -C_c \end{bmatrix} \quad\quad (46)$$

$$A_3 = \begin{bmatrix} -R_L & -1 & 0 & 0 \\ 1 & 0 & 0 & 0 \\ 0 & 0 & -1 & 1 \\ 0 & 0 & 0 & 0 \end{bmatrix} \quad\quad (47)$$

$$F_3 = \begin{bmatrix} 0 \\ -1 \\ 0 \\ 0 \end{bmatrix} \quad\quad (48)$$

$$\hat{A}_3 \equiv M_3^{-1} A_3 = \begin{bmatrix} \dfrac{(-R_L - R_u)}{L} & -\dfrac{1}{L} & 0 & 0 \\ -\dfrac{1}{C_u} & 0 & 0 & 0 \\ 0 & 0 & \dfrac{-1}{C_b(R_c + R_e)} & \dfrac{1}{C_b(R_c + R_e)} \\ 0 & 0 & \dfrac{1}{C_c(R_c + R_e)} & \dfrac{-1}{C_c(R_c + R_e)} \end{bmatrix} \quad\quad (49)$$

$$\hat{F}_3 \equiv M_3^{-1} F_3 = \begin{bmatrix} \dfrac{R_u}{L} \\ -\dfrac{1}{C_u} \\ 0 \\ 0 \end{bmatrix}$$

$$\hat{F}_3 \equiv M_3^{-1} F_3 = \begin{bmatrix} \dfrac{R_u}{L} \\ -\dfrac{1}{C_u} \\ 0 \\ 0 \end{bmatrix} \quad\quad (50)$$

This mathematical model describes the relationship of the states of the system when the switch of the "boost converter" is switched closed. To see the relationships of the system while the switch is open, State 4 is considered.

State 4: The power flows from the ultracapacitor to the battery; S_1 is off and S_2 is off

$$V_c + R_c i_c + R_t i_L + V_L + R_L i_L + R_u i_u + V_u = 0 \qquad (51)$$

$$\rightarrow \boxed{\dot{x}_1(L) + \dot{x}_2(R_u C_u) + \dot{x}_4(R_c C_c) = x_1(-R_L - R_t) - x_2 - x_4} \qquad (52)$$

$$-i_L + i_u + \zeta = 0 \qquad (53)$$

$$\rightarrow \boxed{\dot{x}_2(C_u) = x_1 - \zeta} \qquad (54)$$

$$V_b + R_e i_b - R_c i_c - V_c = 0 \qquad (55)$$

$$\rightarrow \boxed{\dot{x}_3(R_e C_b) + \dot{x}_4(-R_c C_c) = -x_3 + x_4} \qquad (56)$$

$$-i_b - i_c + i_L = 0 \qquad (57)$$

$$\rightarrow \boxed{\dot{x}_3(-C_b) + \dot{x}_4(-C_c) = -x_1} \qquad (58)$$

These equations are in the form $M\dot{x} = Ax + F\zeta$. Where,

$$M_4 = \begin{bmatrix} L & R_u C_u & 0 & R_c C_c \\ 0 & C_u & 0 & 0 \\ 0 & 0 & R_e C_b & -R_c C_c \\ 0 & 0 & -C_b & -C_c \end{bmatrix} \qquad (59)$$

$$A_4 = \begin{bmatrix} -R_L - R_t & -1 & 0 & -1 \\ 1 & 0 & 0 & 0 \\ 0 & 0 & -1 & 1 \\ -1 & 0 & 0 & 0 \end{bmatrix} \qquad (60)$$

$$F_4 = \begin{bmatrix} 0 \\ -1 \\ 0 \\ 0 \end{bmatrix} \qquad (61)$$

$$\hat{A}_4 \equiv M_4^{-1} A_4 = \begin{bmatrix} \dfrac{\left(\dfrac{R_e^2}{R_c + R_e} - R_e - R_t - R_u\right)}{L} & \dfrac{-1}{L} & \dfrac{-R_c}{L(R_c + R_e)} & \dfrac{-R_e}{L(R_c + R_e)} \\ \dfrac{1}{C_u} & 0 & 0 & 0 \\ \dfrac{\left(1 - \dfrac{R_e}{(R_c + R_e)}\right)}{C_b} & 0 & \dfrac{-1}{C_b(R_c + R_e)} & \dfrac{1}{C_b(R_c + R_e)} \\ \dfrac{R_e}{C_c(R_c + R_e)} & 0 & \dfrac{1}{C_c(R_c + R_e)} & \dfrac{-1}{C_c(R_c + R_e)} \end{bmatrix} \qquad (62)$$

$$\hat{F}_4 \equiv M_2^{-1} F_2 = \begin{bmatrix} \dfrac{R_u}{L} \\ \dfrac{-1}{C_u} \\ 0 \\ 0 \end{bmatrix} \qquad (63)$$

To calculate the outputs, a similar approach is taken to the previous power flow direction "system". In this case, only the battery bus voltage and the inductor current are of interest. The main difference in this case is that the battery voltage changes based not only on the states of the system, but whether or not the battery is "conducting". This is due to the ESR drop dictated by R_t. During state 3, where the battery is not conducting, the output is defined as,

$$y = R_c i_c + V_u \qquad (64)$$
$$\rightarrow R_c C_c \dot{x}_4 + x_4 \qquad (65)$$

From equation 43 and 45,

$$\dot{x}_4 = \frac{-\dot{x}_3 C_b}{C_c} \qquad (66)$$

$$\dot{x}_3 = -\frac{x_3}{R_e C_b} + \frac{x_4}{R_e C_b} + \frac{\dot{x}_4 R_c C_c}{R_e C_b} \qquad (67)$$

These equations can be rearranged to obtain,

$$\dot{x}_4 = \frac{x_3 - x_4}{C_c (R_e + R_c)} \qquad (68)$$

$$y = \frac{R_c x_3}{R_e + R_c} - \frac{R_c x_4}{R_e + R_c} + x_4 \qquad (69)$$

This output is arranged in the format of $y = Cx + G\zeta$ where,

$$C_3 = \begin{bmatrix} 0 & 0 & \dfrac{R_c}{R_e + R_c} & 1 + \dfrac{R_c}{R_e + R_c} \\ 1 & 0 & 0 & 0 \end{bmatrix} \tag{70}$$

$$G_3 = 0 \tag{71}$$

This describes the battery bus and the inductor current while the battery is conducting in a recharge state. To define the system during a non-conducting time the equations are,

$$y = R_t i_L + R_c i_c + V_u \tag{72}$$

$$\rightarrow R_t x_1 + R_c C_c \dot{x}_4 + x_4 \tag{73}$$

From equation 56 and 58,

$$\dot{x}_4 = \frac{x_1}{C_c} - \frac{\dot{x}_3 C_b}{C_c} \tag{74}$$

$$\dot{x}_3 = -\frac{x_3}{R_e C_b} + \frac{x_4}{R_e C_b} + \frac{\dot{x}_4 R_c C_c}{R_e C_b} \tag{75}$$

These equations can be rearranged to obtain,

$$\dot{x}_4 = \frac{R_e x_1 + x_3 - x_4}{R_e C_c + R_c C_c} \tag{76}$$

$$y = x_1 \left(R_t + \frac{R_e R_c}{R_e + R_c} \right) + x_3 \left(\frac{R_c}{R_e + R_c} \right) + x_4 \left(1 + \frac{R_c}{R_e + R_c} \right) \tag{77}$$

31

This output is arranged in the format of $y = Cx + G\zeta$ where,

$$C_4 = \begin{bmatrix} R_t + \dfrac{R_e R_c}{R_e + R_c} & 0 & \dfrac{R_c}{R_e + R_c} & 1 + \dfrac{R_c}{R_e + R_c} \\ 1 & 0 & 0 & 0 \end{bmatrix} \quad (78)$$

$$G_4 = 0 \quad (79)$$

Again, this system is binary in nature and can be represented as an average between these two states where the averaging number is determined by the percentage of time during a cycle spent in each state. The combination of these two states for power flowing from the ultracapacitor towards the battery can be described by the equations:

$$\dot{x} = \left(d\hat{A}_3 + (1-d)\hat{A}_4\right)x + F\zeta \quad (80)$$

$$\rightarrow \dot{x} = \left(d\hat{A}_3 x + \hat{A}_4 x - d\hat{A}_4 x\right) + F\zeta \quad (81)$$

$$\rightarrow \dot{x} = \left(\hat{A}_3 x + d(\hat{A}_3 - \hat{A}_4)x\right) + F\zeta \quad (82)$$

$$\hat{A}_3 - \hat{A}_4 = \begin{bmatrix} \dfrac{\left(\dfrac{-R_e^2}{R_c + R_e} + R_e + R_L(-R_t - 1)\right)}{L} & 0 & \dfrac{R_c}{L(R_c + R_e)} & \dfrac{R_e}{L(R_c + R_e)} \\ \dfrac{-2}{C_u} & 0 & 0 & 0 \\ \dfrac{\left(\dfrac{R_e}{(R_c + R_e)} - 1\right)}{C_b} & 0 & 0 & 0 \\ \dfrac{-R_e}{C_c(R_c + R_e)} & 0 & 0 & 0 \end{bmatrix} \quad (83)$$

Although it is fairly straight forward to mathematically describe this system in its separate states, it is very difficult to design a controller for this system given its non-linear and time varying qualities. There are many advanced methods of control that have been developed to achieve control of these types of converters such as backstepping control, slide mode control, or optimal control techniques such as the Pontryagin's Minimum Principle, but since it is intended to eventually transition the

32

controller design to a COTS system whose internals are either unknown or difficult to

obtain, for the purposes of the work presented here, it does not make sense to spend

time with these advanced control concepts when the time averaged model works just

fine with using a simple PI controller. Although this mathematical approach has given

insight to the system and provided a glimpse into the dynamics, it was decided at this

point to move forward with a circuit simulator such as Simulink's SimPowerSystems,

which offers more dynamic electronic component models and a more robust

environment for implementing the desired system level controls that will be eventually

implemented on top of a COTS system.

Chapter 3: Simulink SimPowerSystems Model

While this work aims to address the need for a system level control for COTS devices, in order to simulate the controller in MATLAB/Simulink, it is necessary to use a simplified model of a HESM and its power converters. In the material below, MATLAB/Simulink's SimPowerSystems toolbox will be utilized instead of a mathematical model.

A generic schematic of a HESM is shown in Figure 6. In this schematic, a simple buck-boost converter is utilized in order to give the controller a method of bi-directional voltage and current control. The load and the generator are tied together as one variable current source/sink as the system which the HESM augments can be seen as a generalized external power disturbance. When mathematically modeling this system, in similar fashion to [35], C1 and C2, the output capacitors for each direction of power flow, hold the state variables of the battery bus voltage and the DC load bus voltage and L, the power inductor, holds the state variable of the power converter current, and the combined current sourcing or sinking from the load and generation is the external disturbance, denoted as ζ. For instance, when $\zeta > 0$, the generator is producing more current than the load is drawing, but when $\zeta < 0$, the load is drawing more current than the generation is producing. There are multiple equations to describe this circuit during operation, based on the state of the switches. To demonstrate the variation of this system over time, the mathematical equations that represent these states are shown below. For simplicity, the system will be evaluated in each direction of power flow while treating the load ESD as an omitted independent variable, shown in the circuit as V_1 and V_2.
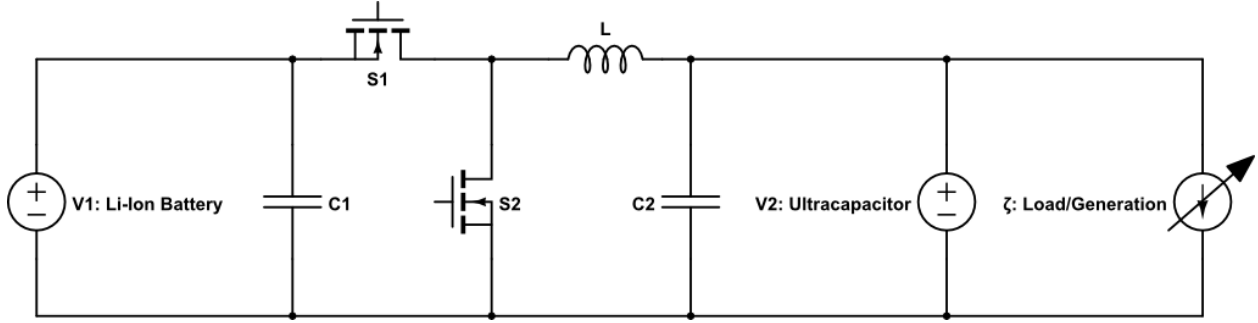
Figure 6: Schematic of a generic battery/ultracapacitor HESM

1. *State 1: When power flows from the battery towards the ultracapacitor and when S_1 is on and S_2 is off,*

$$L\frac{di_L}{dt} = V_{C1} - V_{C2} \qquad (84)$$

$$C_1\frac{dV_{C1}}{dt} = i_L - i_{V1} \qquad (85)$$

$$C_2\frac{dV_{C2}}{dt} = i_L - i_{V2} - \zeta \qquad (86)$$

2. *State 2: When power flows from the battery towards the ultracapacitor and when S_1 is off and S_2 is off,*

$$L\frac{di_L}{dt} = -V_{C2} \qquad (87)$$

$$C_1\frac{dV_{C1}}{dt} = -i_{V1} \qquad (88)$$

$$C_2\frac{dV_{C2}}{dt} = i_L - i_{V2} - \zeta \qquad (89)$$

3. *State 3: When power flows from the ultracapacitor towards the battery and when S_1 is off and S_2 is on,*

$$L\frac{di_L}{dt} = V_{C2} \tag{90}$$

$$C_1\frac{dV_{C1}}{dt} = -i_{V1} \tag{91}$$

$$C_2\frac{dV_{C2}}{dt} = i_{V2} - i_L - \zeta \tag{92}$$

4. *State 4: When power flows from the ultracapacitor towards the battery and when S_1 is off and S_2 is off,*

$$L\frac{di_L}{dt} = V_{C2} - V_{C1} \tag{93}$$

$$C_1\frac{dV_{C1}}{dt} = i_L - i_{V1} \tag{94}$$

$$C_2\frac{dV_{C2}}{dt} = i_{V2} - i_L - \zeta \tag{95}$$

These mathematical equations are presented here to reinforce the idea that this system is time varying, with four different plant descriptions, depending on the state of 2 switches. Although there are mathematical methods in which these equations could be combined to produce a time-average model in which the controller could be evaluated, it was decided that a more accurate model could be created using MATLAB/Simulink's SimPowerSystems toolbox for controller evaluation in order to utilize the toolbox's lithium ion battery model and additional component values such as internal impedances. This model would be used to evaluate the performance of system level control. In the work presented here, two different controllers were evaluated. The block diagram for this model can be seen in Figure 11. When designing a HESM, one of the largest

obstacles to overcome is the successful application of system level control. Fuzzy Logic Control (FLC) employs an if-then rule-base with mathematical fuzzification and defuzzification in order to achieve an expert response with a digital controller's speed and efficiency. In other words, it behaves exactly how a human would if they had expert knowledge on the desired behaviors of the system. Fuzzy systems typically achieve utility in assessing more conventional and less complex systems [37], but on occasion, FLC can be useful in a situation where highly complex systems only need approximated and rapid solutions for practical applications. FLC can be particularly useful in nonlinear systems such as this HESM which shifts between 4 different operation states. One key difference between crisp and fuzzy sets is their membership functions. The uniqueness of a crisp set is sacrificed for the flexibility of a fuzzy set. Fuzzy membership functions can be adjusted to maximize the utility for a particular design application. The membership function embodies the mathematical representation of membership in a set using notation Ω_i, where the functional mapping is given by $\mu_{\Omega_i}(x) \in [0,1]$. The symbol $\Omega_i(x)$ is the degree of membership of element x in fuzzy set Ω_i and $\mu_{\Omega_i}(x)$ is a value on the unit interval which measures the degree to which x belongs to fuzzy set Ω_i.

Two fuzzy input sets were defined as the DC bus voltage and the HESM current – these inputs can be seen in Figure 7 and Figure 8. The first input, the DC bus voltage, was a logical choice as maintaining this voltage is critical to all three tasks of the HESM, which is to supply power under all scenarios and to act as a power buffer to transients, as transients will cause deviations in the DC bus voltage. The second input, HESM current, was chosen because of its proportional relativity to the differential change in the bus voltage.

The HESM current can be defined as,

$$i_{HESM} = i_{C2} + i_L \qquad (96)$$

which leads to,

$$\frac{i_{HESM} - i_L}{C_2} = \frac{dV_{C2}}{dt} \qquad (97)$$

where V_{C2} is the DC bus voltage. It is because of this proportional relationship that the HESM current is able to give the controller sensory insight to the direction of the demand for power, giving an increased ability to maintain the voltage of the DC bus, similar to what a traditional PID controller would be able to offer.
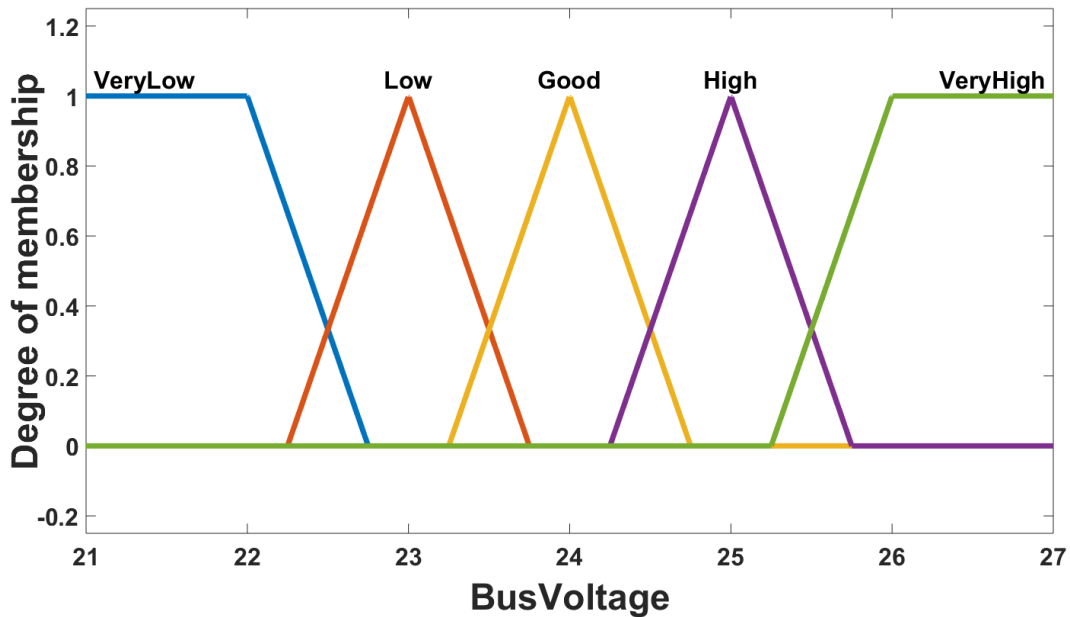
Figure 7: First input fuzzy membership function – the voltage of the output bus of the HESM
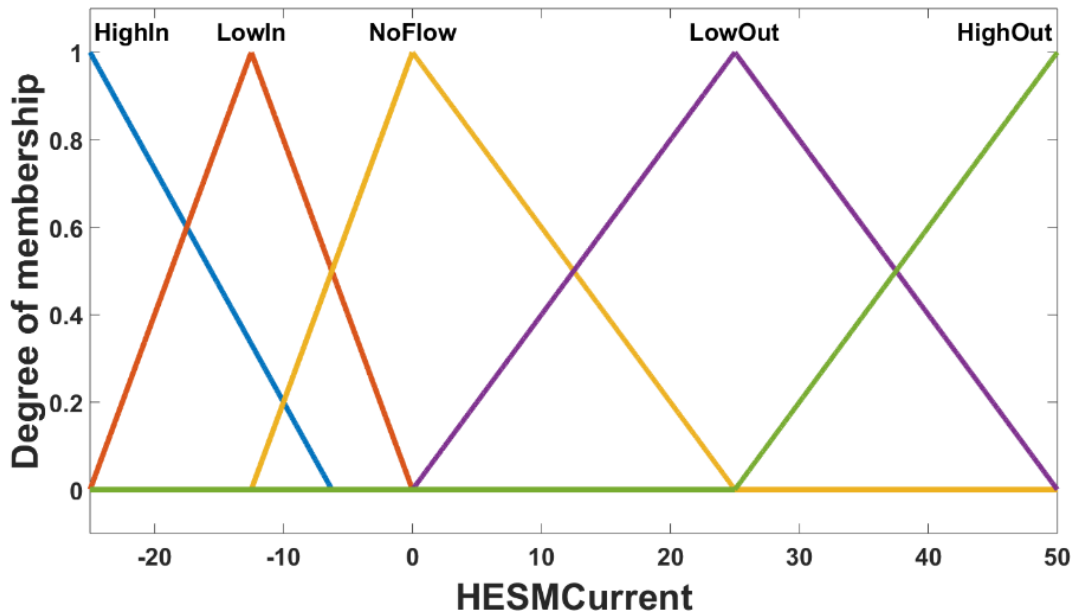
Figure 8: Second input fuzzy membership function – the current flowing in or out of the HESM

The output fuzzy set was chosen to be the battery current limit as this gives a superb amount of control over the HESM. The membership function describing this relationship can be seen in Figure 9. With the battery being actively limited in the direction and magnitude, all remaining HESM power must come from the ultracapacitor. This essentially gives full, albeit indirect, control over the power flow to and from all ESDs associated with the HESM.
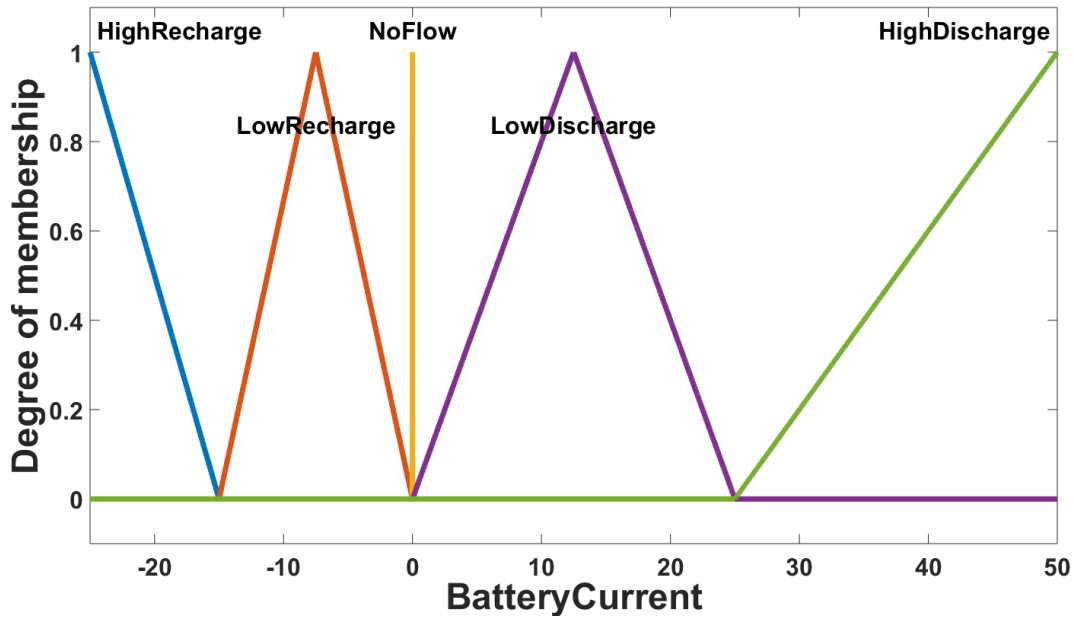
Figure 9: Output fuzzy membership function – the current direction and limit of the battery

The controller's inputs and outputs are mapped together using a rule-base. That is to say that for a given set of input conditions, there should be a relative output condition. Since it is possible for values to lie in-between conditions, there may be times when multiple output conditions are met. In this case, the FLC determines the value by computing the centroid of mass in the membership functions [38, 39]. The set of rules being used in this controller is seen in Table 1. The process of relating these input values to a rule-base is called fuzzification. Once the rule-base is in place, the controller's input versus output can be observed as seen in Figure 10. The plateau area represents high discharge while the valley area represents high recharge. The process of relating the output membership function to a value is called defuzzification.

Table 1: Fuzzy Logic Rule-Base

		Bus Voltage				
		Very Low	Low	Good	High	Very High
HESM Current	High In	No Flow	Low Recharge	High Recharge	High Recharge	High Recharge
	Low In	Low Discharge	No Flow	Low Recharge	High Recharge	High Recharge
	No Flow	High Discharge	Low Discharge	No Flow	Low Recharge	High Recharge
	Low Out	High Discharge	High Discharge	Low Discharge	No Flow	Low Recharge
	High Out	High Discharge	High Discharge	High Discharge	Low Discharge	No Flow
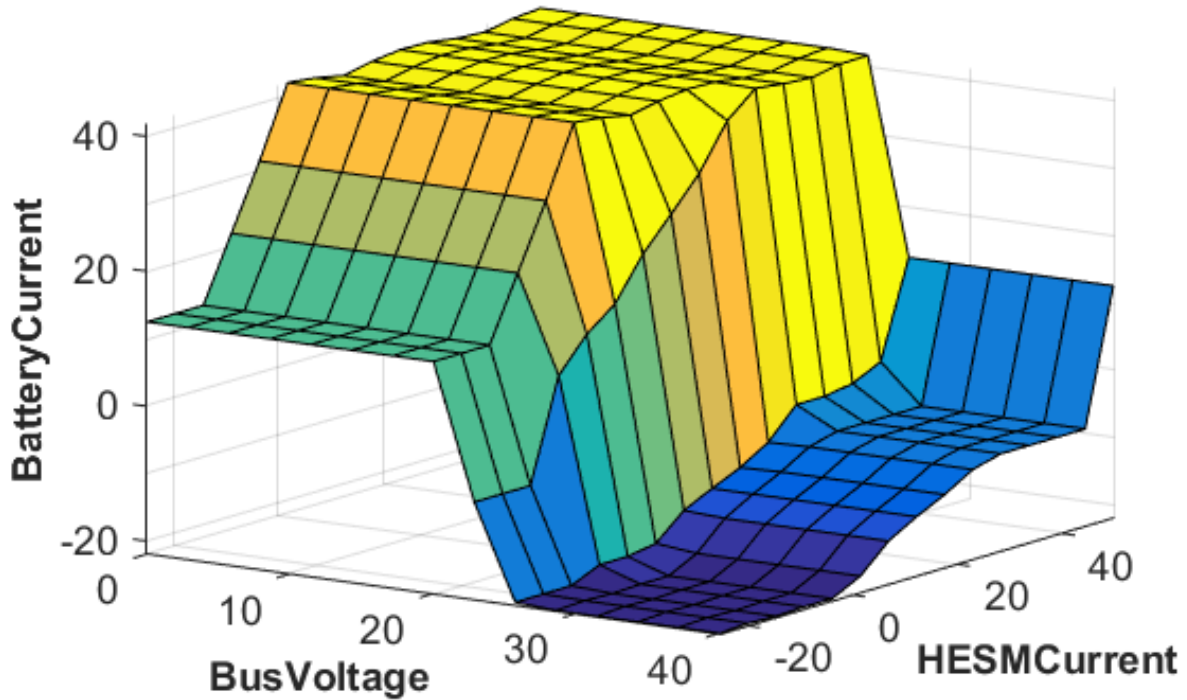
Figure 10: Fuzzy Logic Controller input vs. output relationship

In order to test the controller an experiment was designed to mimic a typical naval pulsed power load. In this case, a pulse train load profile of 5 seconds at high load power draw and 1 second of low load power draw was simulated. To compare the FLC to a traditional type of state-machine controller, the experiment introduces a shift in the power demand halfway through the test.
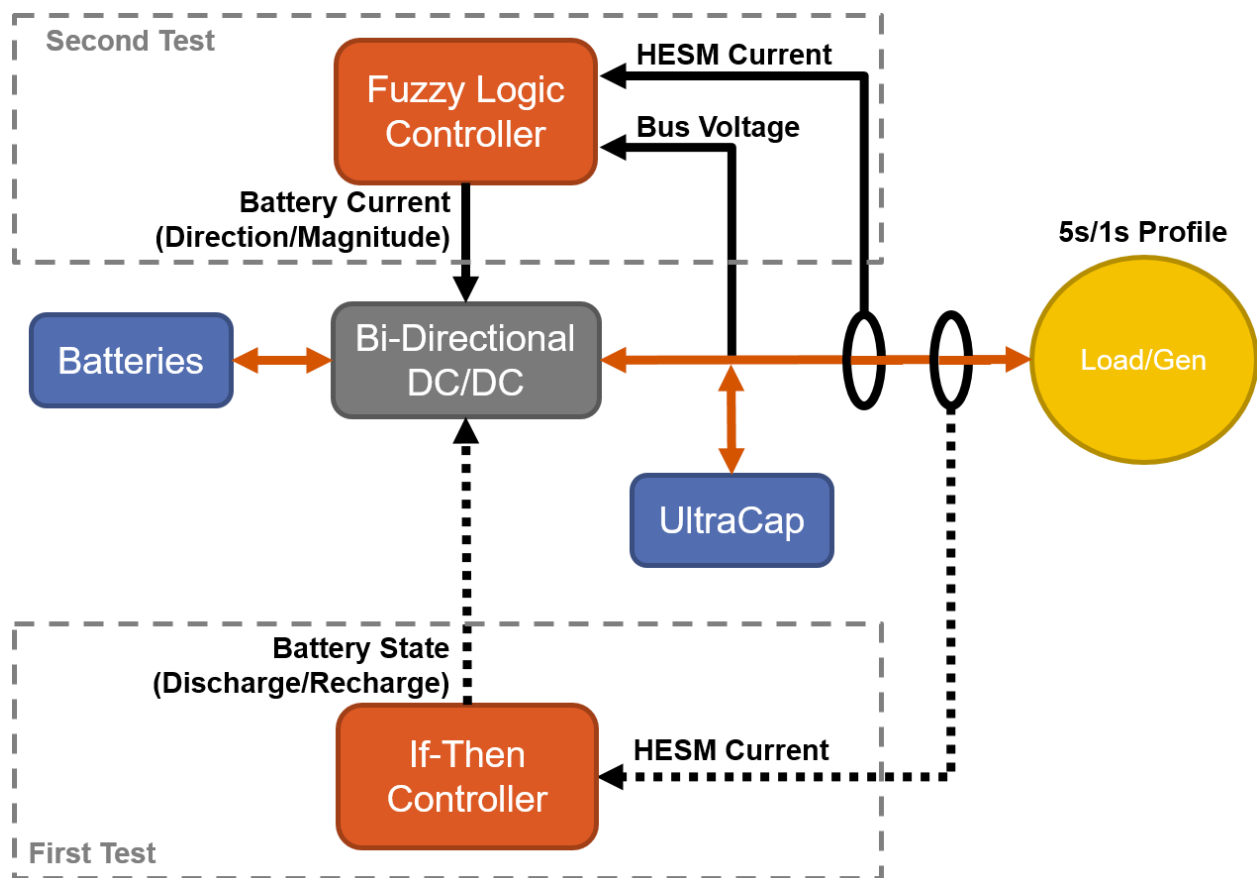
Figure 11: Block diagram of HESM experiment in SimPowerSystems toolbox

Initial investigation into acquiring parts for hardware validations lead to the values chosen for this simulation. This investigation occurred with the intention of validating this controller with real hardware for future investigations. The values chosen for the

simulation can be seen in Table 2. The voltage selections of the devices were chosen

based on preliminary investigation into part availability to achieve a hardware validation,

which will be discussed further in the next section. The lithium-ion battery was initialized

at a 50% state-of-charge to ensure that it would both be able to provide power as well

as sink power during "recharge" periods. The load generation profile of 5 seconds on

and 1 second off is reflective of a typical pulsed power load seen in a naval setting. The

PI gains of the low level converter controllers were achieved by starting with the Zeigler-

Nichols method and then by slightly tuning to achieve the desired responses.

Table 2: Simulation values

Component	Value
Lithium Ion Battery	36 V_{nom}, 15 Ahr, 50% SOC
Ultracapacitor	24 V_{nom}, 29 F, 44 mΩ ESR
Load/Generation	5 seconds on, 1 second off, variable currents
Switches	R_{on} = 100 mΩ, f_{sw} = 40 kHz
Inductor	3.4 mH, 1.5 mΩ ESR
Discharge PI Controller	Voltage: k_P = 0.2, k_I = 10 Current: k_P = 1, k_I = 200
Recharge PI Controller	Voltage: k_P = 0.028, k_I = 1.5 Current: k_P = 5, k_I = 1

For comparison, Figure 12 shows the results of the experiment when using a simple if-

then controller and Figure 13 shows the results of the experiment when using the FLC.

Positive currents indicate that a device is sourcing energy and negative currents

indicate that a device is sinking energy. By examination of Figure 12, it is clear to see

that the controller operates satisfactory for the first 30 seconds, where it was designed

to operate, but as soon as the system starts to exhibit behaviors outside of a pre-

determined need, the controller is no longer able to effectively maintain the DC bus

voltage. In addition to the presence of large voltage swings during the change in the pulsed load power draw, there is an overall decay in voltage, which in a real system would lead to a failure to maintain an effective power buffer and therefore lead to either a cascading power failure throughout other components of the integrated power system from over demand, or a larger sizing requirement to accommodate loads outside of pre-determined profiles. In addition to these problems, the generator would also run in an inefficient manner as a change in the voltage would inevitably lead to a change in power generation. As a reminder, the goal of this system is to ensure that a generator's output power can remain relatively constant to improve both efficiency and power quality.
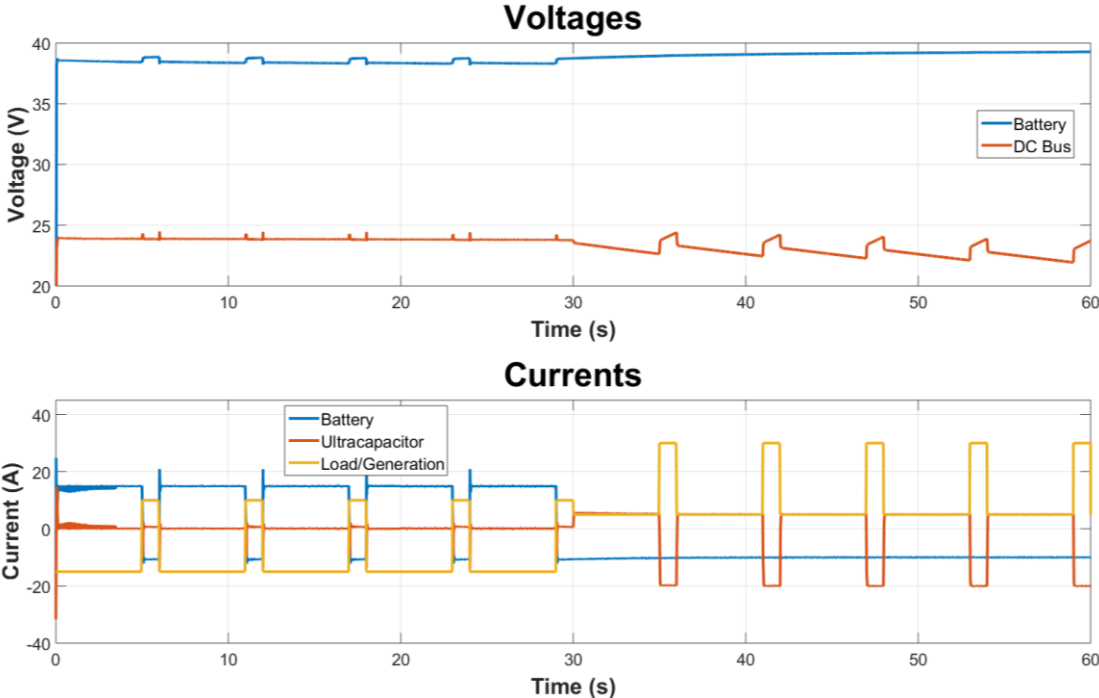
Figure 12: Simulation results with if-then control
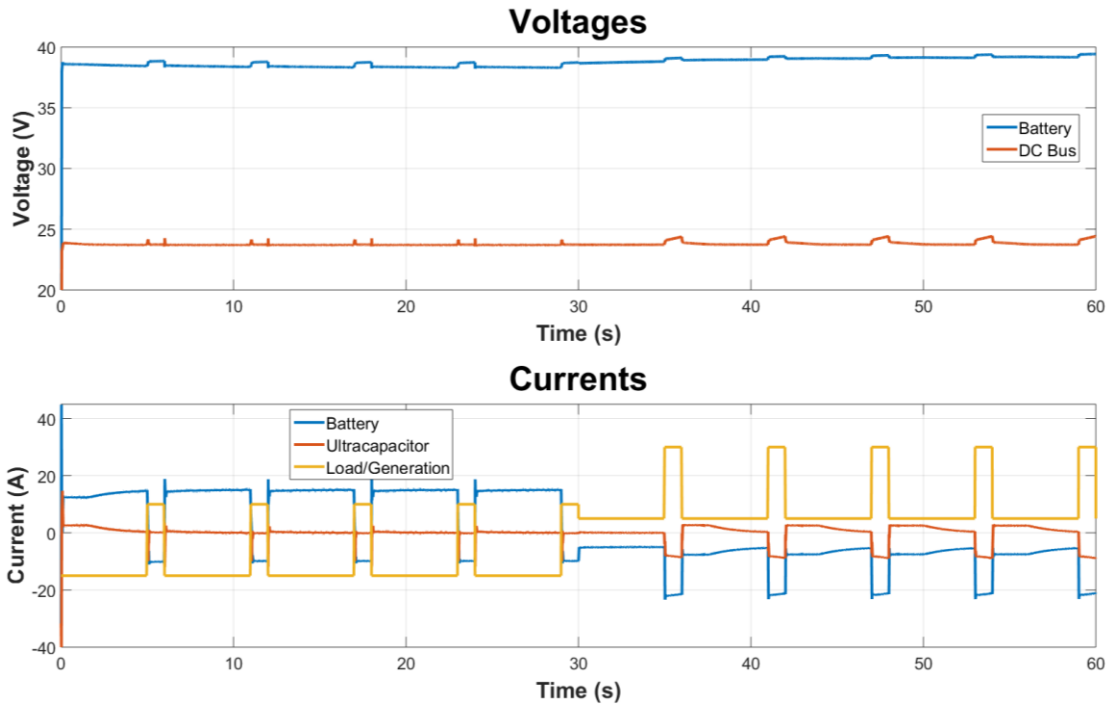
Figure 13: Simulation results using Fuzzy Logic Control

Comparing the results in Figure 12 to Figure 13, it is clear to see that as the load/generation shifts to a different region, the FLC is able to easily accommodate the change. There are certainly some changes in the voltage swing through the pulsed power load profile, but this can be fixed through more meticulous tuning of the FLC. A numerical representation of the results can be seen in Table 3.

Table 3: Numerical experimental results - comparison of if-then control with FLC

If-Then	*Voltage Swing during Pulse*	1.77 V
	Voltage Sag over final 30 seconds	1.84 V
FLC	*Voltage Swing during Pulse*	0.66 V (62% improvement)
	Voltage Sag over final 30 seconds	0.00 V (100% improvement)

To emphasize the fact that this successful level on control corresponds to a constant power output of the generator, a plot showing the power level of the generator is shown in Figure 14. It is clear to see in the plot that the generator's power output remains very constant during the first 30 seconds and has some small changes in the second 30 seconds of the test. This is a direct correspondence to the voltage level of the bus and therefore from here on throughout the paper, it will be assumed that if a constant bus voltage is maintained with this topology, so too will be the power output of the generator.
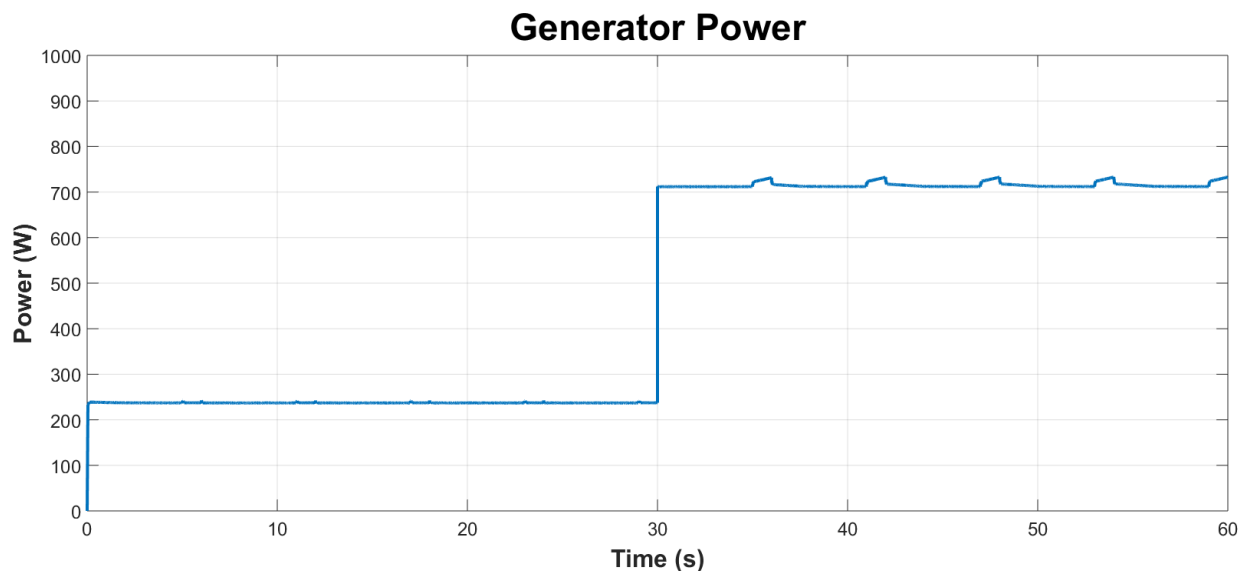
Figure 14: Plot of Generator Power During Fuzzy Logic Test

These results clearly show that the fuzzy logic controller is a promising candidate for system level control of a HESM. One drawback of the FLC is that it is only as accurate as the knowledge of the expert creating it, but through meticulous tuning, even this inadequacy can be overcome. Although these simulations show promise, it was necessary to expand this work into the realm of real hardware in order to gain more insight into the feasibility of this controller.

Chapter 4: Tabletop HESM Experiment

Although simulations can give a great amount of insight into problems, they alone cannot indicate the behavior of a system with certainty. To assign credibility to a simulation, researchers oftentimes undergo a process referred to as validation. In order to validate a model, it is necessary to reconstruct the conditions of a simulation in a physical way. It is important to note that a model is only validated to the degree that a real-world system is evaluated. With this in mind, the next logical step in the process of designing a HESM was to construct a real-world system that closely resembled the simulation conditions. The schematic of the system to be implemented in these tests can be seen in Figure 15. Starting from the left and moving to the right, the batteries implemented in this tabletop testbed were two 12 V Enersys XE16 lead acid batteries placed in parallel. These batteries serve as the energy dense device in the HESM topology. It was originally intended to use 3 of these batteries in series to mimic the simulation, but this was one of the first issues encountered with validating the results of the model. In simulation, many components will act ideal unless you attribute specific characteristics to them. In the real-world, there is no such luck. When constructing this system, it was found that due to both the intrinsic inductances associated with the MOSFET switches (which will be discussed below) and the inductive nature of the "load" (from the power inductor) in each direction, there were significant spikes of voltage that occurred from the drain to the source across the MOSFET switches. These voltage spikes were destroying the MOSFETs and although it was possible to reduce their impact, it was not possible to effectively reduce them enough while the system

operated at the nominal battery voltage of 36 V. Thus, it was decided to use two

batteries in parallel to maintain the bus voltage around 12 V.
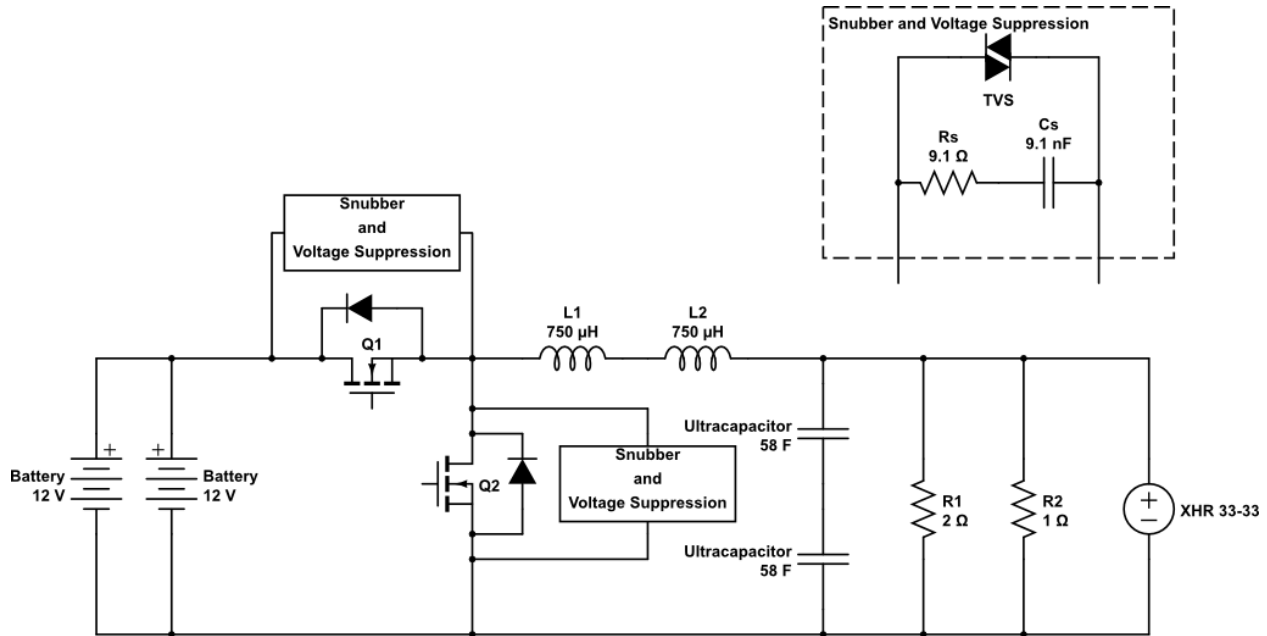
Figure 15: Schematic of the Tabletop HESM

Moving to the right, the MOSFETs used as switches in this testbed were Semikron SKM

111AR power MOSFETs, which were driven by a Semikron SKHI 21A IGBT/MOSFET

driver. These MOSFETs are rated to operate at up to 50 kHz with a current rating of up

to 200 A and a voltage rating of up to 100 V. It is intended to use Q1 as the switch for

the buck converter and Q2 as the switch for the boost converter in the opposite

direction. The body diode of Q2 serves as the freewheeling diode for the buck operation

and the body diode of Q1 serves as the feed-forward diode for the boost converter.

Attached in parallel to both MOSFET switches are RC snubbers and transient voltage

suppression (TVS) diodes. To design the RC snubber, an application note written by

NXP was used [40].

To detail the steps that were used to size this RC snubber,

1. A capacitance was added in parallel with the switch and the ringing frequency before and after the capacitor was added was recorded

    - $C_{added} = 0.027 \mu F$ $f_{ringing\_before} = 1.9 \, MHz$ $f_{ringing\_after} = 737 \, kHz$

2. The leakage capacitance of the MOSFET was calculated

$$C_{leakage} = \frac{C_{added}}{\left(\frac{f_{ringing\_before}}{f_{ringing\_after}}\right)^2 - 1} = 4.782nF \tag{98}$$

3. The leakage inductance of the MOSFET was calculated

$$L_{leakage} = \frac{C_{added}}{\left(2\pi f_{ringing\_before}\right)^2 C_{leakage}} = 1.467 \mu H \tag{99}$$

4. The snubber resistor was calculated, with $\zeta = 1$ for critical damping

$$R_{snubber} = \frac{1}{2\zeta}\sqrt{\frac{L_{leakage}}{C_{leakage}}} = \boxed{8.758\Omega} \tag{100}$$

5. The snubber capacitor was calculated

$$C_{snubber} = \frac{1}{2\pi R_{snubber} f_{ringing\_before}} = \boxed{9564pF} \tag{101}$$

Obviously, there are some issues that are associated with obtaining exact values for capacitors and resistors, so the closest values were chosen of 9100 pF and 9.1 Ω, respectively. The time constant difference between the calculated and the obtainable values changes by only 1.1%, which is negligible. After sizing the snubber, a sufficient TVS diode was chosen to clamp the voltage after reaching 35 V. This allowed a bit of

head room due to the capabilities of the MOSFET, but also allowed the TVS diode to greatly contribute in transferring the otherwise ringing energy that would be lost in the switching dynamics to the power inductor. Moving to the right, the power inductors used in this tabletop testbed were Schaffner 750 µH inductors that are rated up to 50 amps. Two of these inductors were placed in series to achieve an equivalent inductance of 1.5 mH. The next components serve as the power dense device in the HESM topology, the ultracapacitors. The two ultracapacitors used in this testbed are Maxwell BMOD0058 E016 B02 ultracapacitor modules. These modules are rated up to 16.2 V and have 58 F of capacitance. Originally, this ultracapacitor bus was intended to operate at 24 V, so it was necessary to stack them in series to be able to operate at that voltage level, but after re-evaluation, the voltage level was dropped to 6 V. Despite this, it was decided to keep them in a series configuration to try to keep the results similar to the simulation. When thinking back to Figure 6, it is important to remember that the load and generator can be seen as a general disturbance to the HESM. With this in mind, it was decided to keep the load static and allow the power supply to change programmatically. The loads were simple resistors that were on hand in the laboratory, 2 Ω and 1 Ω in parallel (to keep within power ratings). The programmable power supply which mimics the generator is a Xantrex XHR 33-33 power supply which is rated to supply up to 1 kW of power with a voltage rating of up to 33 V and a current rating of up to 33 A while allowing controllability from a GPIB bus. A simple LabVIEW program, which is discussed further in Appendix A, was written in order to allow the user programming capabilities to run the power supply as a pulsed load with different current levels to represent different operational scenarios.

The next step in this process was to implement some level of control and data

acquisition for the system. In order to run the fuzzy logic controller that was used in the

simulations, it would either be necessary to program the fuzzy logic controller in by a

discrete method, or to use a controller that supports fuzzy logic control. Both

MATLAB/Simulink and LabVIEW come to mind as simple controller software

implementations that support a fuzzy logic control scheme. A PC104 was on hand and

supported Simulink's Real Time Operating System (RTOS) and fuzzy logic control so it

made the choice a little simpler. The PC104 uses a Diamond Systems DMM-32X-AT

Analog input/output module with auto-calibration. This module was used for analog

inputs and supports up to 16 differential input channels with a voltage range of +/- 10 V.

In order to read the actual voltages on the testbed, 2 Teledyne LeCroy differential

probes, allow the user to measure up to 700 V at up to 15 MHz, were used to acquire

the voltages and step them down with a 10:1 ratio in order to shift the voltages into a

range that the analog input module can measure. In order to read the currents

throughout the HESM, LEM LA 55-P current transducers were used, which offer a

current conversion ratio of 1:1000 for reading currents up to 50 A. Using a 100 Ω

resistor on the output of the transducer, the differential voltage being measured over the

resistor ranges from +/- 5 V, which is, again, measured by the Diamond analog input

module. In order to exert control over the system, the PC104 utilizes an MPL PowerPC

controller Analog and Timing I/O Intelligence (PATI) module for generating a PWM

signal on each of the two MOSFET switches. The 5 V PWM signal goes through a

Semikron SKHI 21A IGBT/MOSFET driver, which produces a +15 V / -7 V gate drive

voltage with shoot-through protection, which is particularly helpful in this half-H switch topology. A picture showing the setup can be seen in Figure 16.
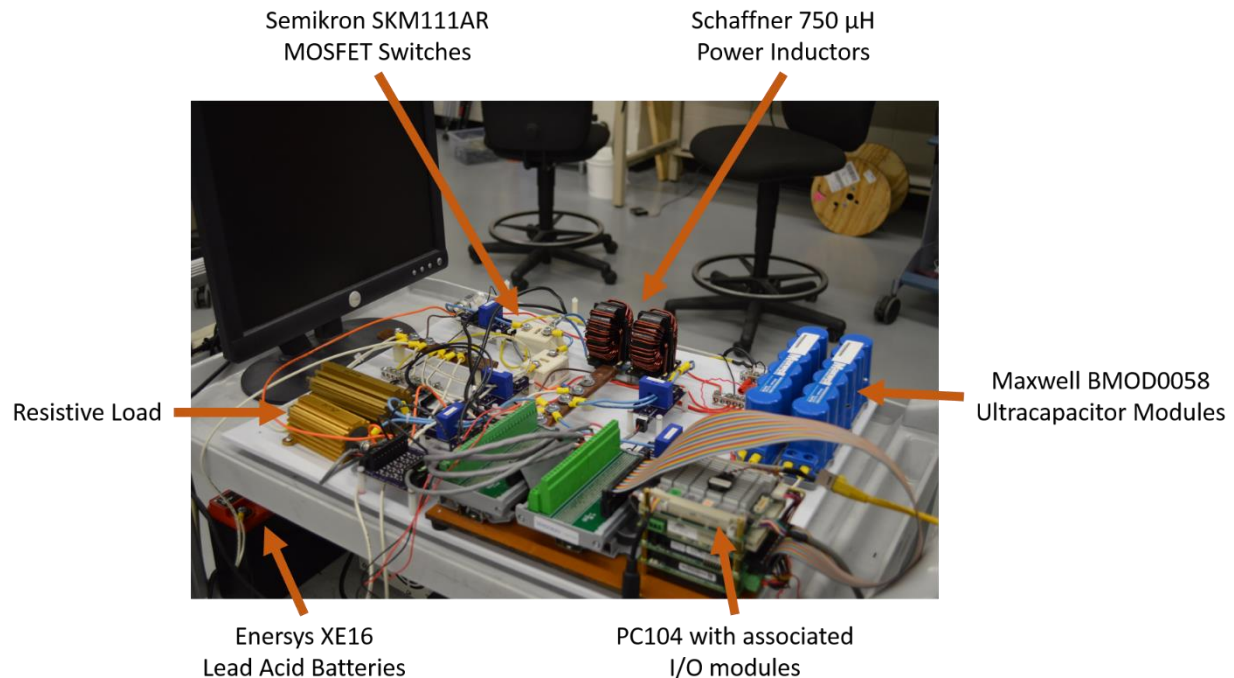

Figure 16: Photo of the tabletop setup

After constructing the tabletop, the controller for this system had to be designed. As mentioned before, the controller was a PC104 running Simulink RTOS with an analog input module and a PWM module. Simulink not only supports deploying simulations to the PC104, but also provides toolboxes for interfacing with the two modules attached to the unit. The controls implemented in this system include four PI controllers and a fuzzy logic controller. For both directions of power conversion, there are two PI controllers. The first PI controller is responsible for regulating the voltage output and produces an output that corresponds to a duty cycle between the ranges of 0-100%. The second PI controller is responsible for exerting current limit on the power conversion by pulling back the reference voltage as the current exceeds the limit. The Simulink block diagram

used in this experiment can be seen in Figure 17. Looking at the diagram, it is seen that

the PI controller outputs are either driven by the PI output or are held to a zero value

based on the sign of the value determined by the fuzzy logic controller. This is to ensure

that power only flows in one direction at a time and that the half-H switches never enter
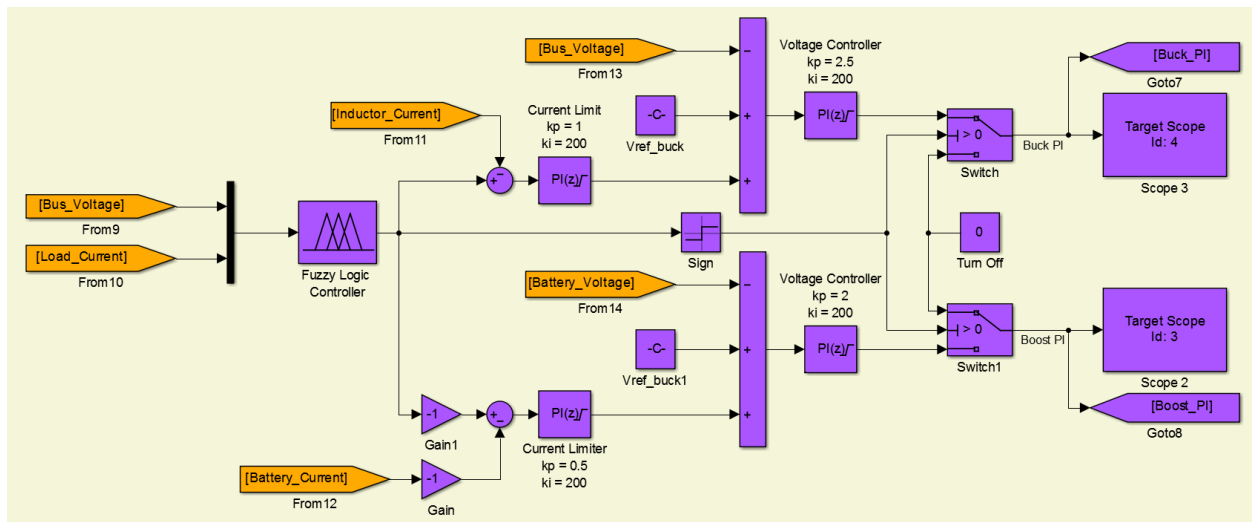
a shoot-through configuration.

Figure 17: Controller block diagram

The fuzzy logic controller was designed to mimic the simulation setup, but scale the

values to a region that is more appropriate for the hardware that was used in this case.

There was also some time spent on smoothing the response by changing the

membership functions from triangles to Gaussian curves. The fuzzy logic membership

functions can be seen in Figure 18, Figure 19, and Figure 20. The rule-base used in this

case is the same as used previously in the simulations, which can be referred to in

Table 1. The input to output relationship between the fuzzy membership functions can

be seen in the surface plot in Figure 21. To describe the fuzzy logic inputs and outputs,

they can be seen in Table 4. These linguistic values chosen in this controller along with

their ranges were chosen based on both expert experience with HESM topologies and

generalized system requirements. They can be tweaked after verification if it is

necessary to achieve a slightly different response, but these values should be capable

of producing the desired results.

Table 4: Fuzzy Logic Inputs and Outputs

Input/Output	Linguistic Value	Range
Input 1	"Very Low"	< ~5.7 V
Input 1	"Low"	~5.5 V – ~5.95 V
Input 1	"Good"	~5.7 V – ~6.3 V
Input 1	"High"	~6.05 V – ~6.5 V
Input 1	"Very High"	> ~6.35 V
Input 2	"High In"	< ~-8 A
Input 2	"Low In"	~-15 A – ~0 A
Input 2	"No Flow"	~-10 A – ~10 A
Input 2	"Low Out"	~0 A – ~15 A
Input 2	"High Out"	> ~9 A
Output	"High Recharge"	< ~-17 A
Output	"Low Recharge"	~-30 A – ~0 A
Output	"No Flow"	~-3 A – ~3 A
Output	"Low Discharge"	~0 A – ~14 A
Output	"High Discharge"	> ~7 A

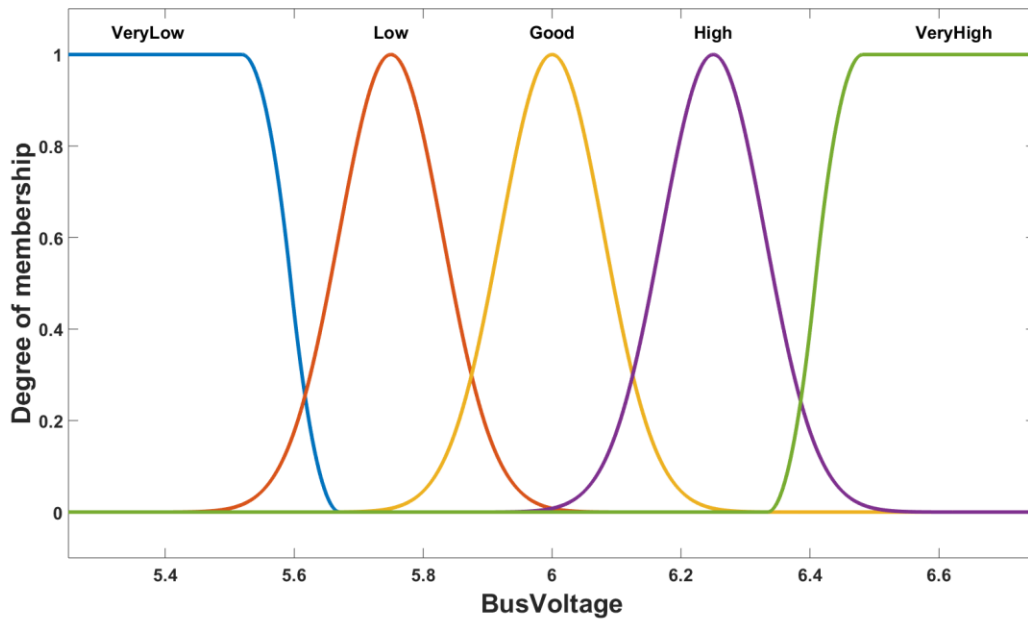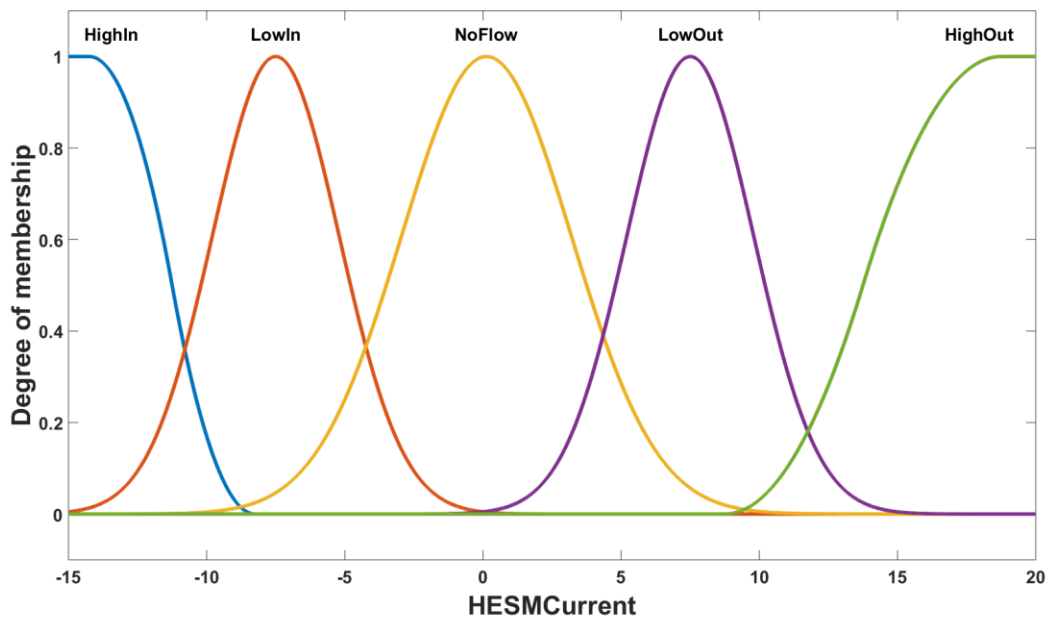Figure 18: First input fuzzy membership function

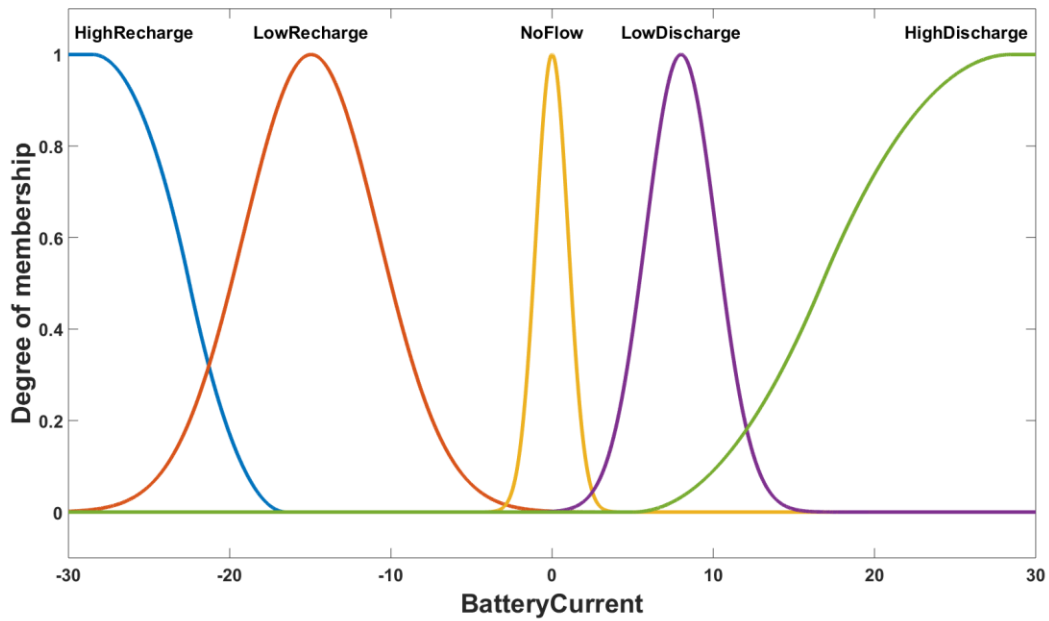Figure 19: Second input fuzzy membership function
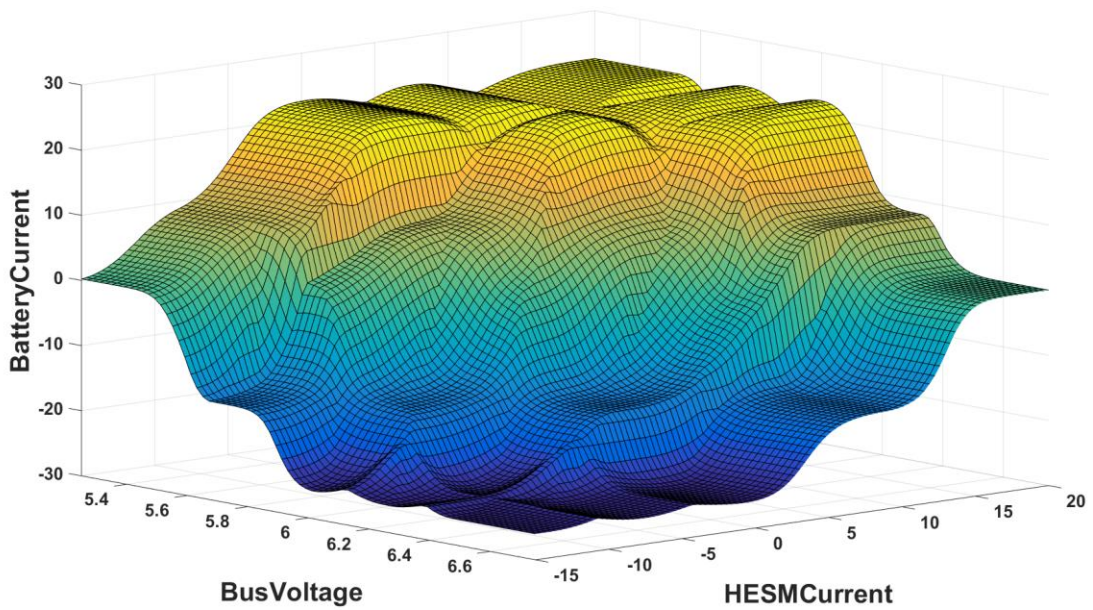
Figure 20: Output fuzzy membership function

Figure 21: Surface plot depicting the fuzzy logic control inputs vs the output

At this point it was necessary to define an electrical load profile that would emulate a

shipboard power architecture. One common load profile run in the naval community is

what is referred to as a "5 second – 1 second" load profile. This can be interpreted as having a high power load for 5 seconds followed by a low power load for 1 second. This pulse train is typically continued for the entirety of an experiment. With this – and the constant load with a programmable power supply – in mind, it was decided to run the following profile shown in Table 5. This profile utilizes two different settings through the test to validate the simulation results from before. The first half of the test utilizes a lower overall contribution from the programmable power supply to emulate a situation where the HESM is required to contribute to powering the load. The second half of the test utilizes a higher overall contribution from the programmable power supply to emulate a situation where there is an excess of power available from the load/generation component and there is power available to be used to recharge the HESM's batteries. This is a situation where a pulsed load may have dropped off for lack of need.

Table 5: Load Profile for HESM Tabletop Experiment

Period	Time	Value
First half of test		
High Power	5 seconds	-9 A
Low Power	1 second	21 A
Second half of test		
High Power	5 seconds	11 A
Low Power	1 second	21 A

The results from this experimental test can be seen in Figure 22 and Figure 23. Figure 22 shows a plot of the voltage vs time and Figure 23 shows a plot of current vs time. When comparing these results to the simulation results shown in the previous chapter it is clear that they both produce very similar outcomes.

One of the major differences is that there are larger spikes of voltage during the first half of the test on the real-world validation and less spikes of voltage during the second half of the test. This is opposite of the results achieved by the simulation results. This can be attributed to a slight difference in fuzzy logic tuning and can honestly be disregarded as a random error. Overall these results show that not only is fuzzy logic control a viable method for controlling this type of system, but that the simulation results very closely follow what would be seen in the real world as well. Although this custom testbed now offered a hardware implementation of the simulated results, the next step was to actually implement this with COTS equipment as this is the most similar to a real world application.
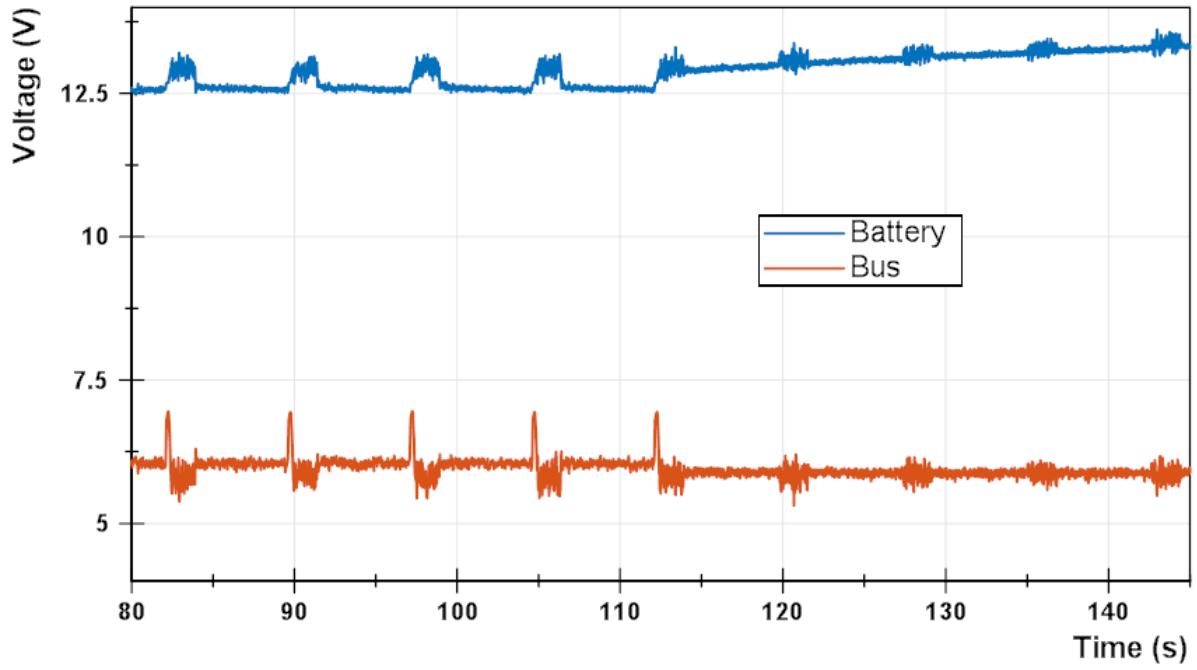
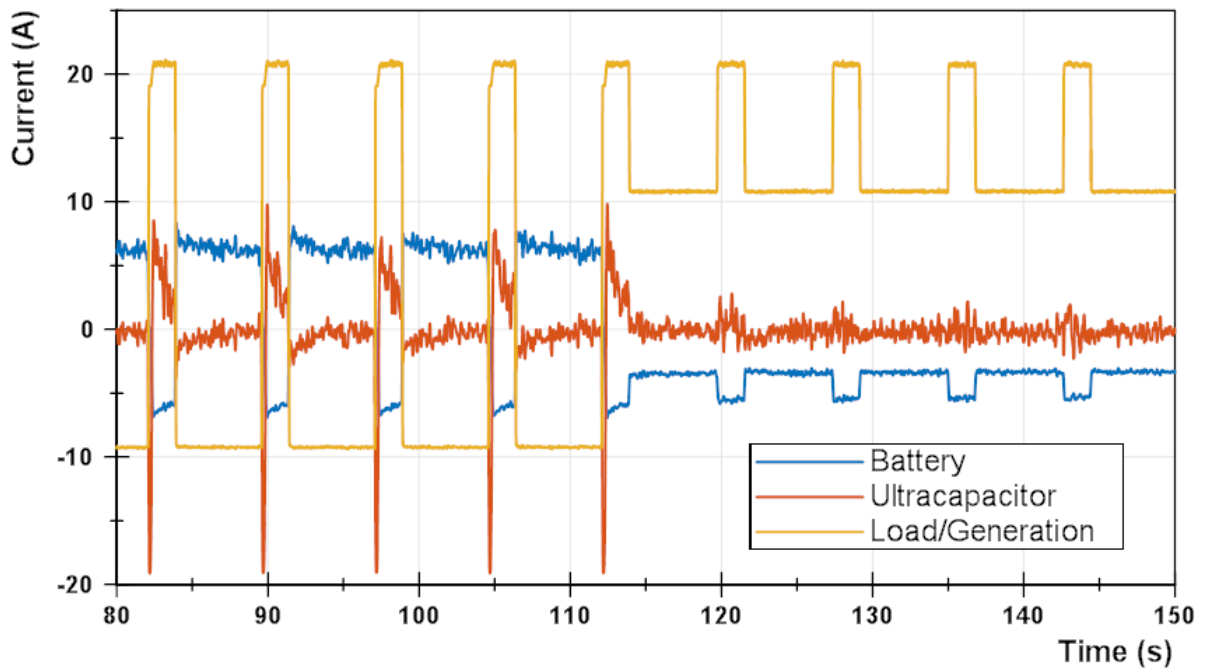Figure 22 : Voltage Waveform of HESM Tabletop Experiment

Figure 23: Current Waveforms of HESM Tabletop Experiment

Chapter 5: COTS HESM Experiments

In an ideal world, power systems would be individually designed from the ground up for each and every application that they are intended for, but in reality, many systems are comprised of an integration of previously designed components – referred to as commercial-off-the-shelf products. When designing a system that places emphasis on evaluating different control mechanisms, it is likely that the COTS components that are utilized would be chosen for their controllability being at the forefront of system needs. With this in mind, a COTS HESM was pieced together to observe the ability of these components to achieve similar results to a custom designed system while also allowing an investigation to proceed on the feasibility of different control mechanisms and to observe the strengths and weaknesses of COTS devices. Since system integration can be difficult and has many points of possible failure, a step-by-step approach was developed to get to a point to test the system level control of the COTS HESM while also validating the topology for usage in different scenarios.

DC Discharge Test

The first test run with COTS products was a simple validation test. Looking back at the previous work completed by Gao et al. [24], it was a good starting point to try to replicate the tests run with these small custom designed components with the larger scale COTS devices.

For safety reasons, it was decided that lead acid batteries should be used in the preliminary tests as the HESM was being constructed. In order to control the current out of the battery during this test, it was necessary to insert a DC/DC converter. In this test, a Zahn CH63250F-SS converter was used to step the nominally 48 V battery pack

down to 40 V [41]. These voltages were chosen arbitrarily just to determine if the COTS devices were capable of reproducing the results seen in [24]. The ultracapacitor used in this setup was a BMOD0083 P048 B01 83 F ultracapacitor, which is rated up to 48 V [42]. The load used in this test was a Chroma 63803 AC/DC Programmable Load, which is capable of sinking up to 35 A in a DC setting. Figure 24 shows this test setup topology.

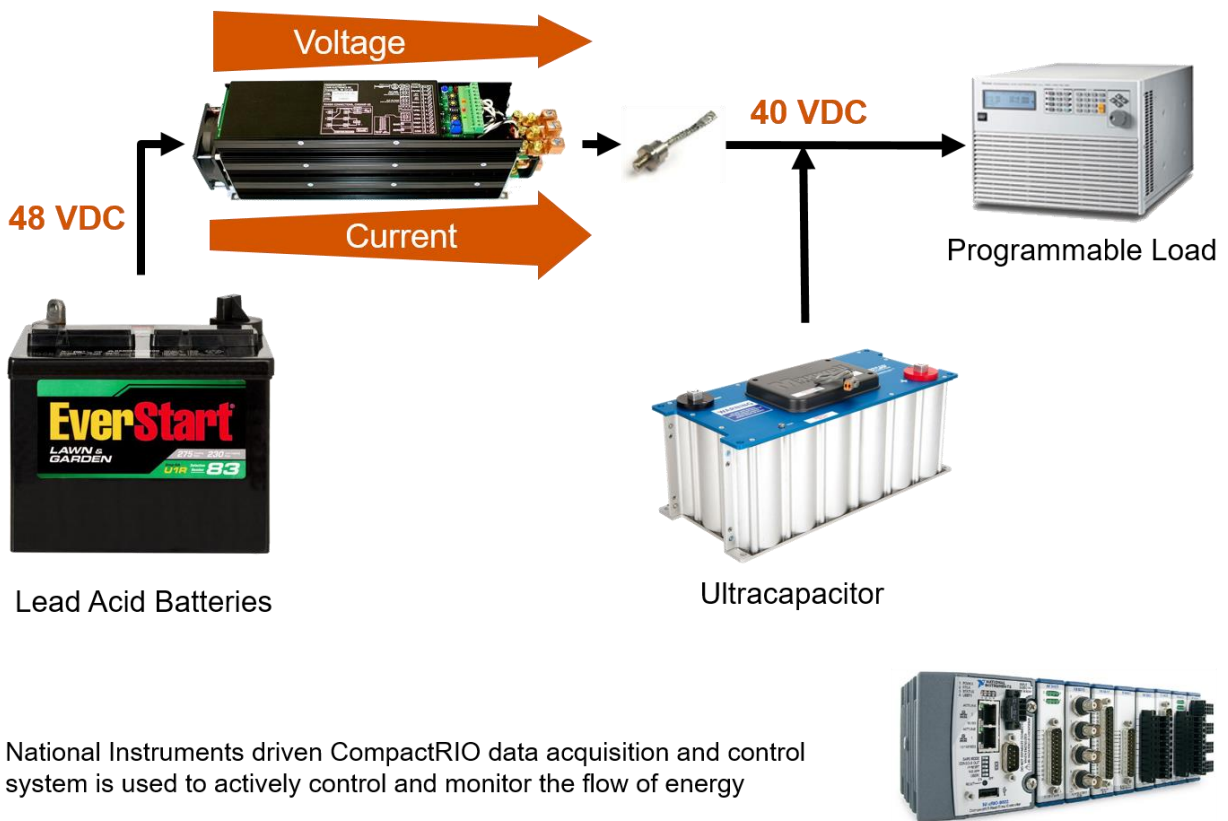Figure 24: Hardware topology for DC discharge test of COTS devices

The load profile run in this experiment was designed to mimic that of the profile being used in the experiment in [24]. In this experiment, it was necessary to slightly adjust the time period of the test, but the duty cycle was kept at 20%. This is not very indicative of a naval load but, again, this is just to ensure that the setup that was being used was

capable of reproducing similar results to previous work. A photograph of the
experimental setup can be seen in Figure 25.

- Ohmite POWR-RIB 1Ω *Resistor*
- Zahn CH15080F-SU *Boost Converter*
- International Rectifier 240UP120D *Diode*
- Everstart 12V Lead Acid *Batteries*
- ABB 5SNA 2400E170100 *IGBT Module*
- Maxwell BMOD0083 P048 B01 *Ultracapacitor Module*
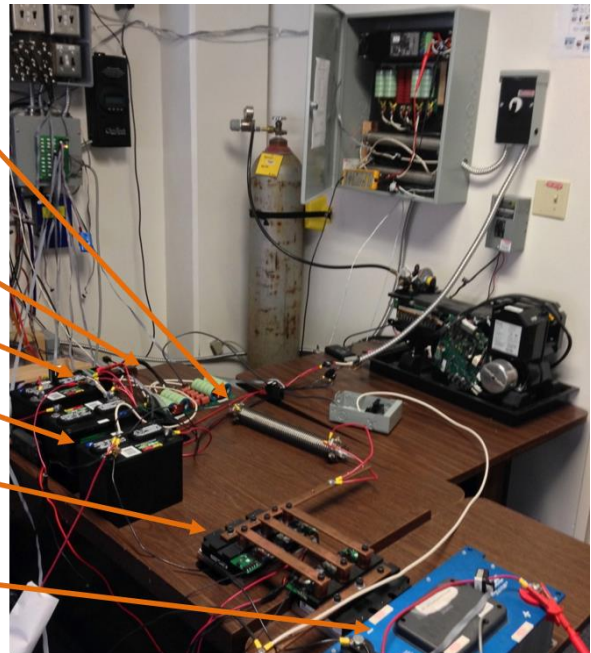
Figure 25: COTS discharge only experimental setup for reproducing results achieved by USC

Comparing the results from UTA's experiment in Figure 26 to the results achieved by
[24] in Figure 27, it is easy to see that the results follow a very similar trend. While the
exact numbers for the current are slightly different, the overall waveform is maintained.
In both tests, the battery maintains a relatively constant output current throughout the
test while the capacitor sources the bulk of the pulsed load during the pulsed load 'on'
time and slowly recharges during the pulsed load 'off' time.
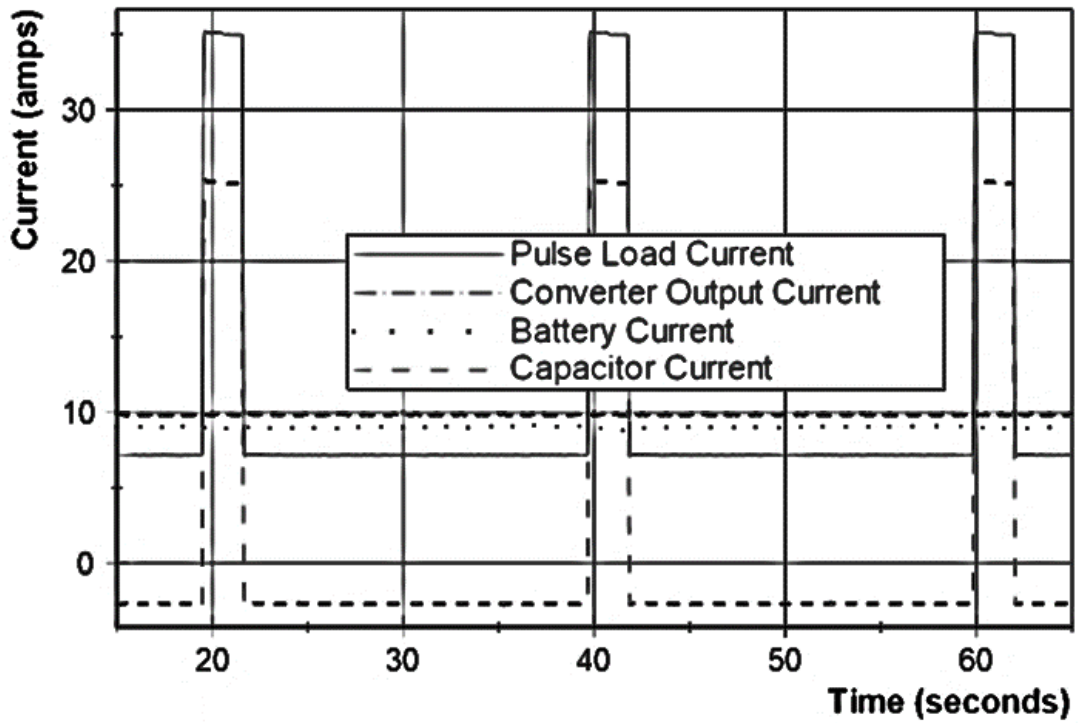
Figure 26: Results from UTA experiment
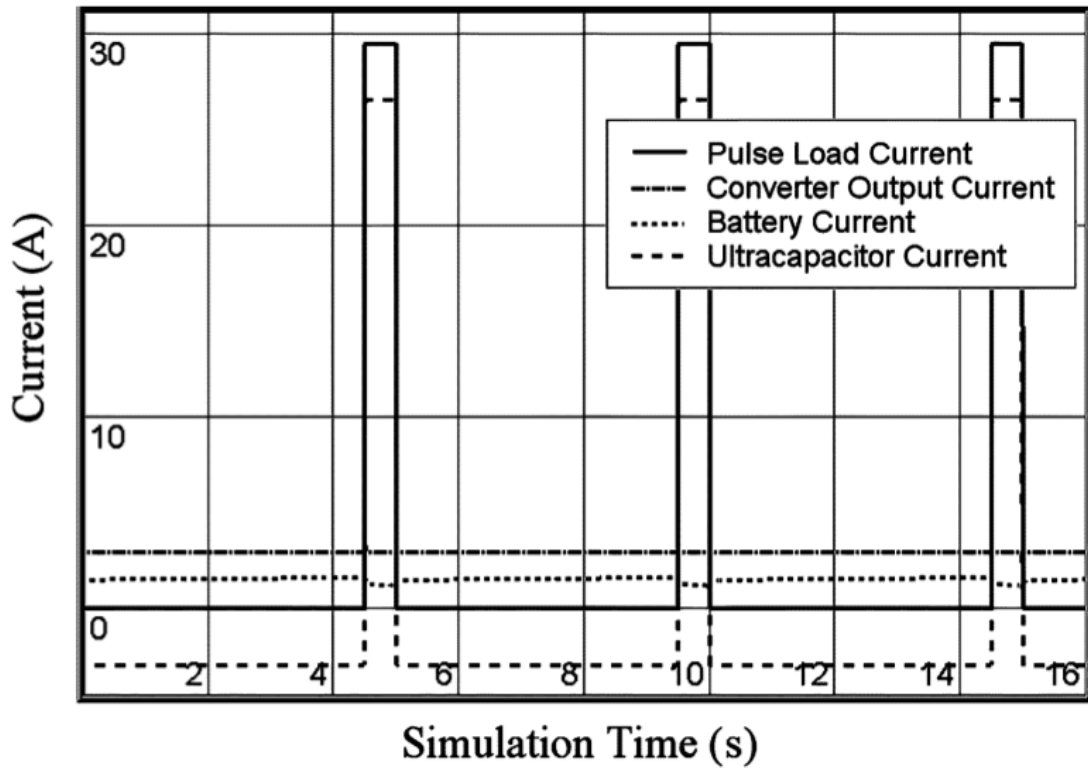
Figure 27: Results from USC experiment [24]

These results not only verify the work completed by [24], but they also show that COTS devices are capable of accomplishing the task just as effectively as the custom designed converter in their experiment. These COTS devices are particularly useful because they can be operated at a much higher power level than was previously shown in a laboratory setting. After verifying that these devices were capable of reproducing the results achieved by [24], it was time to shift the focus to a device that would be capable of bi-directional power flow to and from the main energy storage device, the battery.

DC Bi-Directional Test

The next objective for the COTS devices was to implement some form of bi-directional power flow as the ESD that they are intended to replace would need to both source and sink power to and from a power network in order to act as a competent power buffer. It is also necessary to add a recharge option as it doesn't make sense to simply discharge the batteries until they are empty and then start with new batteries.

This HESM used the previous test setup as a starting point, but built everything into a cart as the components increased. A photograph of the experimental setup can be seen in Figure 28 and the hardware topology can be seen in Figure 29. To describe the system in detail, moving from left to right, this setup uses only 3 lead-acid batteries connected in series to 36 V. The same buck converter used in the previous test was used to buck down the 36 V battery voltage to 26 V, but now requires a diode to prevent the back flow of current back into the battery when it is not desired. Above the buck

converter, two power converters can be seen. This is one of the first unique problems to utilizing a COTS system. While it was possible to design a single converter that is responsible for the bi-directional flow of power in the custom system, it wasn't possible to obtain a single unit with similar capabilities with COTS products. In this case, the manufacturer makes buck converters that allow current limiting, which is essential for the operation of this system, but they did not make boost converters with this option. To circumvent this issue, a boost converter was placed in series with a buck converter. The idea is to boost the voltage high and then buck it back down low to enable current limiting. The boost converter used here is a Zahn CH15080F-SU and the buck converter is a Zahn CH100105F-S. Under the power converters, there is the same 48 V Maxwell EDLC module, which still sits passively on the DC load bus. The power supply is installed to mimic a fossil fuel generator which may be installed in a Navy FOB or shipboard installation. These types of generators have an optimum operational condition at which they are most efficient. Therefore, it is best to operate them at this level and have them fluctuate as little as possible. This means that they should supply some constant base power to the load. The alternative sources, the batteries and EDLC in this case, should supply the excess transient and steady state power demanded by the load. In the event that the load is non-active, the energy storage should be used as an energy sink allowing the generator to continue operation at its most efficient level. This is of course beneficial to the energy storage as it gets recharged for future operation. In the setup here, a Sorensen DCS40-75E 40 VDC – 75 ADC power supply has been internally limited with voltage and current limits of 26 VDC and 25 ADC, respectively. These values are also dynamically adjustable using the NI control system.

The load was a major change from the previous test. On the load side is an IGBT-controlled resistor, the EDLC module, and a grid connected DC power supply. Initially, the load was an adjustable, 1 Ω, Ohmite Powr-RIB® resistor. In the work presented here, the resistance has been adjusted to ~0.4 Ω. Two 2400 A IGBT's, ABB model 5SNA2400E170100 [24], are used to connect the 'pulsed' resistive load to the DC bus. The three IGBTs of each module are connected in parallel and the two modules are connected in anti-series. Accounting for the small conduction voltage drop of ~2 V across the IGBTs, the resulting load requires roughly 60 A to be sourced to it when the bus voltage is maintained at 26 V. The IGBTs are controlled digitally by the NI control system using active high controls. Alternatively, a programmable load or DC/AC inverter can be connected in place of the IGBT-controlled resistor in order to evaluate different load types and profiles which possess more than two states. The resistive pulsed load was chosen initially due to its quicker and more consistent response times to trigger commands. Controlling this system is achieved by using a National Instruments CompactRIO. Using an analog output module, the voltage and currents of the system are dynamically changeable by the CompactRIO. One interesting aspect of this control is that it only affects the output of the power converters. In other words, during the discharge state, it is not possible to directly control the current coming out of the battery. Instead, it is only possible to limit the output of the converter which is related to the battery current with the equation,

$$V_{battery}I_{battery} = \eta V_{DC\ Bus}I_{Buck\ Converter} \qquad (\ 102\ )$$

where η is the efficiency of the power converter. This means that the CompactRIO must adjust its output to a level that achieves the desired battery current, which may change

throughout the test depending on either bus voltage, battery voltage and even changes in efficiency during operation.

- **National Instruments cRIO Controller**
- **Everstart 12 V Lead Acid Batteries**
- **Zahn CH100105F-S Buck Converter**
- **Zahn CH15080F-SU Boost Converter**
- **Zahn CH63125F-S Buck Converter**
- **International Rectifier 240UP120D Diode**
- **Ohmite POWR-RIB 1Ω Resistor**
- **ABB 5SNA 2400E170100 IGBT Module**
- **Maxwell BMOD0083 Ultracapacitor Module**
  On Back of Cart

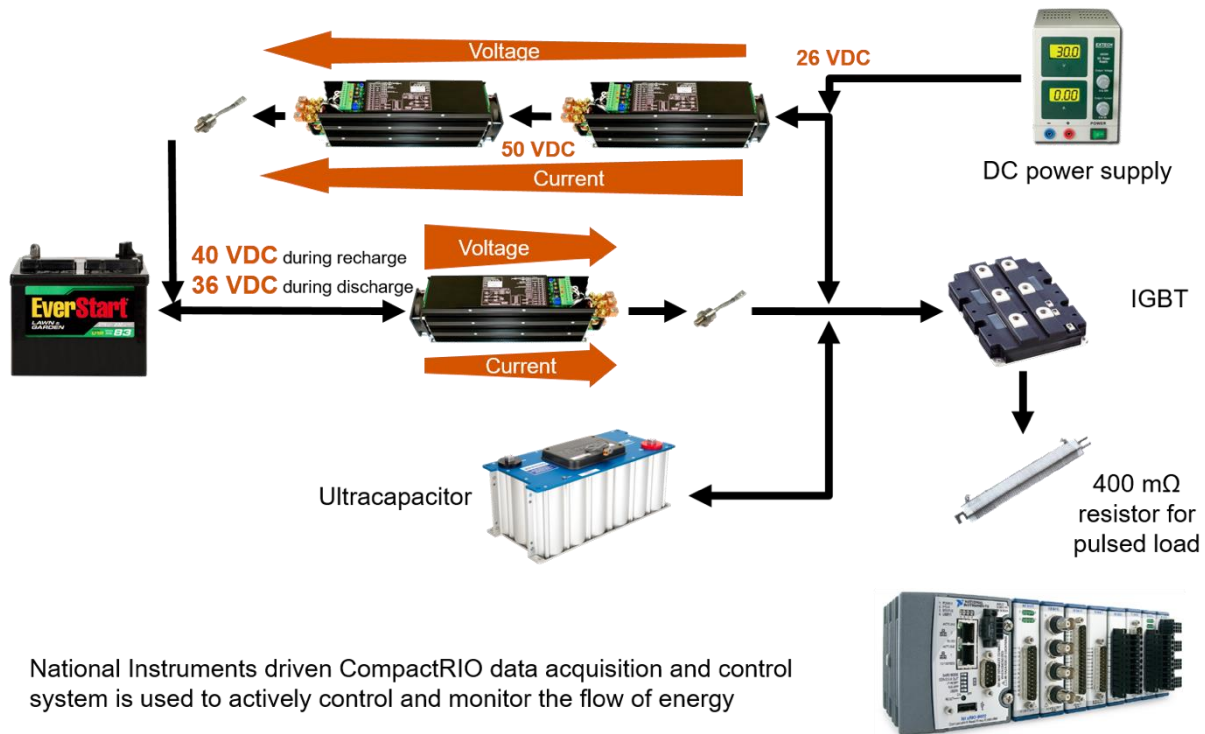Figure 28: Experimental setup of the bi-directional test of a COTS HESM [25]

Figure 29: Hardware topology for bi-directional DC test of COTS devices

The COTS power converters used also need to be controlled via an enable/disable control pin to impose a direction of current flow. When 0 VDC is fed from the control system to the enable pin of the converter, the converter operates. When 5 VDC is sent to the enable pin of the converter, its output is inhibited, but current is still allowed to flow backward towards the input of the converter, therefore a diode was placed on the output. The enable trigger pins operate on the order of ~5 ms.

In the current configuration, the EDLC is the only unregulated source in the HESM though this too could be easily controlled using additional voltage or current regulation to widen its usable voltage range. The EDLC used for the results presented here is a 48 V Maxwell BoostCap Module with a capacitance of 83 F and initial charge voltage of 26 V. The EDLC offers the ability to source high power to the load with nearly no impact to its life. Therefore when 60 A is demanded from the HESM, 20 A are supplied from the battery, 25 A are supplied by the power supply, and the rest comes from the EDLC. Initially, the EDLC supplies a higher front end power as the slower power electronic converters and DC power supply respond to the load.

In order to actively control the HESM components described above, a priority hierarchy for both active-load operation and inactive-load operation had to be implemented. The first priority during active-load operation is supplying the pulsed power load for which the HESM was implemented. This includes not only supplying the current required by the load, but also maintaining the bus voltage within the range of the system requirements. The second priority is to maintain the maximum efficiency of generator operation. In other words, the HESM should be able to compensate for the load demands in excess of the generator's optimal power output. In order to accomplish this,

the third priority must also be taken into account, which is to limit the current output of the battery to prevent excess loading. By sizing the HESM components and controlling the power flow, it is possible to augment the generator while fulfilling all of these priorities.

In this configuration, the EDLC is the dominant voltage source on the DC load bus, sourcing transients when the load exceeds the limits applied to the batteries or power supply. Since the batteries and the power supply have current limitations enforced upon them, their voltages can sag when the load demands more current than they are able to supply. The voltage of the EDLC is determined by the energy it has stored, therefore the DC bus voltage directly correlates with the amount of energy sourced by the EDLC which is described below.

$$\Delta E = \frac{1}{2} C \left(V_i^2 - V_f^2 \right) \tag{103}$$

Where ΔE is the EDLC's energy change in Joules, C is its capacitance in Farads, V_i is its initial voltage in Volts, and V_f is its final voltage again in Volts. The energy change is also the amount of energy needed to be returned to the EDLC during recharge to maintain its voltage the next pulsed loading. Rearranging the equation to calculate the voltage deviation, ΔV, of the bus yields equation 2:

$$\Delta V = V_i - \sqrt{V_i^2 - \frac{2\Delta E}{C}} \tag{104}$$

where $\Delta V = V_i - V_f$.

Knowing the acceptable variation in the DC bus prior to operation allows the user to properly regulate the battery and power supply currents.

It was decided to run a test similar to what was done in earlier experiments with the tabletop setup and the simulations. Since this is still at a verification of topology and integration stage, however, it is not necessary to change the system in the middle of the test before implementing the fuzzy logic controller that was designed in the previous tests. The load profile used in this test is described in Table 6.

Table 6: Load Profile for HESM Bi-Directional COTS Experiment

Period	Time	Value
First half of test		
High Power	5 seconds	400 mΩ
Low Power	1 second	Open Circuit

The overall test results can be seen in Figure 30. This displays plots of the system currents recorded during the ten experimental cycles. While it may initially appear that the nodal currents do not sum up to the pulsed load current, it should be noted that the battery current plotted is that measured into the buck DC/DC converter. This current was selected as it represents the current drawn from the batteries which is of higher importance than the current supplied out of the DC/DC converter. It is also worth noting that the power supply current never decreases. Even during the periods of inactivity, the capacitor is directly connected to the power supply thereby sinking current from it even when the load and recharge converters are disabled. Once the recharge converters are enabled, the current into the capacitor decreases as current is diverted into the batteries. Had the DC power supply been a fossil fuel generator, as it may be in a field application, this type of topology enables the generator to continue sourcing power at its peak efficiency while the energy storage devices are recharged. The high specific

power of the EDLC enables it to absorb high currents while limiting that supplied to the batteries to rates within their rated recharge values.
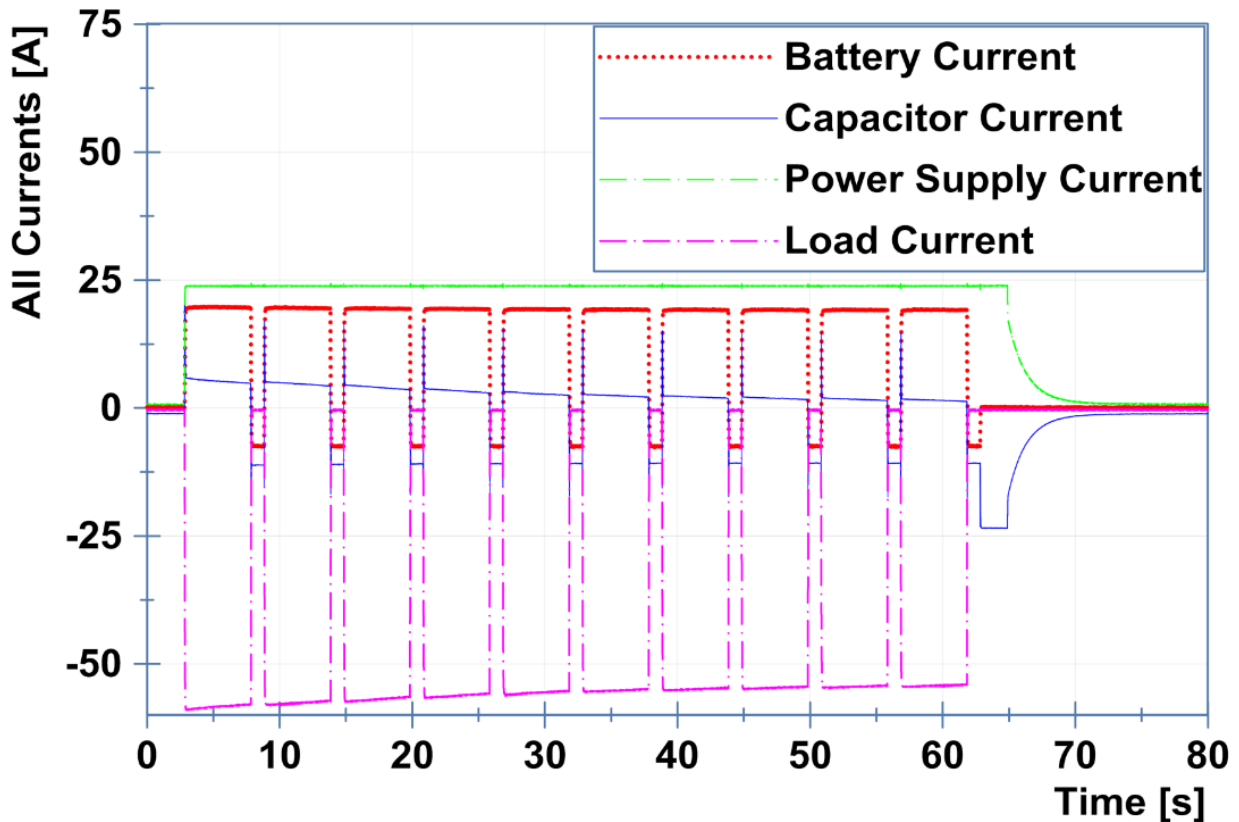

Figure 30: Overall current results from bi-directional test of a COTS HESM [25]

A detailed view of the power waveforms during a single 5 second discharge is shown in Figure 31. It can be seen that at the start of the pulsed loading, there is a spike in the current sourced by the EDLC whereas the batteries have a quick but gentle rise up to their full current sourcing level. This is exactly the desired result from this configuration. The high power density of the EDLC enables it to respond very quickly to a pulsed load. The buck converter and rate of reactions from the battery are a bit slower to respond. While the converters do respond within microseconds of receiving an enable/disable signal, the transition time of response to full power flow takes closer to 5 ms. The plots

show that an active HESM requires some time to charge internal control devices and filters when enabled and this delay should be accounted for in the pulsed power system deployment. Overall, this demonstrates the ability of the EDLC to peak shave the battery based energy storage as well as reduce the stress on the battery's internal chemistry.
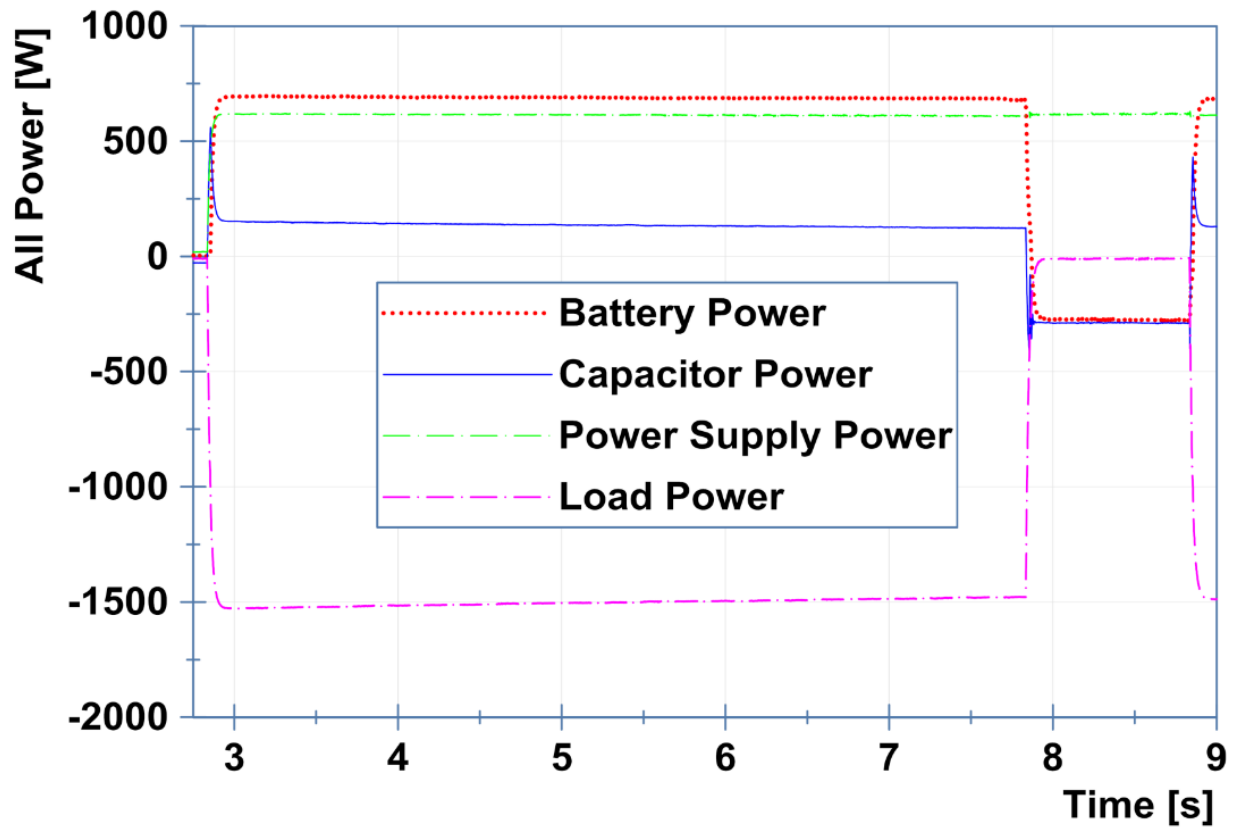
Figure 31: Single pulse power results from DC bi-directional test of a COTS HESM [25]

This configuration of a HESM topology shows that it is possible to both sink and source power to and from a battery using commercially available products with the ability to limit that specific amount of current in order to ideally preserve the lifetime of the batteries. These results are particularly promising as they showed no real issues with performance. The only concern of this entire test was the requirement of two power

converters on the recharge path of the batteries, but the results show that this addition had negligible effects on the system. At this point, it was decided that the next logical step for the COTS equipment was to verify the ability to perform in an AC setting as this energy storage device could possibly encounter scenarios where the DC power would be quickly inverted in order to send the power to other locations onboard the ship.

AC Tests

Moving to an AC setting could be more indicative of what would be encountered in a shipboard setting, although it is unclear whether the power from the generators would be combined with the HESM on a DC or AC bus. For the purposes of these experiments, an AC bus coupling point will be evaluated. This portion of the work aims to address the concern of whether the topology HESM can be injected into a shipboard setting and perform as intended using COTS technologies. This will also give insight into the effect the HESM has on the power quality of power generation when utilizing traditional fossil-fuel driven generators as would be typically seen aboard a naval vessel.

Using Figure 32 as a reference for the design, it is clear that the main changes on the system come in the form of the loading and the power generation. For the load, there was a shift to a Chroma 63803 AC programmable load with ratings of 3.6 kW / 36 A / 350 V, which is used to simulate the pulsed loads of interest. The AC load is controlled dynamically using the GPIB protocol. In the results presented later, a 5 sec 'on' / 1 sec 'off' profile is run in which the AC programmable load varies its resistance from 9.6 Ω to 1 kΩ. To convert the DC power of the HESM into AC, a 4 kW Schneider Electric Conext XW 4024 Inverter [43] is used. Its DC input voltage can vary from 20 – 32 VDC. One

feature heavily utilized is its 'generator support' feature that enables the system to draw power from the generator up to a pre-specified current limit before starting to demand power from the DC input. The generator is a 3000W Champion Power Equipment gasoline generator. This generator outputs power in the form of a 120 VAC / 60 Hz sinusoidal waveform. The frequency of the generator is dependent on the governor, which compensates for loading effects to get the frequency as close as possible to 60 Hz. While the inverter technically has the ability to direct power flow from the generator to the DC load bus, it takes a lengthy amount of time to switch between its charge and discharge modes of operation. This is because the inverter was designed for residential use and as such, changes in power flow tend to be made on the order of minutes rather than milliseconds. In order to overcome this limitation, Xantrex XHR 33 VDC – 33 ADC bench top power supplies are used to rectify the generator's AC power and put it on to the DC bus. The bench top DC power supplies are tied on to the DC load bus via an IGBT switch. While the pulsed load is inactive, during the 1 sec 'off' time, the IGBT is closed allowing the generator to remain base loaded as it puts power onto the DC load bus. Once connected to the DC bus, the power supplies supply a recharge current back to the batteries via the upper current path previously shown just to the right of the batteries. Moving from the previous test to an AC setting required no changes on the interactions between the batteries and the DC load bus, but the battery was swapped out for a lithium-ion battery pack. The batteries being used are K2 $LiFePO_4$ cells arranged in a 12 series / 6 parallel configuration. They are 2.6 Ahr cells that have a voltage range of 2.0 – 3.7 V [44]. By the transitive property, this means that the cells are configured into 15.6 Ahr module with a voltage range of 24 – 43.8 V.
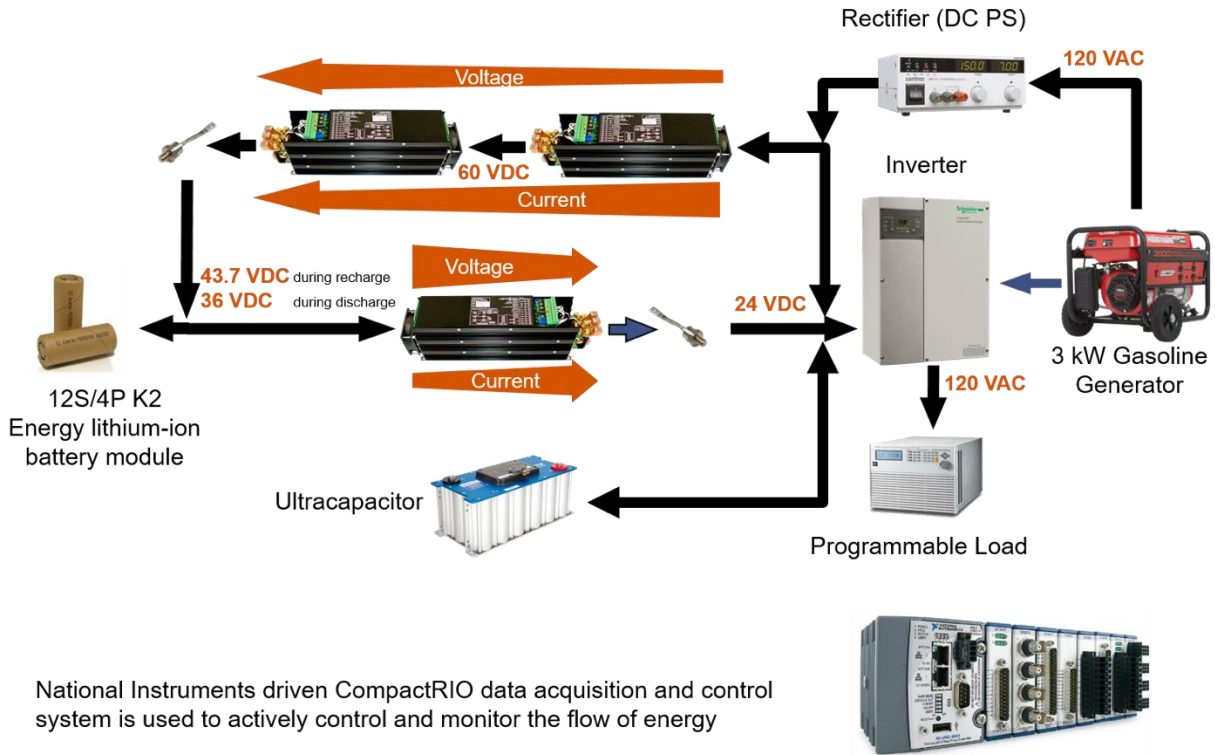
Figure 32: Hardware topology of the AC test of a COTS HESM [34]

At this point, it would be logical to think that the lithium-ion batteries might be suitable to serve as a power dense module to either the lead-acid batteries or just to operate as a standalone module, but in this scenario it is used as the energy dense device to keep the current limited and the lifetime high. A Maxwell BMOD EDLC module is placed across the DC load bus to serve as the power dense element capable of sourcing and supplying any high power transients [42]. The module has an 83 F capacitance and a voltage rating of up to 48 VDC. This was a module already owned by the lab and is not optimized due to the vast spread between its maximum voltage ratings and that of the DC bus. When used here, it typically remains within the range of 23 – 25 VDC.

This ultracapacitor has a maximum energy storage capability of

$$Energy = \frac{1}{2}CV^2 = \frac{1}{2}(83\ F)(48\ V)^2 = 47.81\ kJ \qquad (\ 105\ )$$

While Joules can be difficult to convert to Ahr on a capacitor due to its varying voltage during operation, it could be assumed that the average voltage is the middle point of the charged and discharged voltage, at 24 V.

$$Capacity = \frac{\frac{1}{2}CV^2_{charged}}{V_{average}} = \frac{\frac{1}{2}(83\ F)(48\ V)^2}{24\ V} = 1.11\ Ahr \qquad (\ 106\ )$$

Although this is a considerable amount of capacity when compared to a traditional capacitor, it is almost 15 times less energy than is stored in the lithium-ion battery pack. On the other hand, while the K2 power cells have been experimentally shown to last up to several hundred cycles during high rate cycling [19], the Maxwell Ultracapacitors are rated up to 1,000,000 cycles at high rate cycling [42]. For these reasons, the HESM uses the lithium-ion battery pack as the energy dense device and the ultracapacitor as the power dense device. As before, since the EDLC is the only device on the load bus without any current limitations placed on it, it dominates the voltage of the DC load bus. If the EDLC loses charge, it follows that the DC load bus loses voltage. Therefore, the purpose of the EDLC is to supply and absorb all transient currents without losing or gaining a large amount of charge which might put the system outside of voltage requirements dictated by the inverter.

Energy management is achieved using a National Instruments 9022 cRIO controller. The cRIO has analog inputs, which are used to measure the power flow and voltage points of the system in order to make a decision based on hierarchical importance. The

cRIOs are capable of altering the output voltages and current limits of the converters on the fly as necessary. The priority hierarchy is as follows:

1. The control system's highest priority is to maintain the charge voltage of the batteries and EDLC. If the system detects that the battery voltage drops below a preset value, it will shut down the HESM to protect the batteries. This is achieved by sending a disable signal to all of the converters and all switches are open circuited. If the EDLC module's voltage drops below 20 VDC, the inverter will no longer accept the DC load bus as a power input to the inverter. In an effort to get the HESM back into operation, energy is fed from the batteries into the capacitor until its voltage is restored.

2. The second highest priority of the control system is to deliver power to the load. Any time power is demanded from the load, the HESM is automatically transitioned from its current state into the discharge state so long as none of the safety conditions listed in in Priority 1 above are violated.

3. The control system makes any attempt possible to recharge the batteries and/or EDLC when power is available. This state of the system is only engaged when there is a power supply available, there is no load demand, and none of the safety conditions listed in in Priority 1 above are violated.
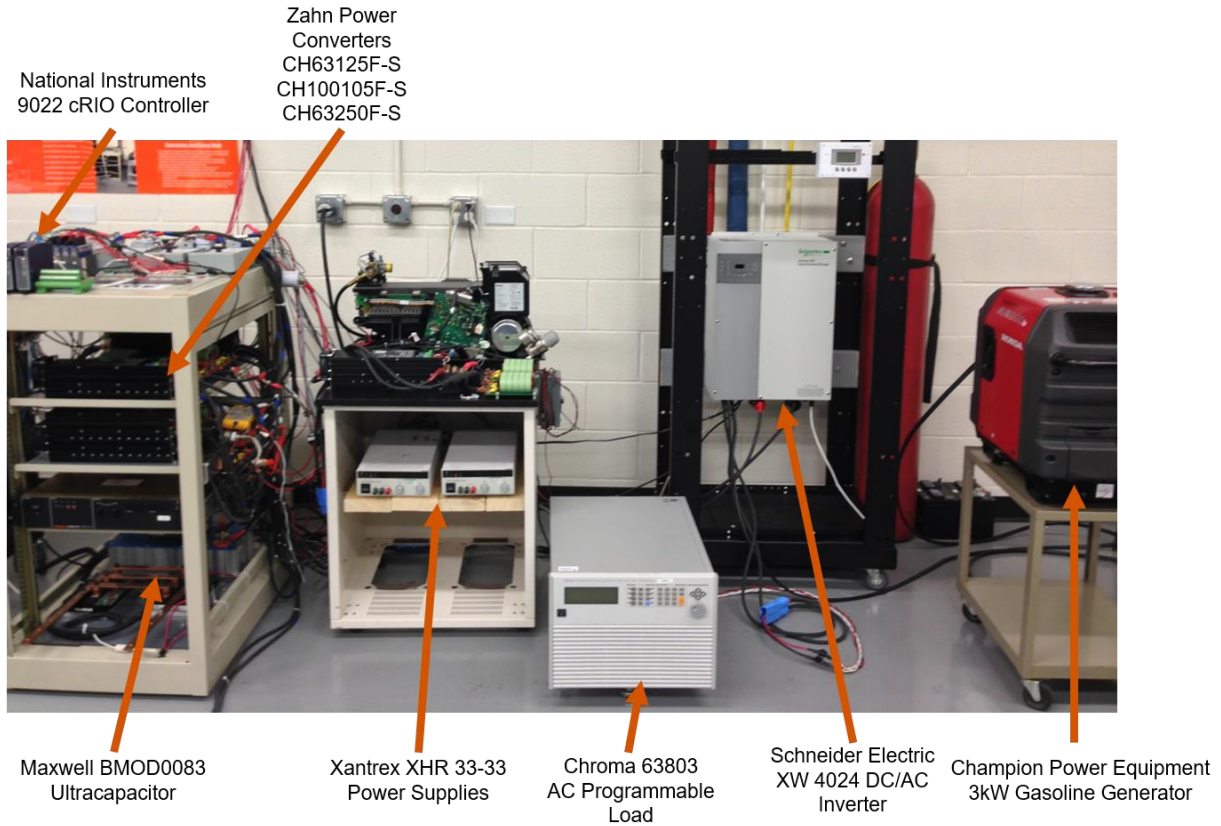
Figure 33: Experimental setup of the AC test of a COTS HESM [34]

The purpose of the experiments presented here is to demonstrate how a HESM may be utilized in combination with a mechanical fossil fuel electrical generator to drive a high power pulsed load. An load profile similar to the previous experiment was chosen and can be seen in Table 7.

Table 7: Load Profile for HESM AC COTS Experiment

Period	Time	Value
First half of test		
High Power	5 seconds	1500 W
Low Power	1 second	0 W

A few different scenarios will be explored in this report.

1. The first scenario utilizes the gasoline generator as the sole source in the system. This scenario is hard on the generator as it is repetitively loaded and unloaded.

2. In the second scenario, the generator is the sole power source, however instead of being unloaded during the 1 second 'off' period, the HESM is employed as a load to the generator keeping it base loaded as much as possible.

3. In the third scenario, the HESM and the generator simultaneously source power to the load in a shared configuration and the HESM still sinks power from the generator during the 'off' period in order to maintain the base loading of the generator. This scenario ensures that the HESM is always able to accept charge but if not properly configured, the HESM will source more capacity than it sinks meaning that it will be depleted in the long run.

The intent is that these two latter scenarios will have a positive impact on the power quality as opposed to that observed in the first scenario. Though not shown here, additional scenarios are possible with a few being that the HESM is used alone to source the load without a generator present or the HESM is used similar to the way it is used in any of the scenarios listed but takes over the load only when a generator is unavailable. The power quality delivered to the load, with regard to the frequency and RMS voltage, will be presented.

Generator Only Test

The power flow of the system during the generator only experiment is seen in Figure 34. In the plot, positive power implies that the source is supplying power while negative power implies it is sinking power. The corresponding Fourier transform of the power delivered to the load can be seen in Figure 35 and a plot of the RMS voltage delivered to the load can be seen in Figure 36.
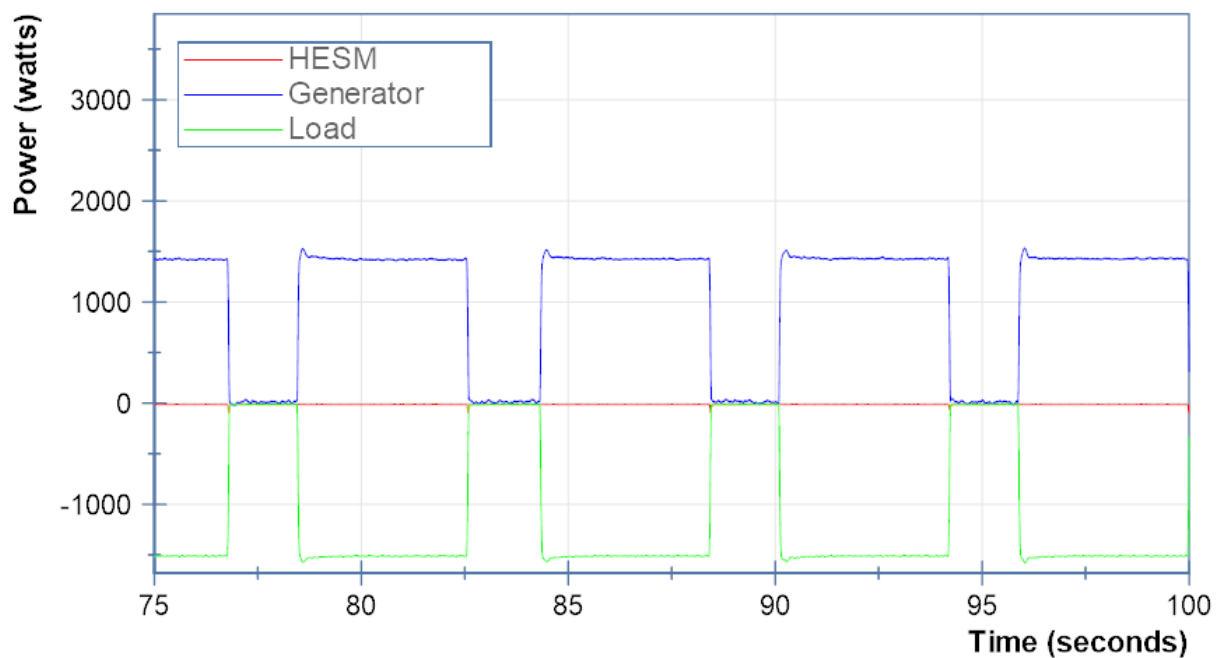

Figure 34: System power flow when only the generator is used to supply the load [34]

In Figure 34, it is clear that the HESM neither contributes nor accepts any power as the generator handles the entire responsibility of powering the load. In Figure 35, it is shown that two major frequencies are present during operation. Note that harmonics are also measured, especially the third harmonic, however the focus will be placed on the shift in fundamental frequency. The first dominant frequency is around 60.5 Hz and this is the loading frequency. The unloaded frequency is around 62.5 Hz showing how the

transient nature of operation negatively affects the rotational speed of the generator. The high frequency is observed less often simply because of the amount of time the generator spends unloaded as opposed to the amount of time it spends loaded. For comparison to standards, lines are drawn to show the constraints outlined in MIL-STD 1399 [45]. In Figure 36, the RMS voltage is shown along with the limits with which the system must stay within in order to meet MIL-STD-1399. The system easily meets these requirements with the only notable characteristics being the spikes of voltage when there is a change in loading and the average voltage deviation during these periods. During the 'on' period, the average voltage is around 120 V RMS while during the 'off' period, the average voltage is around 122.6 V RMS. This is a 2.6 V RMS difference between these periods.
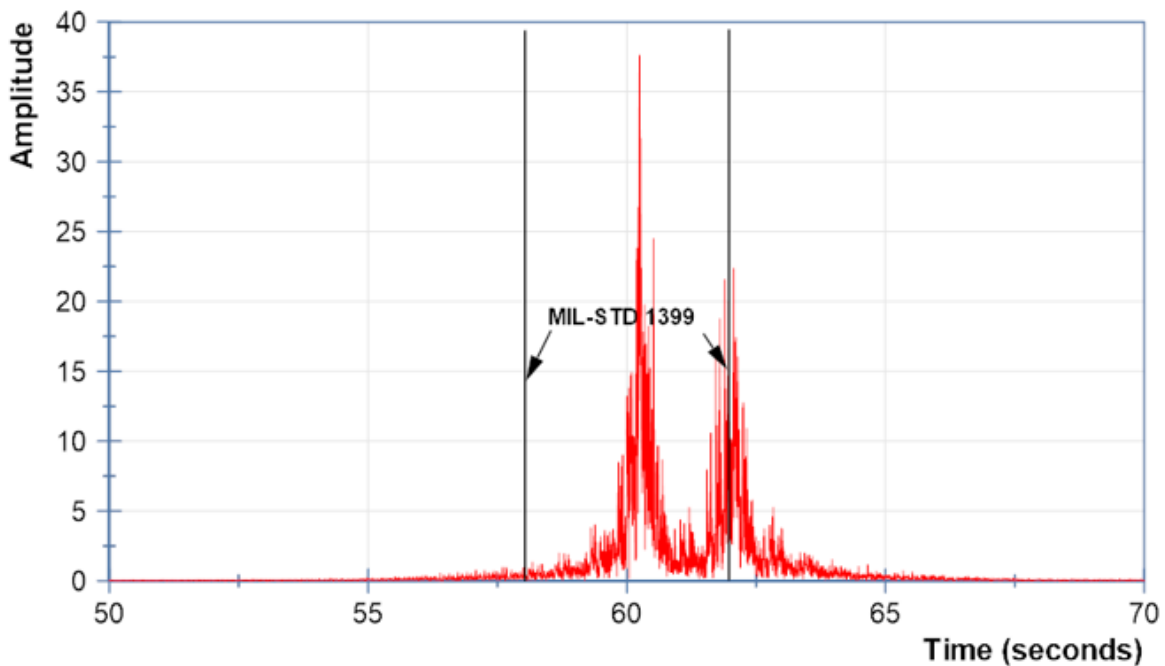

Figure 35: Fourier transform of power delivered to the load when only the generator is used to supply the load [34]
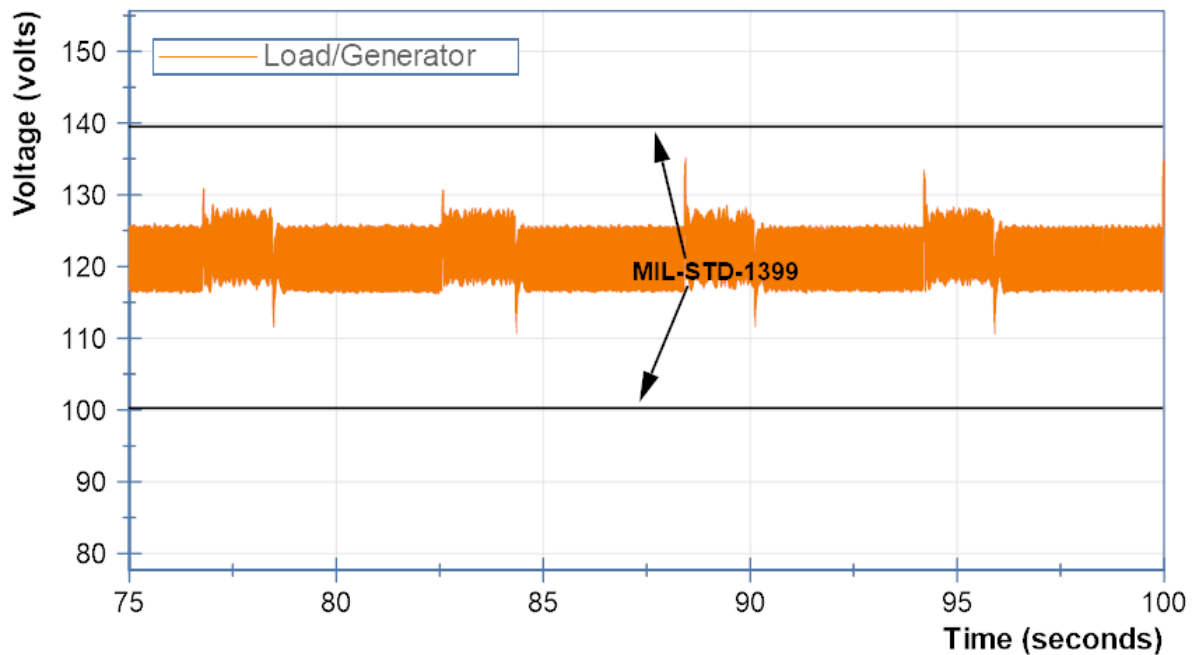
81

Figure 36: RMS load voltage when only the generator is used to supply the load [34]

Generator with Recharge Test

The power flow of the system during the second scenario experiment is seen in Figure 37. The corresponding Fourier transform of the power delivered to the load can be seen in Figure 38 and the RMS voltage delivered to the load can be seen in Figure 39. Figure 37 shows how the generator sources the entire load during the 'on' period as well as the HESM during the 'off' period. Note how there is a small amount of time between transitions where the HESM switches states in reaction to the change in the load. Also notice that despite the desire to base load the generator during the 1 second 'off' periods, this is not the case. This occurs for a couple of reasons. First, the current into the batteries must be limited to 30 A corresponding to a 2C rating. This requires that the buck converter output 1311 W, 43.7 V and 30 A.
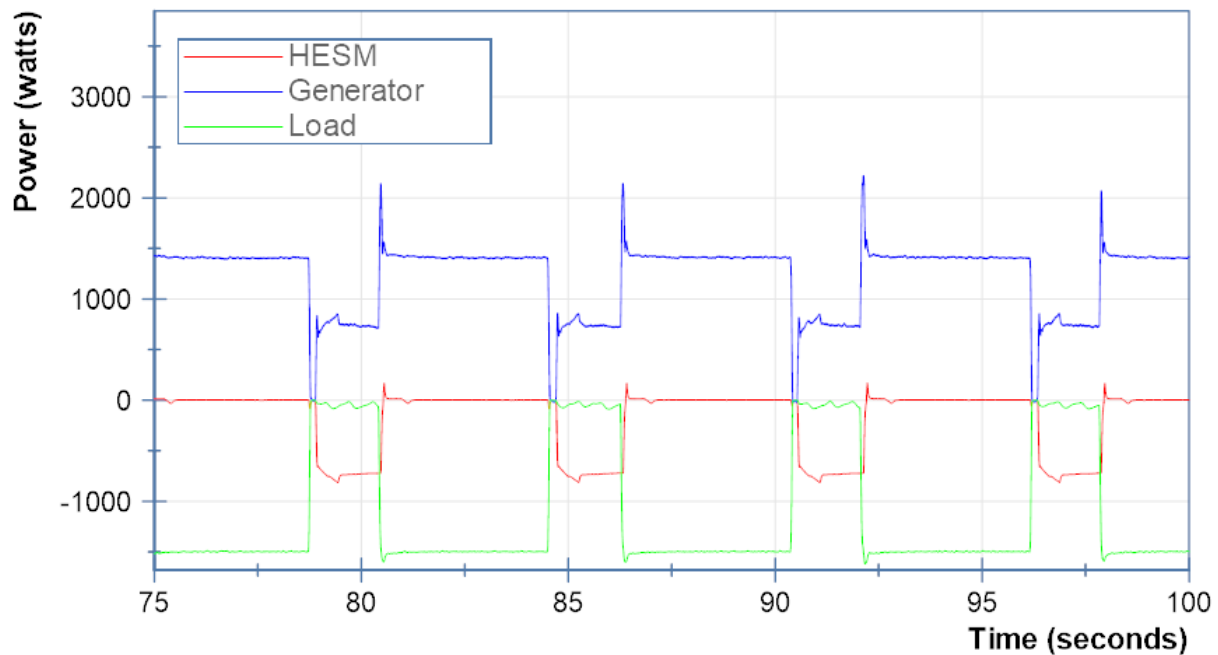
Figure 37: System power flow when only the generator is used to supply the load and the HESM loads the generator during recharge [34]

The bench top power supplies are rated at 1 kW each making them ideally capable of meeting the demand however their response is much slower than is needed to accommodate the 1 second loading period. If they are fully loaded, the output current quickly reaches 15 A, which is roughly half of their rated output current, however the output slowly ramps up to the peak current over a duration of roughly a few seconds. This means that the generator's output is quickly reduced and then ramps up along with them preventing its output from remaining as constant as desired. Before they reach the demand required from them, the 'off' period has concluded and the HESM transitions back into the sourcing state. In these tests, the power supplies were limited to 15 A so that their output remained constant during the 1 second period therefore the generator is also constant but less than that sourced by it to the load preventing it from being

equally loaded throughout the experiment. While the load power could have been reduced to better demonstrate capability here, the experiment is presented as is to show some of the tradeoffs that must be considered when designing such a system. In the future, the power supplies will be replaced with a faster rectifier and the current will be controlled using the recharge buck converter already in place. Another consequence of the inability to base load the system is that the EDLC actually supplies the remaining charge current to the batteries. This reduces their voltage prior to the next 5 second 'on' period which is undesirable. One proposed fix is to actively control the capacitor using additional power electronics and this is also planned in future work.

Comparing Figure 38 to Figure 35, it is clear that the frequencies start to shift closer to 60.5 Hz however there are still times where the frequency is closer to 62.5 Hz. This shift closer to 60.5 Hz is due to the HESM's ability to more evenly balance the base loading of the generator. As improvements are made to the system, it is expected that the generator can be better base loaded and all frequencies away from the load frequency can be reduced if not nearly eliminated. At first glance, it appears that the RMS voltages in Figure 39 are identical to those in Figure 35. However, upon closer inspection it becomes obvious that while there are still transient spikes during the transition phases, the average voltages converge slightly. During the 'on' period, the average voltage is around 121.5 V RMS while during the 'off' period, the average voltage is around 122.3 V RMS. This is only a 0.8 V RMS difference, as opposed to the 2.6 V RMS difference measured during the generator only experiment. As it did earlier, the RMS voltage always stays within the constraints of MIL-STD-1399.
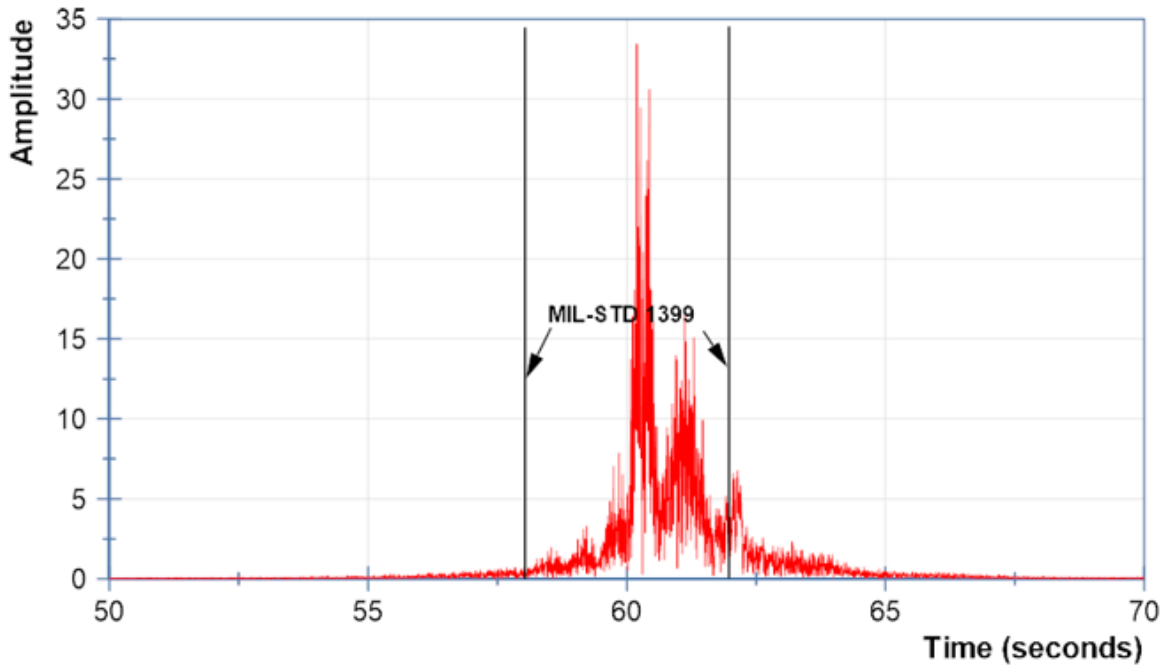
Figure 38: Fourier transform of power delivered to the load when only the generator is used to supply the load and the HESM loads the generator during recharge [34]
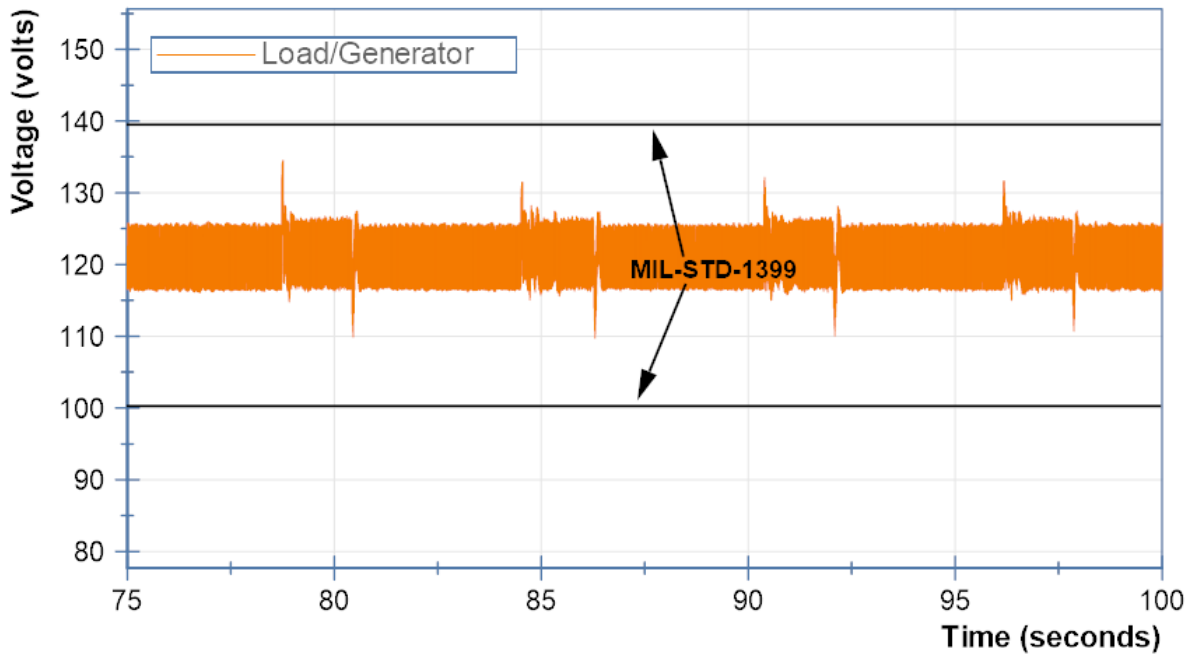

Figure 39: RMS load voltage when only the generator is used to supply the load and the HESM loads the generator during recharge [34]

Generator and HESM Parallel Test

The final experiment presented here is one in which the generator and the HESM are simultaneously used to source power to the load and the HESM is used to absorb energy from the generator during the load's 1 second periods of inactivity. The flow of power from each source during the experiment is plotted in Figure 40. The corresponding Fourier transform of the power delivered to the load is seen in Figure 41 and the RMS voltage delivered to the load is seen in Figure 42.
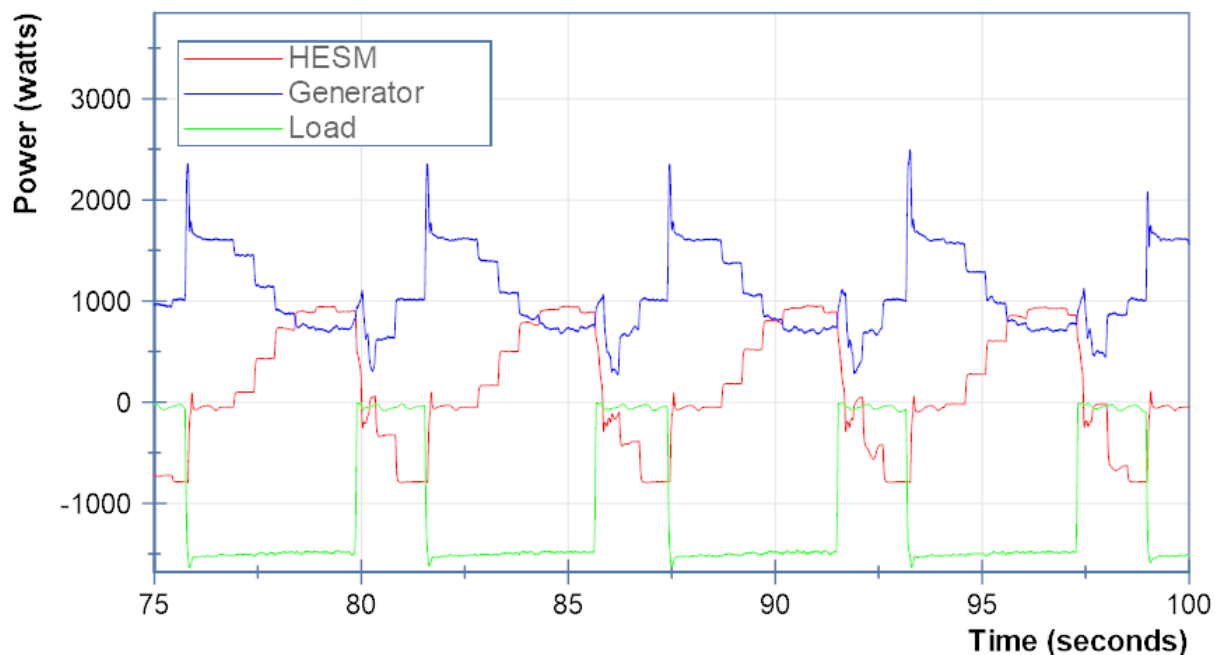

Figure 40: System power flow when the generator and HESM are simultaneously used to supply the load and the HESM loads the generator during recharge [34]

In parallel operation, the Xantrex inverter's 'generator support' function is used to limit the power flow from the generator and simultaneously source power from the inverter's DC input source. This is achieved by setting a limit on the RMS current that the inverter draws from the generator. If the RMS current limit is exceeded, the inverter kicks in and augments the generator with power from the DC source. Whenever the inverter's load

transitions from an 'off' state to an 'on' state, the inverter immediately sources all of the load's demand by passing through power from the generator. Unfortunately, as it does this the inverter does not quickly limit power from the generator meaning that if the load immediately demands power in excess of the 'generator support' limit, the generator will be stressed beyond the desired limits. Once the inverter detects that the 'generator support' limit has been exceeded, it takes the inverter just over two seconds before it fully limits the generator and augments it with power from the battery. While this is acceptable in most steady state applications, it is not optimal when pulsed loads are being operated. In the experiments presented here, roughly half of the pulsed load 'on' time has passed before the generator is limited and the batteries start to source power to the load. This type of operation is seen in Figure 40 where the generator's output power quickly spikes up and then ramps down in just over two seconds while the HESM slowly ramps up. Eventually both sources supply equal amounts of power, however it is much later than is needed to maintain a stable base load on the generator. The opposite is also true in that once the load turns off and DC power is no longer needed, it takes the inverter some time to recognize this and stop drawing power from the DC input. These are all consequences of using COTS components within the HESM design rather than those which are custom designed.

Figure 41 shows that the frequencies are closer to 60 Hz, similar to the 'Generator with Recharge' test. The spikes previously seen around 60.5 Hz and 62.5 Hz are still present but there is a clear shift towards 60 Hz. These results aren't completely representative of what this setup is capable of providing if the inverter response is faster, but they are still better than the results from the 'Generator Only' test.
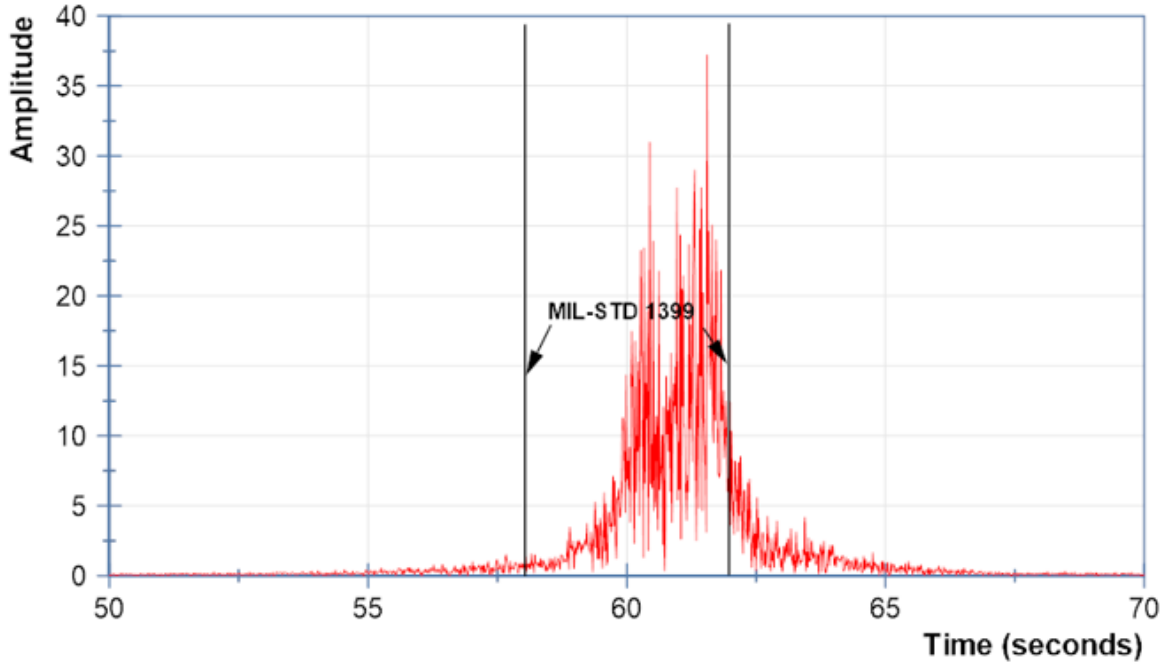
Figure 41: Fourier transform of power delivered to the load when the generator and HESM are simultaneously used to supply the load and the HESM loads the generator during recharge [34]
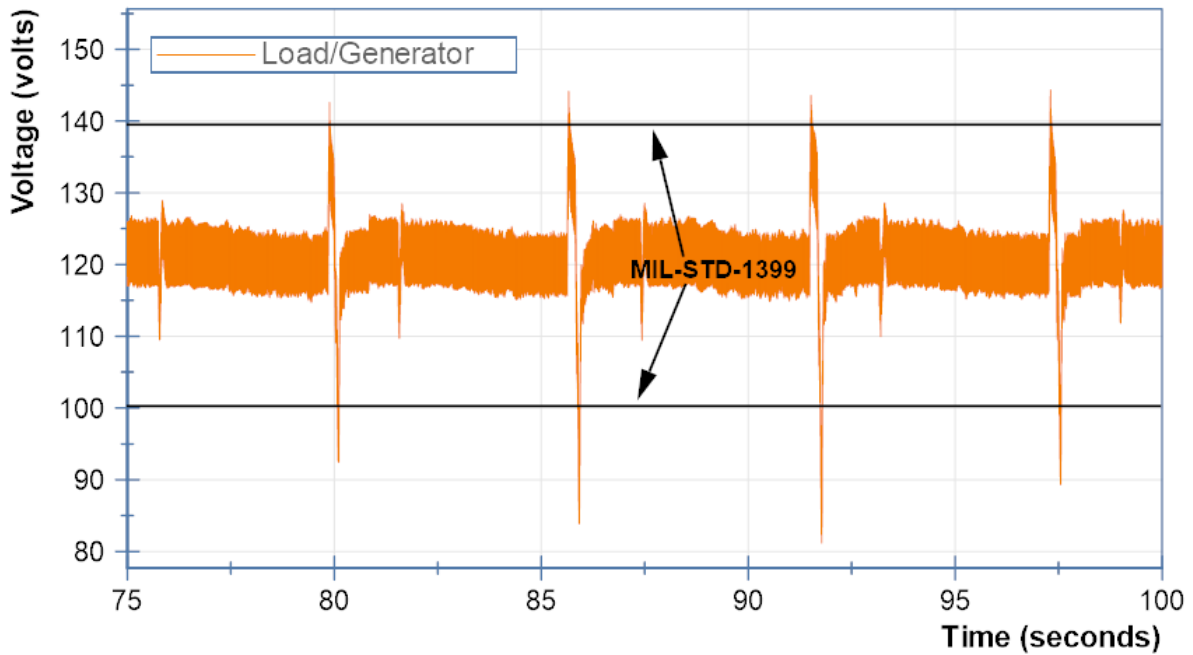

Figure 42: RMS load voltage when the generator and HESM are simultaneously used to supply the load and the HESM loads the generator during recharge [34]

As seen in Figure 42, there is a glaring difference in the RMS voltage waveform with presence of enormous voltage spikes and sags during transition when the load transitions from an 'on' state to an 'off' state. The sags are due to the overloading of the generator while it must source both the load and the HESM. The spikes are due to the abrupt open circuit after removing both of these loads. It is important to note that these voltage spikes and sags bring the system outside of the standards set by MIL-STD-1399.

The work presented here provides a brief glimpse into the design of a HESM and shows a few of the operational scenarios in which it will be utilized in the Navy's future electric fleet. The experiments showed how the operation of pulsed loads using a mechanical generator alone imparts high stress on the generator and results in poor power quality. They have also shown how a generator can be better base loaded if a HESM is used as the generator's load during periods of load inactivity. Similarly, it has been shown how a HESM can be used to augment a generator to supply the load while maintaining a base load on the generator. The latter set of results presented did not fully achieve the desired results and give a false impression that a HESM actually negatively impacts power quality. This is purely a result of two drawbacks introduced to the UTA system through the use of COTS components. This problem can be overcome by simply avoiding COTS software for integrating AC power sources and by rectifying the power from the generator to join the two power sources together in a DC setting before inverting them back to AC for transferring to another part of the ship. Now that the topology of the HESM using COTS equipment has been verified, the final logical step in this work is to analyze the ability of the fuzzy logic controller to impose a system level

control over the COTS equipment, solidifying the proposed hypothesis that it is a viable solution to this application.

Fuzzy Logic Control of COTS Equipment Test

The final experiment presented here is one in which the entire work presented here has built up to. It is easy to say that a system or a controller will work by designing and simulating the results, but it may prove to be much more difficult to implement when using real world products with their own internal control systems and dynamics to account for. In a final effort to validate the candidacy of a fuzzy logic control for implementing system level control over a Hybrid Energy Storage Module, it was decided to utilize the controller on the COTS HESM.

The system was completely physically overhauled in order to clean up the wiring, place the newer National Instruments 9118 CompactRIO Controller, and remove unnecessary components such as pull-boxes and extra Anderson Connectors. Photos of the new setup can be seen in Figure 43, Figure 44, and Figure 45. Figure 43 shows the overall COTS HESM System. Starting from the left and moving to the right, the HESM utilizes a PC with a fiber optic connection through the PCI-E slot to a National Instruments PXI-e 1078 chassis with NI PXI-e 6361 analog input modules for data acquisition. These modules are capable of up to 2 GHz sample rates, but in these tests they will only be used to sample at rates of about 1 KHz. The connections to these modules are attached to the side of the PC cart as BNC connectors. To the right and front of the PC is the energy storage cart. On the left of the cart are the battery packs in a blue shrink wrap. This is the same K2 lithium-ion 12s/6p battery pack used in previous tests.
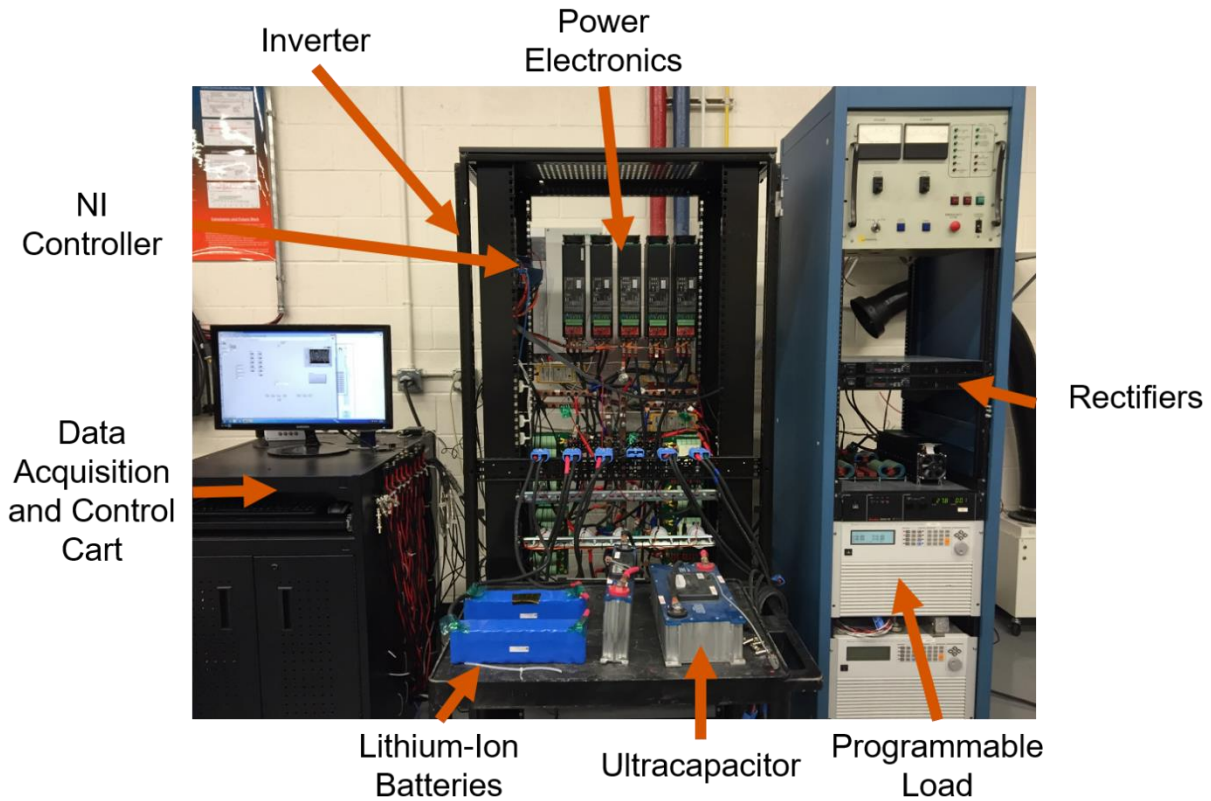
Figure 43: Photo of Overall COTS HESM System

The next device is the 500 F 16 V Ultracapacitor. This is not used in this test. The final

device is an 83 F 48 V Ultracapacitor which is the capacitor that sits on the 24 V DC

Load Bus in this test. Behind the energy storage cart is the actual HESM and can be

better seen in a close-up photo in Figure 44. On the top left of the photo, the National

Instruments 9118 CompactRIO Controller can be seen connected largely to the terminal

blocks below it. This can be seen much better in the close-up photo in Figure 45. To the

right of the controller, 5 separate black boxes can be seen which contain the switches

for the DC/DC power converters. These boxes connect to the green PCBs seen below

which are the LC filters for their respective power converters. Between the copper bus

bars, several yellow differential probes can be seen which are responsible for dividing

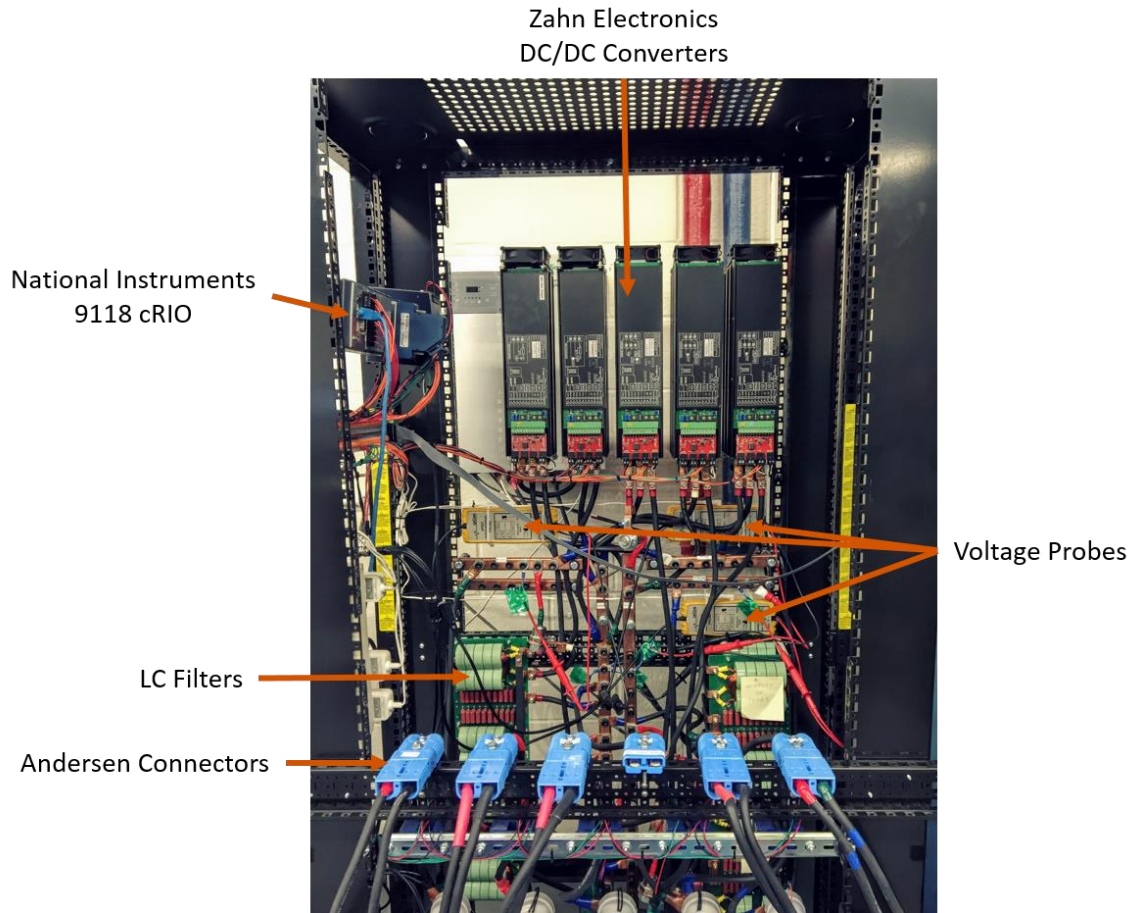down the voltage of the busses for the data acquisition system.

Figure 44: Close-up photo of the HESM

At the bottom of the photo, several components can be seen. There are blue Anderson

Connectors which are used for connecting the energy storage devices, the inverter, and

the power supply to the HESM cart. Additionally, there are blue Automation Direct hall-

effect current sensors which return voltages between +/- 10 V proportional to the

amount of DC current flowing through the wires. Finally, there are grey DC contact

relays responsible for providing not only a controllable way to insert items to their

respective busses, but also as a quick emergency shutdown of the HESM cart. Looking

back at Figure 43 and moving to the right of the HESM, there is a Sorensen DCS40-75E

power supply capable of providing up to 40 V and 75 A of DC power. This is used to

mimic a generation source in the tests. Below the power supply is a Chroma 63803 AC

programmable load that receives power that is inverted through the Schneider Electric

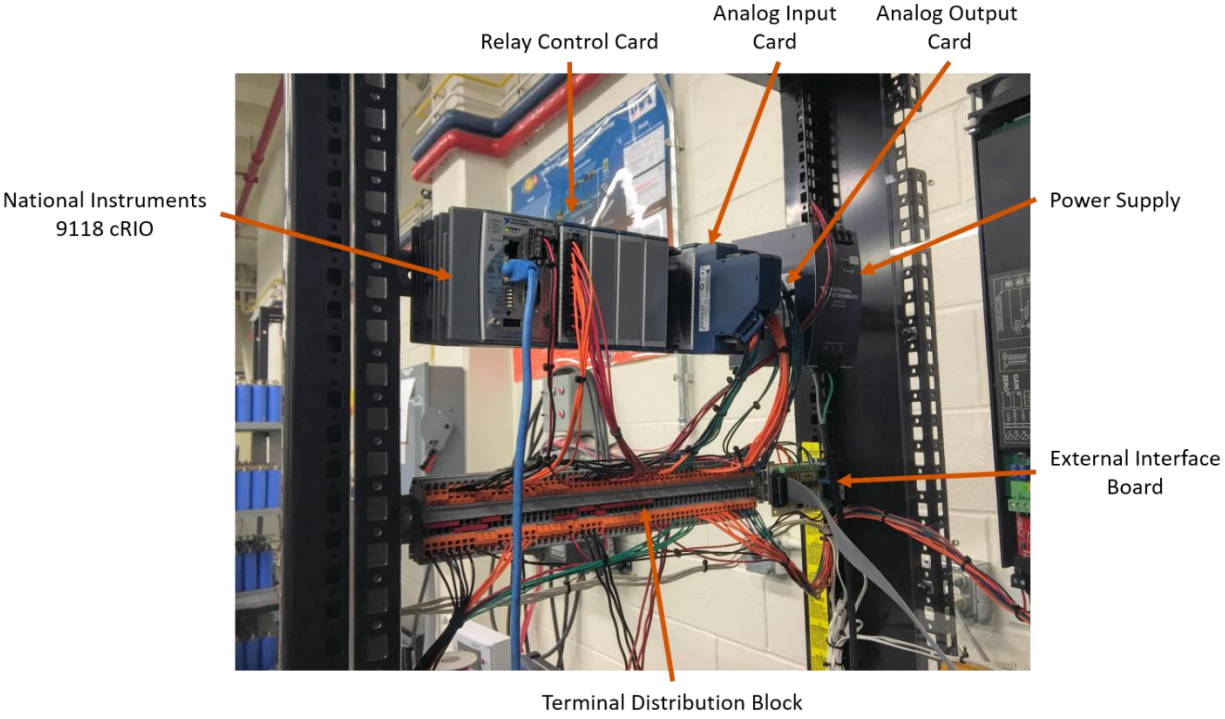Conext XW 4024 Inverter that is barely visible behind the HESM cart.

Figure 45: Close-up of the NI Controller

Another change in the experimental setup was the fuzzy logic controller. In this system,

it was necessary to use a 24 V DC load bus and a ~40 V battery bus with a much higher

current capacity so the controller was redesigned and can be seen in further detail in

Figure 46, Figure 47, and Figure 48. More detail about the specifics of each

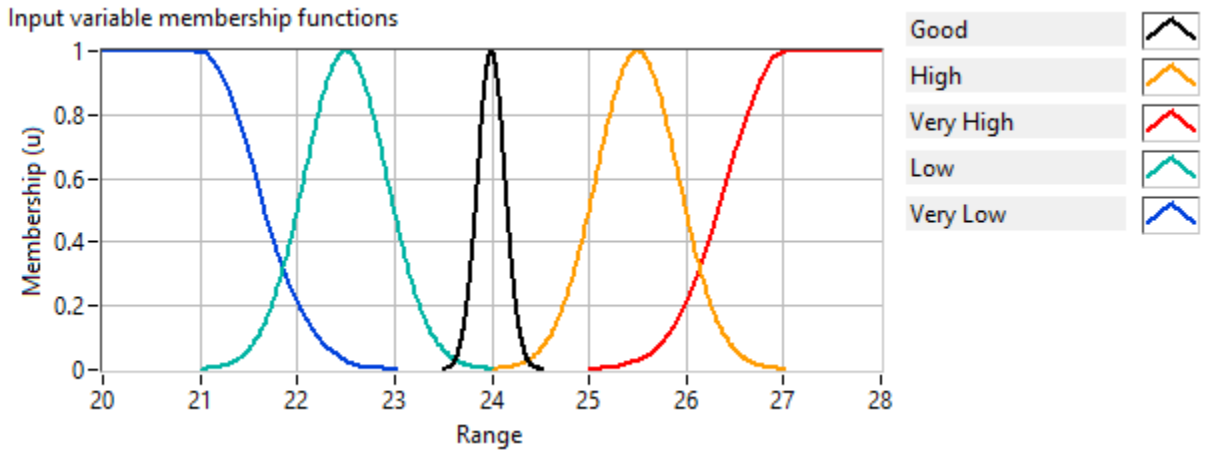membership function can be seen in Table 8.

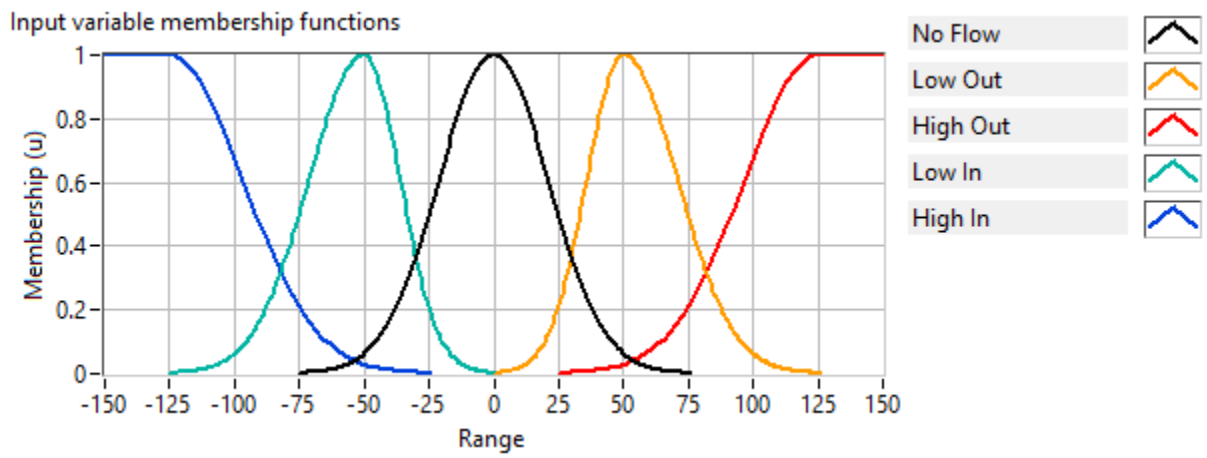Figure 46: Bus voltage input membership function

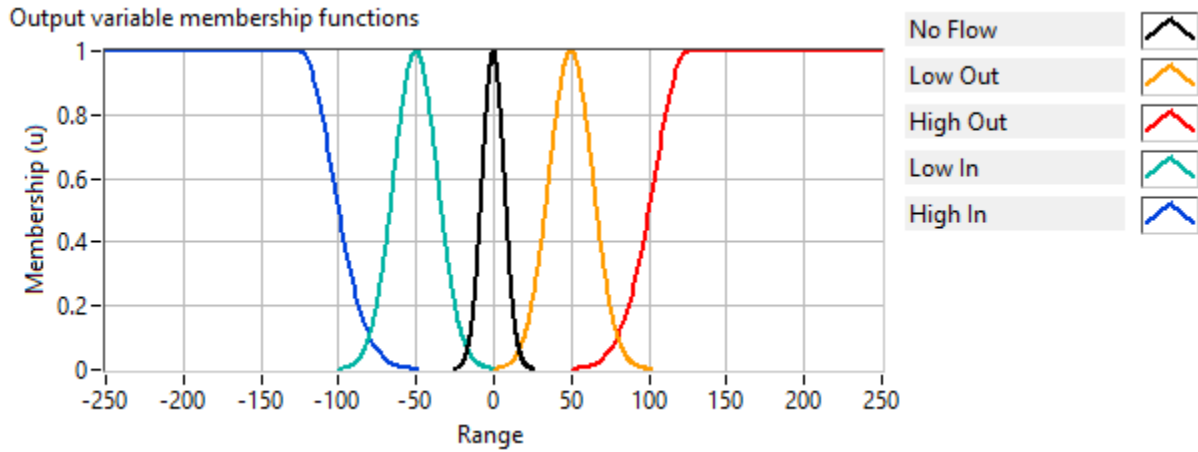Figure 47: HESM Current input membership function

Figure 48: Battery Current output membership function

Table 8: Numerical descriptions of membership functions

Input/Output	Linguistic Value	Range
Input 1	"Very Low"	< ~23 V
Input 1	"Low"	21 V – 24 V
Input 1	"Good"	23.5 V – 24.5 V
Input 1	"High"	~24 V – ~27 V
Input 1	"Very High"	> 25 V
Input 2	"High In"	< -25 A
Input 2	"Low In"	-125 A – 0 A
Input 2	"No Flow"	-75 A – 75 A
Input 2	"Low Out"	0 A – 125 A
Input 2	"High Out"	> 25 A
Output	"High Recharge"	< -50 A
Output	"Low Recharge"	~-100 A – 0 A
Output	"No Flow"	-25 A – 25 A
Output	"Low Discharge"	0 A – 100 A
Output	"High Discharge"	> 50 A

To test this system, a similar profile was designed to replicate the results of the tabletop experiments. In this case, the easiest way to use the programmable loads was to command them to operate in a constant resistance setting for a specified amount of time. The load profile run can be seen in Table 9.

Table 9: Load profile for the COTS HESM fuzzy logic control experiment

Period	Time	Value
First half of test		
High Power	5 seconds	5 Ω
Low Power	1 second	1000 Ω
Second half of test		
High Power	5 seconds	25 Ω
Low Power	1 second	1000 Ω

The results of the experiment can be seen in Figure 49 and Figure 50. These results show that the fuzzy logic controller is excellent at maintaining the bus voltage as shown in the tabletop tests. The current plots follow very similar results to the tabletop experiments and this can be considered an overall successful implementation of the controller.
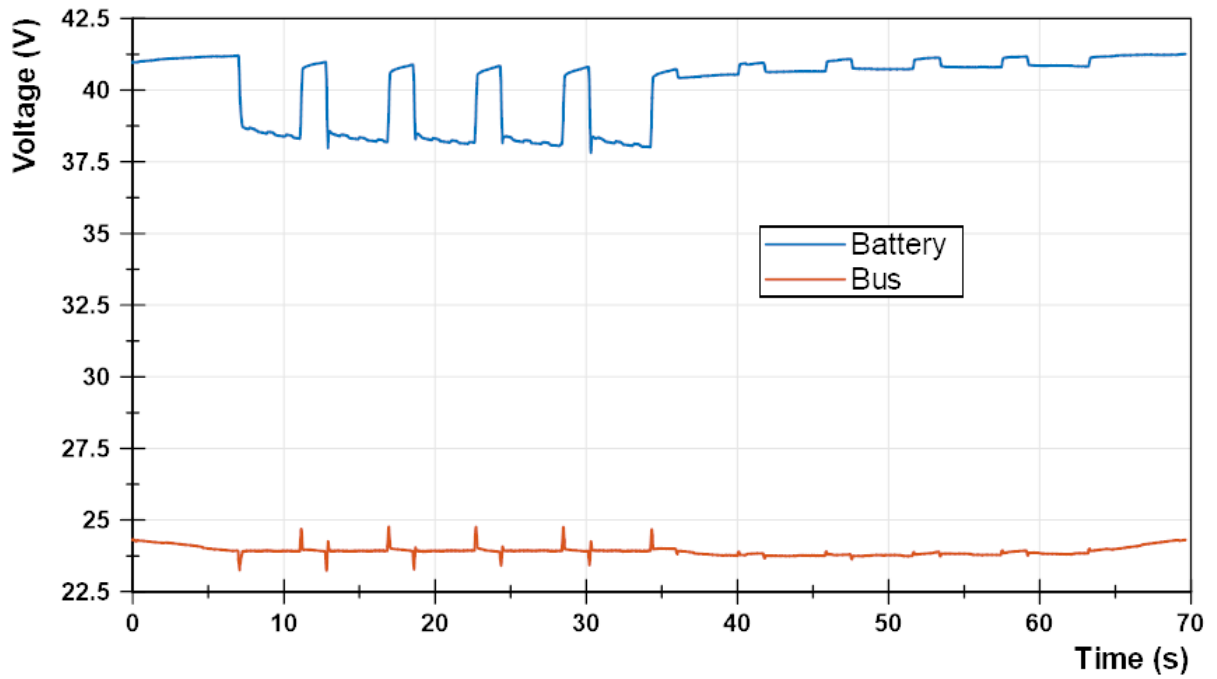
Figure 49: Voltage plot from COTS HESM fuzzy logic control test
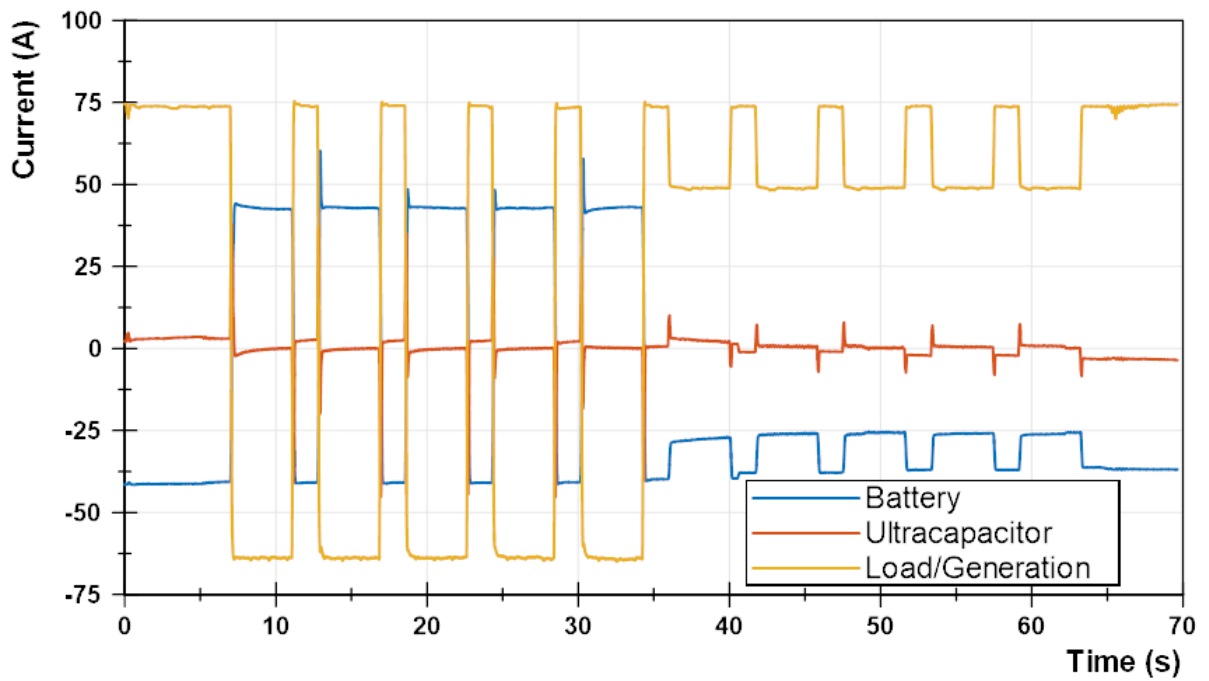

Figure 50: Current plot from COTS HESM fuzzy logic control test

Chapter 6: Summary and Conclusions

ESDs are becoming more and more crucial as integrated power systems evolve. Their application in naval settings are becoming more desirable and the challenges associated with individual ESDs can be overcome by utilizing a HESM topology. The work presented here aimed to not only demonstrate the design of a Hybrid Energy Storage Module, but to present a method of control for such a system, even while using commercial-off-the-shelf components as might be seen in a real world application. This work has shown that fuzzy logic control was capable of controlling this system through each level of construction from a model, to a custom tabletop testbed, and finally to a COTS system integration. While all of this has been demonstrated in a laboratory setup, much of the design can be largely transferred to practical application designs in future systems with very minor additional considerations. It is not expected that COTS components will ever flawlessly achieve all of the unique demands of this type of system, but the work shown here has identified some of the shortcomings of COTS technologies while simultaneously showing many of the exciting benefits that a HESM offers to future naval power application. This work will be used to ensure that a future custom solution is able to meet all of any unique demands required of a shipboard naval HESM.

Appendix A

Instruction Manuals for Custom Software and Testbeds

Operation Manual for Controlling Xantrex XHR 33-33 for HESM Tabletop

Tests

1. Ensure that the GPIB to USB cable is connected to both the power supply and

   the controlling computer

2. Ensure that the power supply is powered on

3. Open LabVIEW project file from Tabletop HESM > LabVIEW >

   PowerSupplyControl-TabletopHESM.lvproj

4. Open PowerSupplyControl-TabletopHESM.vi

You will be presented with a VI that looks like Figure 51.
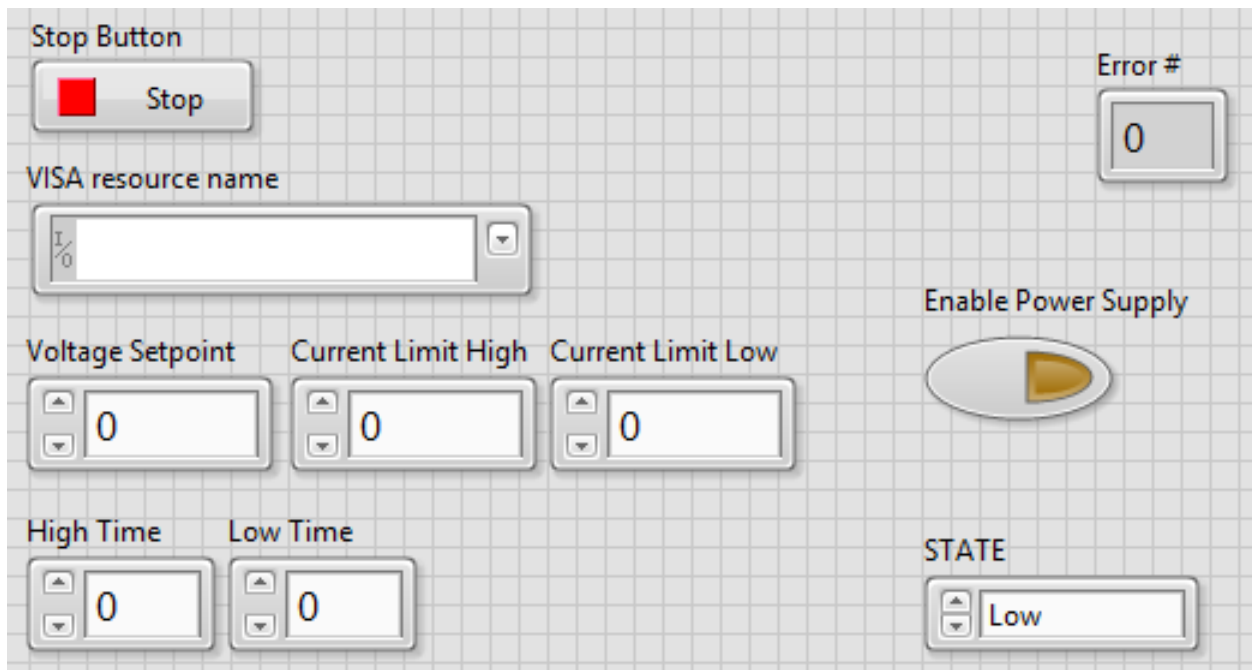

Figure 51: VI of Xantrex XHR 33-33 GPIB Control

5. Click the dropdown button and select the Xantrex XHR 33-33 GPIB resource.

This resource name may not be obvious. If you are confused and there are several devices available to choose from, try to use NI MAX to get a better idea of which resource is the power supply.

6. Type in a value for the voltage setpoint

7. Type in a value for the current limit high

8. Type in a value for the current limit low

9. Type in a value for the high time

10. Type in a value for the low time

11. Press play on the VI controls

12. When ready, press the enable power supply button

13. When test is complete, press the stop button

The descriptions of the buttons and indicators, starting from the top left and moving to the bottom right, are as follows:

- Stop button – Stops the VI when it is being run. This will also shut down the visa connection.

- Error # - This indicator shows the user what error code number is being returned by the power supply (if one is present). Error codes can be referenced in the XHR 33-33 user manual.

- VISA Resource Name – Selects the GPIB connections to the power supply.

- Voltage Setpoint – this allows the user to select what level of voltage they would like the power supply to attempt to achieve (keep in mind

that this voltage will be automatically rolled back by the power supply if the current limits set in the next fields are exceeded).

- Current Limit High – This allows the user to select how much current the power supply should be limited to during "high" times.

- Current Limit Low – This allows the user to select how much current the power supply should be limited to during "low" times.

- Enable Power Supply – This button allows the user to enable the output of the power supply. If this button is not pressed, the power supply will remain in standby mode.

- High Time – This allows the user to select how much time, in seconds, they would like the power supply to remain in "high" time (the total time of a repeated period is the summation of "high" time and "low" time).

- Low Time - This allows the user to select how much time, in seconds, they would like the power supply to remain in "low" time (the total time of a repeated period is the summation of "high" time and "low" time).

- STATE – This indicates to the user the current state of the program and flips between "High" and "Low" depending on the state.

Operation Manual for HESM Tabletop Software

1. Ensure that the PC104 is powered on and the Ethernet cable is connected to the controlling computer

2. Open the Simulink file in Tabletop HESM > MATLAB > xPC > xPC_HESMwithFuzzy_LPF.slx

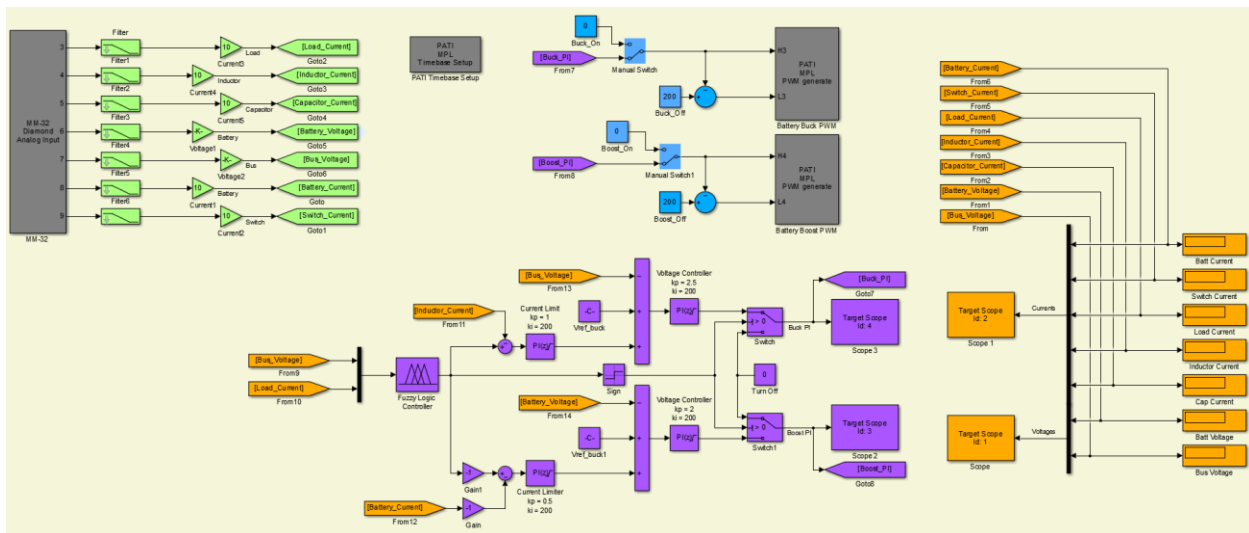You will be presented with a "model" that looks like Figure 52.



Figure 52: Simulink software for running the HESM tabletop

3. Press the "Build Model" button ⊞ . This will compile the Simulink code into C code and deploy it onto the PC104.

4. Press the "Connect to Target" button ⊙ .

5. Press the "Play" button ▶ .

6. Use the power supply as described in the Operation Manual for Controlling Xantrex XHR 33-33 for HESM Tabletop Tests section in Appendix A.

The PC104 being used in this tabletop testbed is seen in Figure 53. The top module is the PC104 PC running Simulink RTOS. It contains an Intel Atom N455 1.66 Ghz Single Core Processor and has 1 GB DDR3 800 MHz onboard memory. The second module moving down is the MPL PATI-1 PWM board. This board has 32 PWM channels that can operate independently of each other. The third module down is the Diamond DMM-32X-AT Analog Input board. This board has channels for Analog I/O and Digital I/O, but in this setup, only the Analog Inputs are being used. On the Analog Inputs, channel 1 and 2 are broken so everything is shifted over starting at channel 3.
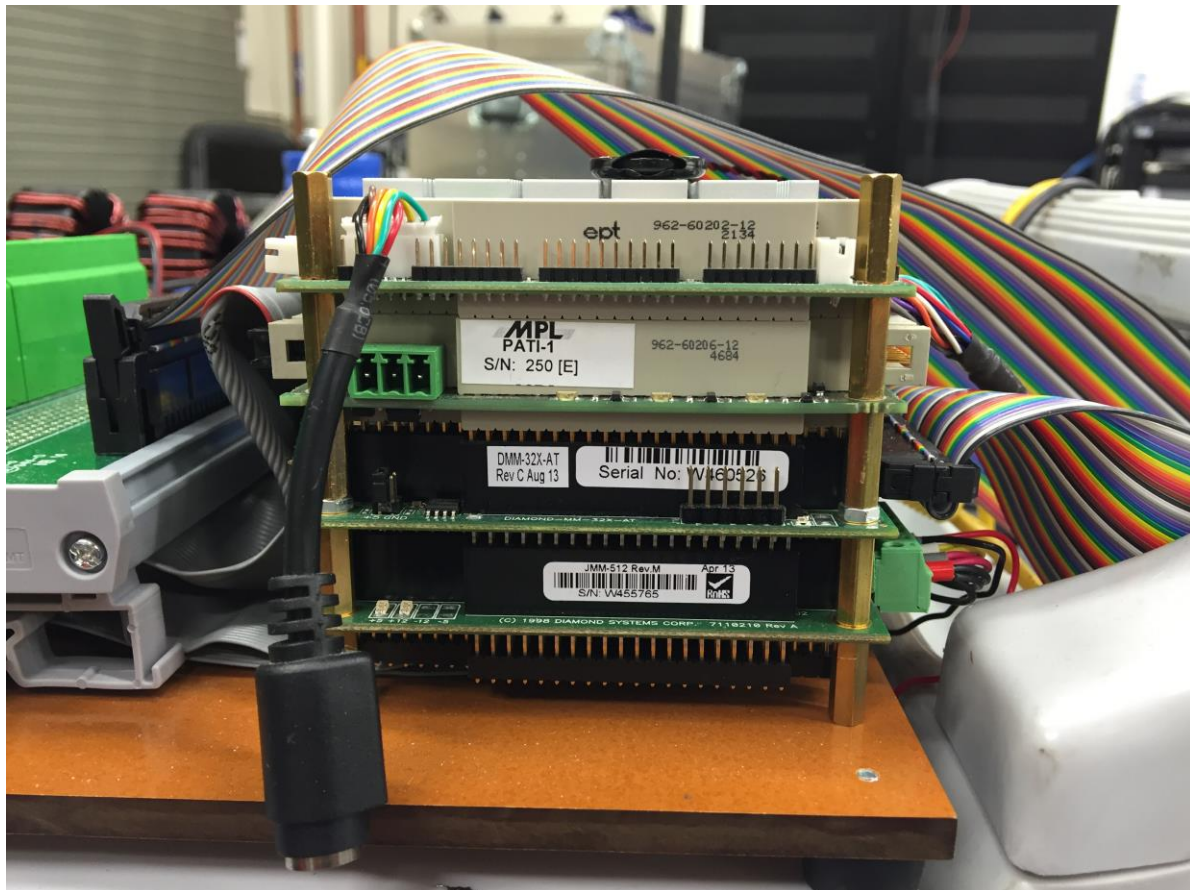

Figure 53: PC104 target PC for HESM tabletop experiments

The color scheme of the software is as follows:

- Grey blocks – These are blocks directly associated with the PC104 target PC. These are either settings blocks or direct I/O interfacing blocks.

- Green blocks – These blocks are associated with signal input and conditioning. These blocks are responsible for filtering the signals, applying their gains, and setting the variables to be used by other blocks.

- Orange blocks – These blocks are associated with reading variables. They are used as control inputs and for indicators on the GUI for the user to validate what they think they should be seeing. The indicators do not update very quickly, so the important values are actually sent to the PC104 for a virtual scope that is displayed on a VGA connected monitor.

- Purple blocks – These blocks are associated with controls. These controls are not interactive with the user and are essential in voltage control, current limiting, and fuzzy logic control of the tabletop.

- Blue blocks – These blocks are associated with user interactive controls. The constant blocks are used to set how many clock cycles on a 10 MHz clock will be used for 'on' and 'off' times of the switch. The percentage of 'on' time over 'off' time is the duty cycle of the switching converter. These are only used if the Manual switch is in the

up position. If the manual switch is in the lower position, it will defer to the purple control blocks.

The descriptions of the most important buttons and indicators, starting from the top left and moving to the bottom right, are as follows:

- MM-32 Diamond Analog Input – Direct access to the analog I/O pins on the PC104. These analog values can range from -10 to 10 V and they start at a base address of 0x300. This is configured as differential inputs for pins 1-16 and the first channel used in this software is channel 3.

- Filters – These blocks are used as low-pass filters for all the signals coming from the HESM tabletop. The time constant for the filter is set at 10 ms.

- PATI MPL Timebase Setup – This sets the frequency for the PWM generator on the PATI board. For this software, only the TCR1 timer is used, so the PATI board clock is set to 10 MHz so each period is 100 ns.

- PATI MPL PWM Generate – This block is responsible for generating the PWM signal for the switches. The H input on the blocks correspond to the periods of the 10 MHz clock that the PWM signal will remain high and the L input corresponds to the periods of the 10 MHz clock that the PWM signal will remain low. High always comes before low. They should add up to the desired period of the switching frequency.

- Control blocks – These blocks are set up with two separate loops of control. One loop is for buck converter control (top) and one is for boost converter control (low). Only one loop can be active at a time, which is dictated by the sign of the fuzzy logic controller output and controlled with the software switches. Both of these controllers output to a variable that is accessed by the PWM generator blocks, but also to a target scope, which is responsible for outputting the waveform to a VGA connected monitor on the PC104.

- Measurement blocks – These blocks not only give a front panel read out of the voltages and currents that update slowly, but also output all voltages and currents to target scopes which, like above, output the waveform to a VGA connected monitor on the PC104.

Operation Manual for COTS HESM Software

1. Turn on the PXI chassis

2. Turn on the control and data acquisition PC

3. Go to "E:\Dropbox\UTA PPEL Team Folder\Projects\COTS
   HESM\LabVIEW\Newest HESM"

4. Open "HESM.lvproj"

5. Open "PXI-QuickStart.vi", click run, and minimize the VI (seen in Figure 54)

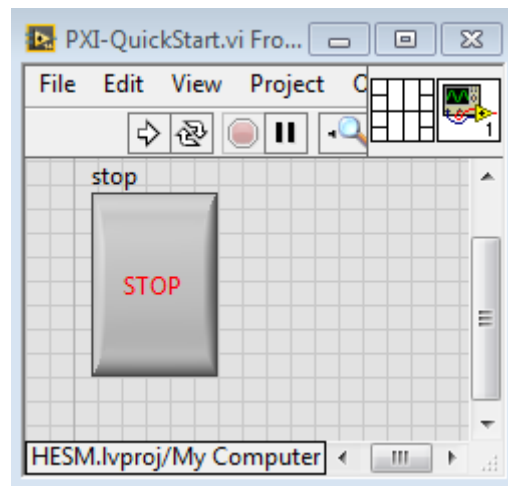Figure 54: PXI-QuickStart.vi Front Panel

6. Open "RunLoadProfile.vi", select the file for the programmable load, and click run
   (seen in Figure 55)

   To edit the file:

   a. Go to the file location ("E:\Dropbox\UTA PPEL Team
      Folder\Projects\COTS HESM\LabVIEW\Chroma AC Control")

   b. Open the file using excel for ease, but the file can be edited in notepad

   c. Follow convention to make edits

To change the file during operation

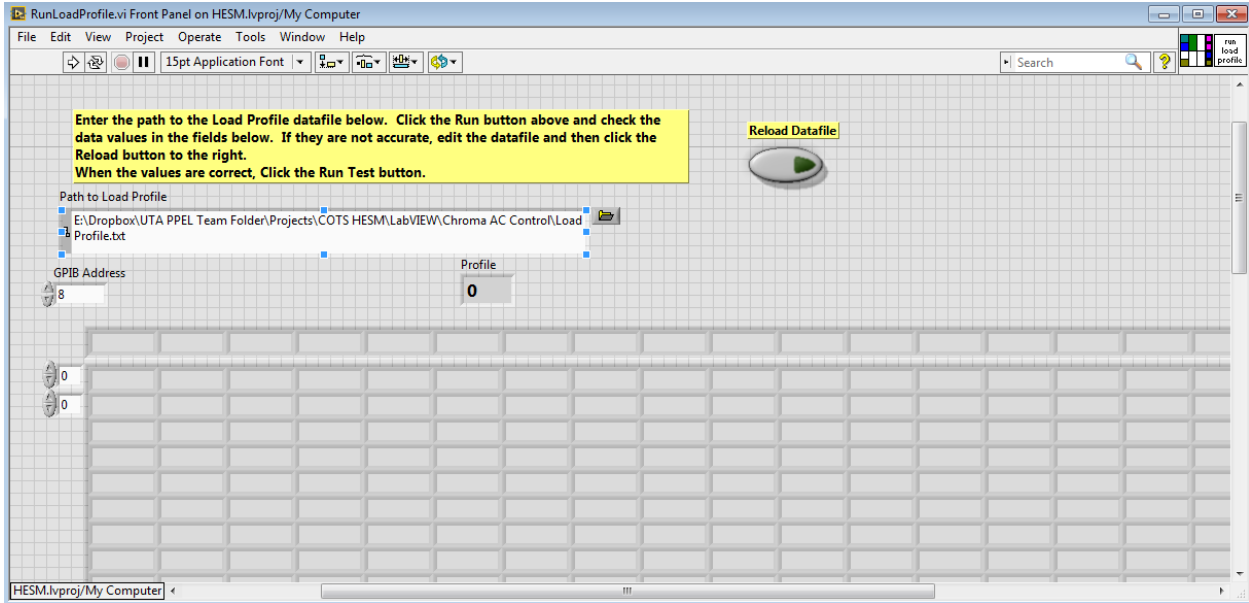   a. Select file from file browser

    b. Click reload data file

Figure 55: RunLoadProfile.vi Front Panel

7. Press the "plus" button to the left of the cRIO target "newHESM"

8. Open "Main.vi" and click run (seen in Figure 56)
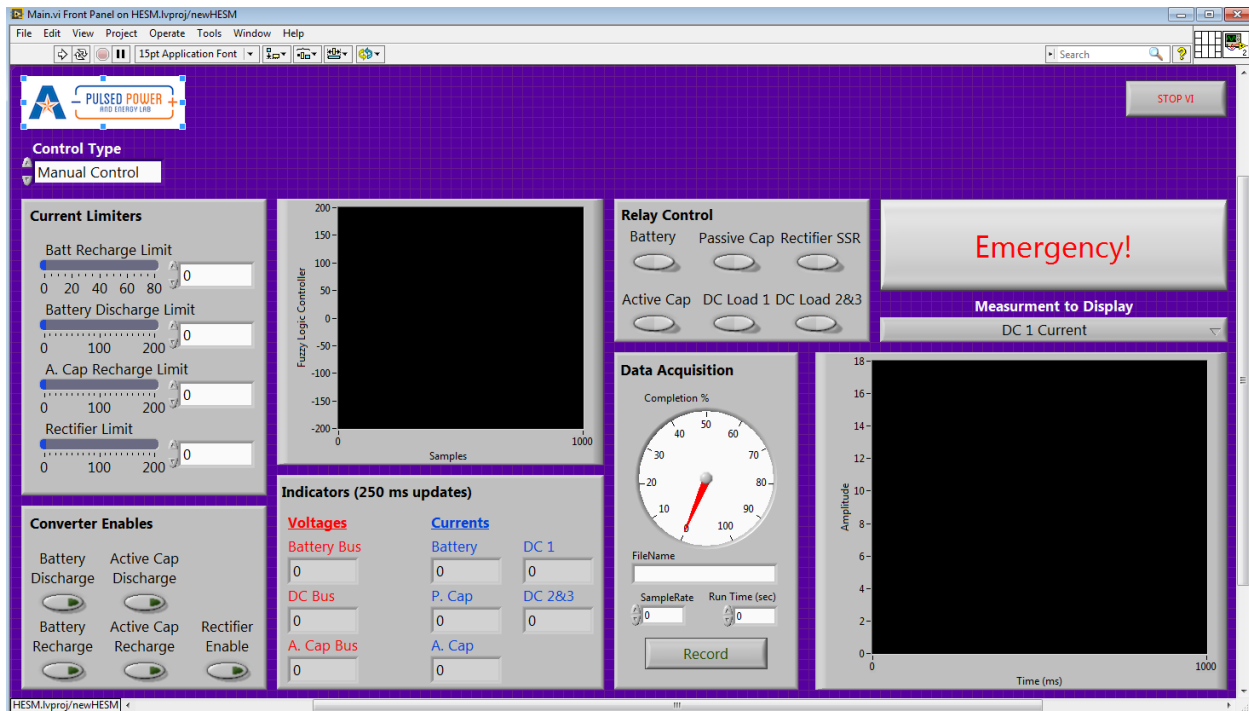
Figure 56: Main.vi Front Panel

9. Use the relay control box to insert the power sources desired

10. Set the current limiters if manual operation is desired

11. Enable the desired converters if manual operation is desired

12. Fill in the file name box, the sample rate, and the run time of the test in the Data

    Acquisition box if data recording is desired

13. Select the control type if Fuzzy Logic Control is desired

    a. Note: This mode does not utilize the active capacitor

14. Press record to initiate the test

    a. Note: This button turns on and off the recording of the PXI chassis and it

    initiates the programmable load profile all by network variables – it

    requires no human intervention.

15. If anything causes great concern, the emergency stop button can be used to open all relays and disable all converters without stopping the program, use this only in emergencies as it can degrade the lifetime of the relays

16. When finished using, the stop vi button in the top right will also ensure that all converters are disabled and that all relays are open before shutting down the VI

References

[1] D. Stoudt, "Naval Directed-Energy Weapons - No Longer a Future Weapon Concept," *Leading Edge,* vol. 7, no. 4, pp. 6-11, 2012.

[2] H. Fair, "Progress in Electromagnetic Launch Science and Technology," *IEEE Transactions on Magnetics,* vol. 43, no. 1, pp. 93-98, 2007.

[3] H. Fair, "Advances in Electromagnetic Launch Science and Technology and its Applications," *IEEE Transactions on Magnetics,* vol. 45, no. 1, pp. 225-230, 2009.

[4] J. Kuseian, "Naval Power Systems Technology Development Roadmap PMS 320," May 2013. [Online]. Available: http://www.navsea.navy.mil/Media/Forms/AllItems.aspx. [Accessed 2014].

[5] N. Doerry, "Next Generation Integrated Power System NGIPS Technology Development Roadmap," November 2007. [Online]. Available: http://www.dtic.mil/cgi-bin/GetTRDoc?AD=ADA519753. [Accessed 2014].

[6] W. Matthews, "Navy: Energy Weapons Ready for Ships," May 2013. [Online]. Available: http://seapowermagaizine.org/sas/stories/20130410-energy-weapons.html. [Accessed 2014].

[7] J. Thongam, "All-electric ships - A review of the present state of the art," in *8th International Conference and Exhibition on Ecological Vehicles and Renewable Energies*, 2013.

[8] Y. Chuan, G. Venayagamoorthy and K. Corzine, "AIS-Based Coordinated and Adaptive Control of Generator Excitation Systems for an Electric Ship," *IEEE Transactions on Industrial Electronics,* vol. 59, no. 8, pp. 3102-3112, 2012.

[9] J. Gully, "Investigation of an Alternator Charged Pulse Forming Network with Flywheel Energy Storage," *IEEE Transactions on Magnetics,* vol. 29, no. 1, pp. 969-974, 1993.

[10] D. Swett and J. Blanche, "Flywheel charging module for energy storage used in high-voltage pulsed and multi-mode mobility hybrid electric military vehicle power system," in *Conference Record of the 2004 Power Modulator Symposium and 2004 High Voltage Workshop*, 2004.

[11] J. Ennis, "Recent Advances in High Voltage, High Energy Capacitor Technology," in *16th IEEE International Pulsed Power Conference*, San Diego, 2007.

[12] H. Boenig, "Design and testing of high power reptitively pulsed, solid-state closing switches," in *Industry Applications Conference, Thirty-Second IAS Annual Meeting, IAS '97*, 1997.

[13] S. Balathandayuthapani, C. Edrington and S. Henry, "Study on converter topologies for capacitive pulse forming network and energy storage units in electric ship," in *2011 IEEE Electric Ship Technologies Symposium (ESTS)*, 2011.

[14] R. Kotz and M. Carlen, "Principles and Applications of Electrochemical Capacitors," *Electrochimica Acta,* vol. 45, pp. 459-462, 2000.

[15] P. Novak, D. Wetz and B. Shrestha, "Cycling Fatigue induced on Electrochemical Energy Storage Cells as a result of High C Pulsed Charging," *Electrochemical Society Transactions,* vol. 50, no. 26, pp. 175-186, 2013.

[16] D. Wetz, B. Shrestha and P. Novak, "Pulsed Evaluation of High Power Electrochemical Energy Storage Devices," *IEEE Transactions on Dielectrics and Electrical Insulation,* vol. 20, no. 4, pp. 1040-1048, 2013.

[17] Saft America, Inc., "Rechargeable lithium-ion battery VL 5U - Ultra high power cell; Doc. No. 54073-2-1009," 2009.

[18] B. Shrestha, D. Wetz and P. Novak, "The Impact of High Pulsed Loading on the Fatigue of Electrochemical Energy Storage Devices," *Electrochemical Society Transactions,* vol. 50, no. 26, pp. 187-196, 2013.

[19] D. A. Wetz, B. Shrestha, S. T. Donahue, D. N. Wong, M. J. Martin and J. M. Heinzel, "Capacity Fade of 26650 Lithium-Ion Phosphate Batteries Considered for Use Within a Pulsed-Power System's Prime Power Supply," *Plasma Science, IEEE Transactions on,* vol. 43, pp. 1448-1455, 2015.

[20] M. Hantel, Graphite Oxie and Graphene Oxide Based Electrode Materials for Electrochemical Double Layer Capacitors, Munich: Technische Universität München, 2013.

[21] D. Shin, "Battery-Supercapacitor Hybrid System for High-Rate Pulsed Load Applications," in *Design, Automation & Test in Europe Conference & Exhibition, 2011*, 2011.

[22] L. Baoquan, Z. Fang and B. Xianwen, "Control Method of the Transient Compensation Process of a Hybrid Energy Storage System Based on Battery and Ultracapacitor in Micro-grid," in *IEEE International Symposium on Industrial Electronics*, 2012.

[23] A. Khaligh and Z. Li, "Battery, Ultracapacitor, Fuel Cell, and Hybrid Energy Storage Systems for Electric, Hybrid Electric, Fuel Cell, and Plug-In Hybrid Electric Vehicles: State of the Art," *IEEE Transactions on Vehicular Technology,* vol. 59, no. 6, pp. 2806-2814, 2010.

[24] L. Gao, R. A. Dougal and S. Liu, "Power Enhancement of an Actively Controlled Battery/Ultracapacitor Hybrid," *Power Electronics, IEEE Transactions on,* vol. 20, no. 1, pp. 236-243, 2005.

[25] I. J. Cohen, J. P. Kelley, D. A. Wetz and J. Heinzel, "Evaluation of a Hybrid Energy Storage Module for Pulsed Power Applications," *Plasma Science, IEEE Transactions on,* vol. 42, no. 10, pp. 2948-2955, 2014.

[26] S. M. Lukic, S. G. Wirasingha, F. Rodriguez and J. Cao, "Power Management of an Ultracapacitor/Battery Hybrid Energy Storage System in an HEV," in *IEEE Vehicle Power and Propulsion Conference, 2006. VPPC '06*, Windsor, 2006.

[27] D. Carreira, G. D. Marques and D. M. Sousa, "Hybrid Energy Storage System with a Low Cost Digital Control," in *2015 9th International Conference on Compatibility and Power Electronics (CPE)*, Costa da Caparica, 2015.

[28] C. Jin, N. Lu, S. Lu, Y. Makarov and R. Dougal, "Coordinated Control Algorithm for Hybrid Energy Storage Systems," in *2011 IEEE Power and Energy Society General Meeting*, 2011.

[29] V. B. Semwal, P. Chakraborty and G. C. Nandi, "Less computationally intensive fuzzy logic (type-1)-based controller for humanoid push recovery," *Robotics and Autonomous Systems,* vol. 63, no. 1, pp. 122-135, 2015.

[30] Y. Lu, H. L. Hess and D. B. Edwards, "Adaptive Control of an Ultracapacitor Energy Storage System for Hybrid Electric Vehicles," in *IEMDC '07, IEEE International Antalya: Electric Machines and Drives Conference*, 2007.

[31] C. H. Wu, P. Y. Chen and J. C. Ke, "On the Study of Energy-Based Control Strategy for a Lithium Battery/Supercapacitor Hybrid Energy Storage System," in *2010 International Conference on Environmental Science and Information Application Technology (ESIAT)*, Wuhan, 2010.

[32] Z. Yu, Z. Jiang and X. Yu, "Control Strategies for Battery/Supercapacitor Hybrid Energy Storage Systems," in *IEEE Energy 2030 Conference*, Atlanta, 2008.

[33] D. G. Wilson, R. D. Robinett III and S. Y. Goldsmith, "Renewable Energy Microgrid Control with Energy Storage Integration," in *2012 International Symposium on Power Electronics, Electrical Drivers, Automation and Motion (SPEEDAM)*, Sorrento, 2012.

[34] I. J. Cohen, D. A. Wetz, C. Storm and J. Heinzel, "Impact of a Hybrid Energy Storage Module on Power Quality of a Fossil Fuel Generator," in *Proceedings of the 2014 American Society of Naval Engineers Electric Machines Technology Symposium (EMTS)*, Philadelphia, 2014.

[35] Y. Zhang, J. Zhenhua and Y. Xunwei, "Small-Signal Modeling and Analysis of Battery-Supercapacitor Hybrid Energy Storage Systems," in *IEEE Power & Energy Society General Meeting PES '09*, Calgary, 2009.

[36] V. H. Johnson, A. A. Pesaran and T. Sack, "Temperature-Dependent Battery Models for High-Power Lithium-Ion Batteries," in *17th Annual Electric Vehicle Symposium*, Montreal, 2000.

[37] T. J. Ross, Fuzzy Logic with Engineering Applications, McGraw-Hill, 1995.

[38] M. Sugeno, "An Introductory Survey of Fuzzy Control," *Information Sciences,* vol. 36, no. 1, pp. 59-83, 1985.

[39] C. C. Lee, "Fuzzy Logic in Control Systems: Fuzzy Logic Controller. II.," *IEEE Transactions on Systems, Man and Cybernetics,* vol. 20, no. 2, pp. 419-435, 1990.

[40] NXP, "Designing RC snubbers - AN 11160," 2012.

[41] Zahn Electronics, Inc., "DC/DC Converters," 2015. [Online]. Available: http://www.zahninc.com/dcdcsdsu1.html. [Accessed 22 September 2015].

[42] Maxwell Technologies, "48V Modules Datasheet," 2013. [Online]. Available: http://www.maxwell.com/images/documents/hq_48v_ds10162013.pdf. [Accessed 22 September 2015].

[43] "Conext XW Inverters/Chargers," Schneider Electric, [Online]. Available: http://www.schneider-electric.com/.

[44] K2 Energy, "High Capacity LFP26650P Power Cell Data," [Online]. Available: http://liionbms.com/pdf/k2/LFP26650P.pdf. [Accessed 22 September 2015].

[45] *MIL-STD-1399,* Department of Defense, 2008.

[46] L. Gao, R. Dougal and S. Liu, "Active Power Sharing in Hybrid Battery/Capacitor Power Sources," in *Eighteenth Annual IEEE Applied Power Electronics Conference and Exposition, 2003 (APEC '03)*, 2003.

Biographical Information

Isaac J. Cohen was born in Miami, Florida in 1988. He received the B.S. degree in electrical engineering in 2013 from the University of Texas at Arlington and has spent several summers serving as a research fellow at the Naval Surface Warfare Center in Philadelphia, Pennsylvania. He served as Chair of the Student Branch of IEEE at UTA in 2012, where he received several awards for his outstanding service. He currently serves as Chair of the Young Professionals affinity group within the IEEE Fort Worth Section. His research interests include applying control theory to power electronics in microgrid, energy storage, and pulsed power settings.